Structural studies of multispecific antibody-antigen complexes by cryo-electron microscopy

David Fernandez-Martinez

To cite this version:

David Fernandez-Martinez. Structural studies of multispecific antibody-antigen complexes by cryo-electron microscopy. Structural Biology [q-bio.BM]. Université Grenoble Alpes [2020-..], 2021. English. NNT : 2021GRALV017 . tel-03626955

HAL Id: tel-03626955
https://theses.hal.science/tel-03626955v1

Submitted on 1 Apr 2022

THÈSE

Pour obtenir le grade de

DOCTEUR DE L'UNIVERSITE GRENOBLE ALPES

Spécialité : **Biologie Structurale et Nanobiologie**

Arrêté ministériel : 25 mai 2016

Présentée par

David FERNANDEZ-MARTINEZ

Thèse CIFRE dirigée par **Gordon LEONARD**
codirigée par **Magali MATHIEU** et co-encadrée **par Eaazhisai KANDIAH**

préparée au sein du **Structural Biology Group, European Synchrotron Radiation Facility** et **Integrated Drug Discovery Group, SANOFI**
dans **l'École Doctorale Chimie et Sciences du Vivant**

Etudes structurales de complexes anticorps-antigène multispécifiques par cryo-microscopie électronique

–

Structural studies of multispecific antibody-antigen complexes by cryo-electron microscopy

Thèse soutenue publiquement le **31 Mars 2021,**
devant le jury composé de:

Examinateur : Prof. Jose María VALPUESTA
Examinateur : Prof. Jan STEYAERT
Examinateur : Dr. Sergio MARCO
Rapporteuse : Dr. Nushin AGHAJARI
Rapporteuse : Dr. Julie BOUCKAERT
Présidente : Dr. Nicole THIELENS
Directeur de Thèse : Dr. Gordon LEONARD

Acknowledgements

First of all, I would like to thank my thesis supervisors. One of the main reasons that made me decide to undertake this PhD was the connection I felt with them during the interviews. To Dr. Eaazhisai Kandiah, a very big thank you for supporting me during my highs and lows, and for your daily monitoring and help. Overcoming such a challenging project would not have been possible without your continuous guidance, both as a mentor and as a friend. To Dr. Magali Mathieu, for your mentoring, for showing me the ins and outs of the pharmaceutical industry, and for making sure all means were available to carry every experiment that we desired throughout the PhD. Finally, to Dr. Gordon Leonard, for his invaluable experience and suggestions, and his hard work in correcting my thesis and CST.

I want to thank my thesis jury for all their questions and insightful discussion: the jury president Dr. Nicole Thielens, the referees Dr. Julie Bouckaert and Dr. Nushin Aghajari and the examiners Prof. José María Valpuesta, Prof. Jan Steyaert and Dr. Sergio Marco.

Similarly, I want to extend my thanks to the members of my thesis advisory committee (TAC), Dr. Laurent Terradot and Prof. Guy Schoehn for all their advice that helped shape the project throughout the years.

Thank you to all the colleagues at Sanofi Vitry and Sanofi Pasteur, who have helped me greatly in making sure experiments were successful or have provided very insightful discussions. Special mention to Prof. Alexey Rak, Valerie Steier, Françoise Begassat, and Marie Claire Nicolai for their training and help. I am also very grateful to the Biologics teams at Sanofi Vitry and Sanofi Frankfurt for providing me with apo-antibodies and therefore allowing me to focus on the next steps of the project.

Thank you to the Structural Biology group at ESRF, especially to Olof Svensson for his great help with setting up the infrastructure required to kickstart cryo-EM at the ESRF. Similarly, thank you to Christoph Mueller-Dieckmann for making the first PhD program in cryo-EM a reality and thus helping establish a strong foundation for future students.

I would like to thank all the members at the CIBB, especially Samira Acajjaoui, Melissa Saidi and Lyna Khettabi, for all their help in the lab and for putting up with my requests; and

Hadrien Depernet, who has been a very close friend and has accompanied me on this PhD journey during all these years. Grazie di cuore Dr. Alessandro Grinzato, for also being like a brother to me during your stay here and your incredible help in advanced electron microscopy.

I want to also extend my thanks to the members of the EM platform at the Institut de Biologie Structurale for their constant help, patience and training in all the different microscopes.

To Dr. Montserrat Soler-Lopez, words cannot express how thankful I am for your help in and out of the lab, for all the long chats, for being a friend. I can only wish you all the best for future endeavours.

Finally, thank you to my family and friends. Eskerrik asko Unai, Patri, Erik, Lae, Pablo… lagun guztioi proiektutik distraitzeagatik eta Aita, Ama, Lydia, Aitona ta Amona… familia guztiari nire ondoan beti egoteagatik.

Enfin je tiens a remercier Anaïs, qui est la meilleur compagne que je pourrais souhaiter et qui m'a soutenu dans mes meilleurs et pires jours. J'espère que je pourrai être là aussi pour ta thèse.

List of abbreviations

ADCC	Antibody dependent cell cytotoxicity
CCD	Charge-coupled device
CD	Cluster of differentiation
CODV	Cross-over dual-variable
CDR	Complementarity determining region
Cryo-EM	Cryo-electron Microscopy
CTF	Contrast transfer function
(k)Da	(kilo) Daltons
DDM	n-dodecyl β-D-maltopyranoside
DE	Direct electron
DSF	Differential scanning fluorimetry
DTT	Dithiothreitol
ESRF	European Synchrotron Radiation Facility
EMBL	European Molecular Biology Laboratory
Fab	Fragment, antigen binding
Fc	Fragment, constant
FEG	Field emission gun
FFT	Fast Fourier transform
Fv	Fragment variable
GS-FSC	Gold-standard Fourier shell correlation
HEPES	4-(2-hydroxyethyl)-1-piperazine-ethanesulfonic acid

HPLC	High pressure liquid chromatography
IBS	Institut de Biologie Structurale
Ig	Immunoglobulin
IL	Interleukin
JAK	Janus kinase
K_D	Dissociation constant
Koff	Dissociation rate constant
Kon	Association rate constant
mAb	Monoclonal antibody
MW	Molecular weight
MP	Mass photometry
Ni-NTA	Nickel-Nitrilotriacetic acid
NS-EM	Negative-stain electron microscopy
PBS	Phosphate buffer saline
PCA	Principal component analysis
PDB	Protein Data Bank
PSF	Point spread function
QC	Quadruple complex
SAXS	Small-angle X-Ray scattering
SDS-PAGE	Sodium dodecyl sulphate polyacrylamide gel electrophoresis
SEC	Size exclusion chromatography
SPA	Single particle Analysis
SPR	Surface plasmon resonance

SST	Sodium silicotungstate
STAT	Signal transducer and activator of transcription
TBS	Tris buffered saline
TBTI	Tetravalent Bispecific Tandem Immunoglobulin
TC	Triple complex
VH	Variable heavy chain
VL	Variable light chain

Table of Contents

List of figures

List of tables

Chapter 1

Introduction

The immune system

-

Antibodies and antibody-based therapeutics

-

Interleukins 4/13 and their role in cancer

-

Cryo-EM: Sample preparation & Single Particle Analysis

-

Preamble to the thesis manuscript

1. Introduction

1.1 The immune system

The immune system is the name given to a series of mechanisms, essential for survival, by which all organisms protect themselves from pathogens. These pathogens are agents that can cause disease and range from biologically simple structures such as viruses to very complex ones such as an organism's own cells (Owen et al., 2013).

Two main types of immune response have been described (Pancer & Cooper, 2006). The innate immune system is inherent to all living organisms and encompasses a series of non-specialized strategies to counter pathogen action. In humans there are many elements that can be classified as belonging to the innate immune system, from anatomical barriers like skin or mucus, to more complex responses like inflammation.

The adaptive or specific immune system, on the other hand, is only found in mammals (Pancer & Cooper, 2006) and is highly efficient in the process of antigen recognition, elimination and in some cases, provides lifetime protection. Antigens comprise any molecule that causes a response from the adaptive system. The adaptive system can be divided into two categories, cell-mediated immunity and humoral immunity, and is mainly driven by lymphocytes (B, T or NK). Adaptive response is not only highly specialized for each type of antigen; it can also provide immunological memory, so pathogens do not cause harm to the organism again, sometimes for the remainder of its life.

The number of mechanisms by which the adaptive system can combat antigen actions are overwhelming, but in most of them, there is a family of proteins, antibodies, that is the cornerstone of the response by both identifying an antigen and reacting to its presence.

1.2 Antibodies and antibody-based therapeutics

1.2.1 Overview and structure

Antibodies are typically Y-shaped large globular plasma glycoproteins (Maverakis et al., 2015) classified into five different classes: IgA, IgD, IgE, IgG and IgM. IgA is a dimer, IgM a pentamer or hexamer and the other classes are all monomers. The polymeric IgM is synthesized and secreted as a first line of response by plasma or naïve mature B-cells, and it is not until a process modulated by T-helper cells called "isotype switching" occurs that IgA, IgG or IgE are synthetized. This process is driven by an irreversible genetic recombination that is also responsible for the specificity towards the antigen (Market & Papavasiliou, 2003). Antibodies are composed of two heavy chains (H) and two light chains (L), can be found in two states - soluble versions in plasma or bound to receptors in membranes – and, because of their many functions, they are considered the central part, or backbone, of the adaptive immune response.

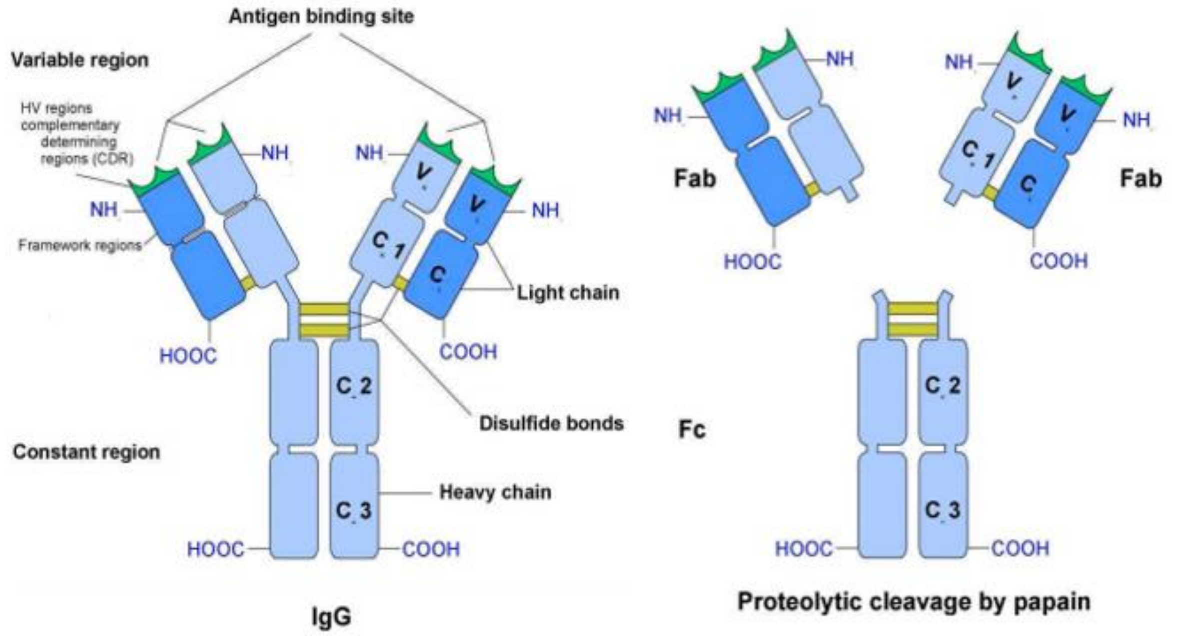

Figure 1.1: Schematic representation of an IgG antibody. An antibody is formed by two light (VL-CL, dark blue) and two heavy (VH-CH1-CH2-CH3, light blue) chains, and consists of a constant region (Fc) and two identical antigen-binding regions (Fab). The Fc and Fab regions are linked by a highly-flexible hinge. The antigen binding sites are located in the Fv domains, with the complementarity determining regions (CDR) allowing for specific binding to targets while the framework regions (FR) provide structural support. Adapted from Wittel et al., 2001.

IgG antibodies, with molecular weights of ~150 KDa, are the most abundant and also the basis of most antibody-based therapies (Kontermann & Brinkmann, 2015). IgGs contain two regions: the antigen binding fragment (Fab) and the fragment constant (Fc). The Fab region of the antibody consists of two variable (VH and VL) and two constant (CH1 and CL) domains (**Figure 1.1**). For antigen recognition the fragment variable domain (Fv, formed by VH and VL), contains the antigen binding site or paratope.

Fvs contain six hypervariable loops, three in the heavy chain and three in the light chain, known as complementarity determining regions (CDR) that, together, form the paratope and are the most important regions in the antigen binding process. CH1 and CL provide the structural integrity and flexibility needed for correct antigen recognition and binding. Although the heavy chains are constant in all B-cells (excluding VH) there can be two types of light chains (κ or λ), which are mutually exclusive in the same B-cell and are differentiated by their composition at the CL domain. Not much is yet known about why one or the other is produced, but their proportion change in serum can be indicative of the presence of malignant cells or other disease (Leong & Cooper, 2003).

1.2.3 Therapeutic use of antibodies

With the advent of the hybridoma technology in 1975, mass production of identical antibodies (monoclonal antibodies, mAbs) became widely available and, shortly after, these molecules were being already used in diagnosis and general biochemistry (Getzoff et al., 1987). However, it was not until 1988 that techniques to humanize monoclonal antibodies made it possible to explore therapeutical applications of mAbs (Verhoeyen et al., 1988). Since then ,medicine has experienced a revolution in antibody therapy, with currently over 50 mAbs approved for clinical use or late-stage clinical trials (Kaplon & Reichert, 2018).

The therapeutic uses of mAbs are many, and even though they are nowadays considered the backbone for state-of-the-art cancer treatment strategies, success has been reported in other areas of medicine. As an example, in 2017 several mAbs have been approved that target molecules linked to psoriasis, dermatitis, rheumatoid arthritis and haemophilia (Godar et al., 2018; Weiner, 2015).

Nevertheless, strategies exploiting the use of mAbs in the treatment of cancer remain perhaps the best example to use to introduce the functions and capabilities of these monospecific molecules (**Figure 1.2**). Here, three main approaches have been adopted: those directly blocking processes occurring within or due to tumoral cells; immunoconjugation for local delivery of drugs or radioactive molecules; retargeting based strategies in which the immune system is directly helped to combat the disease. However, while monospecific mAbs (i.e. antibodies targeting a single antigen) can offer many options for development of strategies against diseases, many challenges require more complex responses that cannot be achieved using these mAbs.

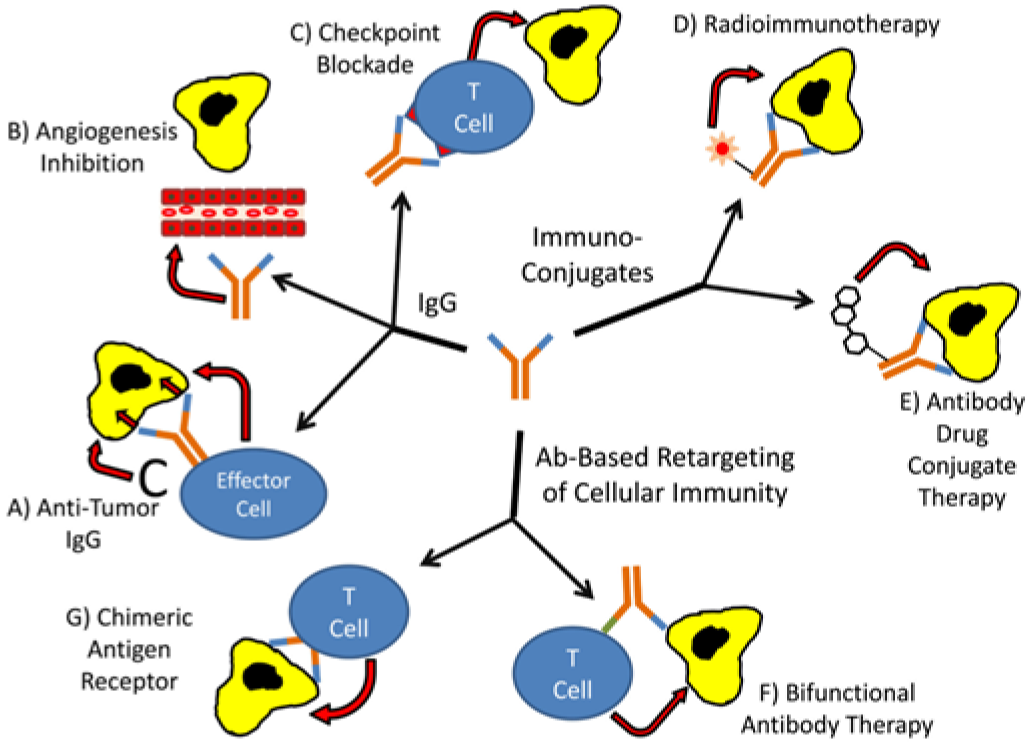

Figure 1.2 : Monoclonal antibody (mAb) based strategies against cancer. Biocompatibility and versatility of antibodies have allowed for the development of many therapeutic strategies against cancer. Three main groups can be distinguished among these approaches: those directly blocking processes occurring within or due to tumoral cells **(A, B, C)**, immunoconjugation for local delivery of drugs or radioactive molecules **(D, E)** and retargeting based strategies **(F, G)** in which the immune system is directly helped to combat the disease. Adapted from Kaplon & Reichert, 2018.

1.3 Multispecific antibodies

Bi- or multivalency in natural antibodies is not uncommon; in fact molecules like IgM can deliberately keep their affinity to ligands low in order to broaden the spectrum of antigens to which they can bind (Ghosh & Campbell, 1986). However, specificities are identical on both Fab arms across virtually all types of antibodies, meaning that there is no non-artificial immunoglobulin that is not monospecific.

However, this does not imply that artificial synthesis of bispecific (or multispecific) antibodies is not possible. In fact, in the last few years many viable methods including chemical conjugation (Weir et al., 2002), hybrid hybridomas (Milstein & Cuello, 1983) or the more modern recombinant DNA technology (Riechmann et al., 1988) have been developed to generate an overwhelming amount of artificial formats. These techniques have allowed the synthesis of multispecific antibody formats with well-defined structure, functions and pharmacological properties. Applications of these antibodies are not only limited to therapy.

Indeed, many of these formats are starting to be used in other areas like imaging, prophylaxis or diagnosis. Nonetheless, therapeutic use is a priority and as of 2018, more than 20 bispecific antibody platforms have been approved for clinical use or clinical trials (Godar et al., 2018).

Among the many advantages bispecific antibodies bring is not having to resort to combination therapy (*i.e.* the use of more than one mAbs) to block, activate or retarget different molecules. This not only reduces the limits in ratio and molecule amounts on therapy, but also translates into quicker, less complex drug manufacturing, preclinical and clinical trials (Kontermann & Brinkmann, 2015). Nevertheless, there are also challenges associated with multispecific antibody use, namely making sure the sample is completely pure and reducing solution viscosity, the latter increasing with antibody size. Moreover, as the molecular weight of bispecific antibodies currently ranges between 55 and 300 KDa (Brinkmann & Kontermann, 2017), challenges of each format must be addressed separately, as parameters such as half-lives, specificities or viscosities will be different from one multispecific antibody to another.

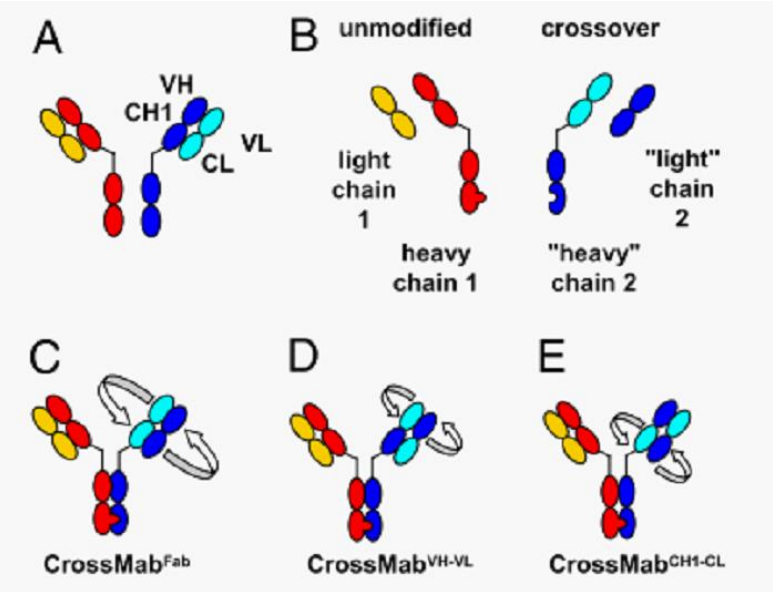

Figure 1.3 : The CrossMab technology for the generation of bispecific antibodies. Fab domain exchange is combined with the knobs-in-holes (KiH) technology to produce different antibodies. Heavy chains are represented in dark red and blue and light chains in cyan and yellow. First, two sets of heavy and light chains are designed **(A)** and the two halves are heterodimerized by the KiH **(B)**. From there, three types of crossovers can happen for generating CrossMabs: full VH-CH1 and VL-CL **(C),** VH-VL only **(D)** or CH1-CL only **(E).**

As mentioned above, there are many strategies for developing bispecific antibodies, including the CrossMAb technology (Klein et al., 2016) which was developed because, even though heavy chain heterodimerization had already been achieved using the knobs-in-holes (KiH) technique (Ridgway et al., 1996), correct light chain heterodimerization was still an unsolved challenge. The CrossMAb format uses a “crossover” technique that consists in exchanging the heavy and light chains in an antibody Fab to make them different enough so that incorrect pairing can no longer occur (**Figure 1.3**).

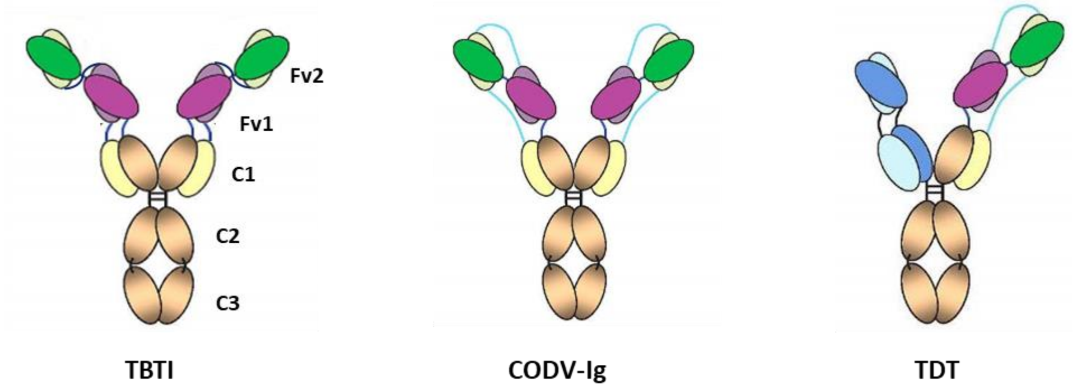

Figure 1.4 : Schematic representation of the multispecific antibodies used in the project. TBTI and CODV have the same number of domains and linkers, but the main difference lies on how the domains are connected by those linkers. In TDT, the antibody is formed by half a CODV and half an anti-TNF-alpha IgG.

1.3.1 TBTI (DVD-Ig) CrossMabs

The dual-variable domain immunoglobulin (DVD-Ig) format (Wu et al., 2007), which is representative of the CrossMab technology, also solves the limitation of Fv instability which occurs when peptide-linking adjacent heavy or light chains to develop multispecific antibodies. As opposed to previous attempts at stabilization by addition of disulphide bridges or interface interactions which only caused issues such as increased aggregation propensity, DVD-Ig formats extend either heavy or light chains by adding a linker to the N-terminal of the Fv without inherently compromising stability or interactions. The result is an antibody consisting of two interconnected Fvs on a Fab, but in which only Fv_1 is directly linked to C1 (Jakob et al., 2013) (**Figures 1.4, 1.5**). A disadvantage of the DVD-Ig format, however, is that positional effects, mean that ligand affinity on Fv_1 is reduced in comparison with Fv_2, which is likely to attain parental antibody-level affinities (Kontermann & Brinkmann, 2015).

1.3.2 CODV CrossMabs

As implied above, CrossMab technology is promising. However, a challenge lies in the loss of affinity of domains due to their position in the molecule (more commonly known as positional effect), which hinders its use in the development of a universal format for therapeutic use. The cross-over dual variable immunoglobulin (CODV) (Steinmetz et al., 2016) is a recently developed format that aims at tacking these difficulties.

As with the DVD-Ig format, CODV extends the light and heavy chains by the N-terminus with a series of linkers to generate dual-Fv Fabs. In the DVD-Ig format, the linkers connect CH_1 and CL only to Fv_1 and Fv_1 to Fv_2. However, in the CODV format these all-glycine linkers connect CL to Fv_2 instead of Fv_1, which give the format a self-supported architecture (**Figures 1.4, 1.5**). The linkers are numbered depending on which domains they link: 1 for the light chains of the Fvs, 2 for CL-Fv_2, 3 for the heavy chains of the Fvs and 4 for CH-Fv_1. These four linkers have been experimentally tested with different lengths and compositions and the optimal construct was defined to have L1 to L4 lengths of 7, 5, 1 and 2 glycine residues, respectively (Steinmetz et al., 2016). Nonetheless, it is not the only possible length; other Fab and target combinations have also reported success with L1 to L4 lengths of 10-0-10-0 residues (Steinmetz et al., 2016).

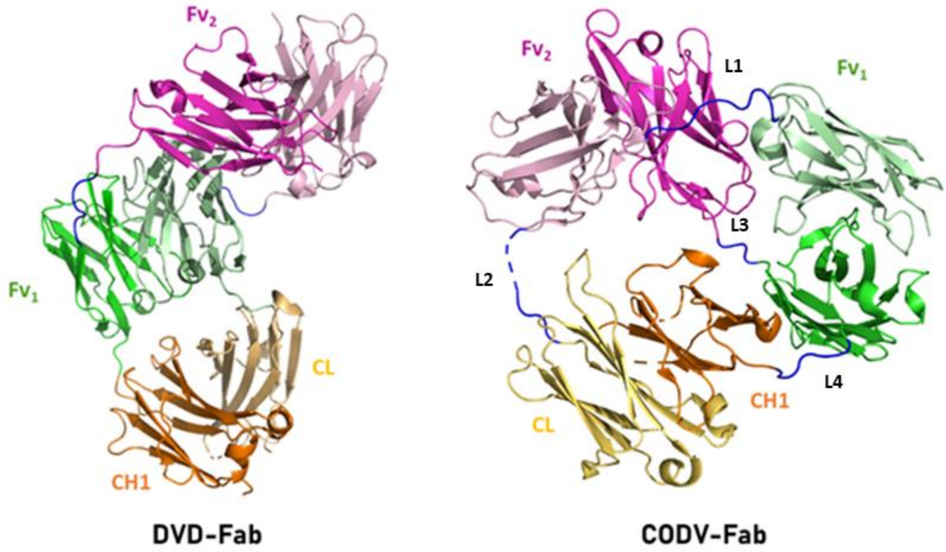

Figure 1.5 : Crystal structure comparison between the Fabs of DVD-Ig and CODV format multispecific antibodies. Both structures present the same number of domains (CH1-CL-Fv1-Fv2), but the linker system of CODV-Fab is more complex than in DVD-Fab. The linkers in DVD-Fab further extend the arms in length, but Fv2 is prone to a “saddle-like” movement that may obstruct antigen binding to Fv1. In CODV-Fab, linkers generate a circular self-supporting truss that provide stability to the Fabs as opposed to DVD while allowing independent and unobstructed binding to both Fv. Adapted from PDB entries 4HJJ (Jakob et al. 2013) and 5HCG (Steinmetz et al. 2016).

As a result of its 4 artificial linkers, the 3D architecture of CODV Fabs is a complex and self-supporting circular scaffold in which the stability of each domain is guaranteed, and domain-level flexibility is restricted. Moreover, the crystal structure of a CODV antibody suggested that there is no apparent inter-Fab or intra-Fab obstruction, and that CODV could bind different antigens independently with no positional effects. This hypothesis was supported by surface plasmon resonance (SPR) experiments performed with a CODV, specifically designed to simultaneously recognise interleukins 4 (IL4) and 13 (IL13), well-known targets for anti-cancer and anti-allergy therapeutic strategies (Mueller et al., 2002). These studies (**Figure 1.6**) demonstrated that adding the ligands IL4 or IL13 to $\text{CODV}_{\text{IL4 x IL13}}$ did not affect the binding affinity of the second antigen, regardless of order or saturating concentrations, thus confirming the absence of a CODV-related allosteric or cooperative antigen recognition mechanism.

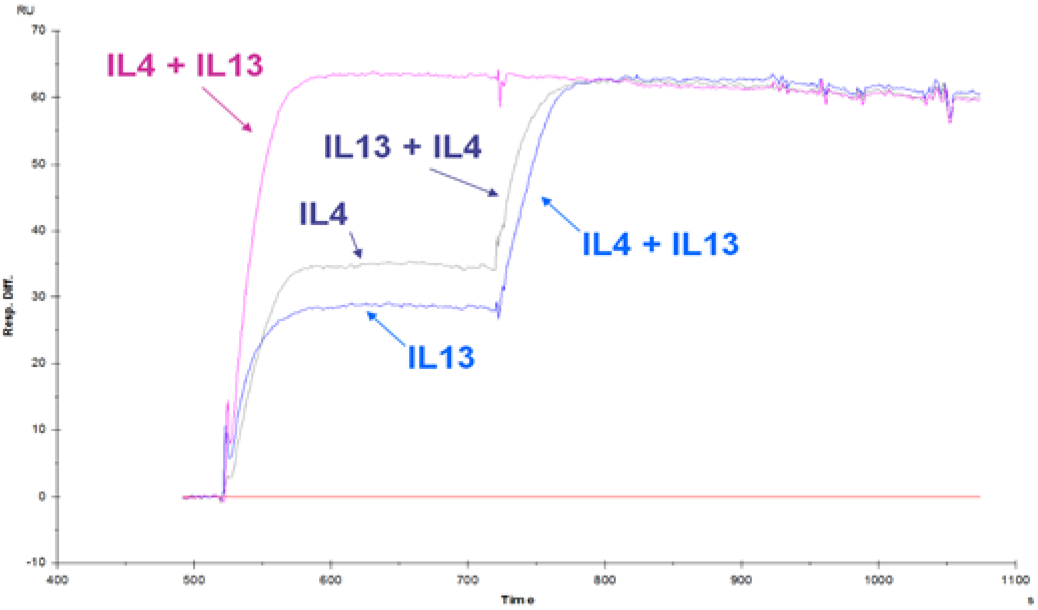

Figure 1.6 : SPR sensograms of CODV binding to IL4 and IL13. In this experiment, ausence of positional effect in antigen binding is shown. The baseline is represented in red. IL4 and IL13 were first added at the same time to generate a maximum response curve in which occupancy of CODV paratopes is maximum (magenta). In the next experiment, IL4 was added first and once everything seemed bound, IL13 (gray). Signal reached the maximum response. Similarly, the order of antigens was inverted and the same response was obtained (blue) this showing that there is indeed no positional effect. Adapted from the supplementary material in Steinmetz et. al, 2016.

Adding both ligands at the same time results in a uniform and fast signal plateau that is unchanged over time (**Figure 1.6**), thus suggesting an independence of antigen binding by the antibody. The median K_Ds measured in the SPR experiments construct was 6 pM for IL4 and 60 pM for IL13, effectively the same as the parental antibodies.

However, even though CODV antigen binding shows no positional effect in vitro, this is not the case when trials are carried in cellulo or in vivo (Steinmetz et al., 2016). There thus remains a need for understanding the three-dimensional structure of CODV, in particular relating to the relative orientations of its antigen binding sites or paratopes, at a full antibody level and under near-native conditions.

1.3.3 TDT

TDT is a trispecific antibody which can also be classified as belonging to the CrossMab family. TDT is formed by CODV and IgG antibodies each of which may have different paratopes. This leads to the potential binding of three targets which might be important when targeting, for example, complex tumoral or viral escape mechanisms. As a novel molecule, there is not yet much research regarding its molecular activities.

1.4 Interleukins 4 and 13 and their role in cancer

The simultaneous targeting of IL4 and IL13, small globular α/β proteins (Walter et al., 1992) with molecular weights of 14.9 KDa and 12.6 KDa, respectively, by a single CODV is an excellent example of the possibilities that the development of multispecific antibodies opens up in biomedicine.

IL4 is a cytokine that is produced by an array of cells of the immune system, primarily by Th2 cells but also by eosinophils, basophils and mast cells. It has been shown to have many roles in the field of immunity: it may induce class switching to IgE in effector B-cells (crucial in the allergic response), it may play a role in B-cell and T-cell proliferation, and macrophage activation and it also plays a very important role in brain functions such as memory and learning (Gadani et al., 2012). It is also a downregulator of Interferon γ synthesis and macrophage proliferation or activation of Th1 cells, which are critical in the generation of immunological memory.

High-levels of IL4 have also been detected in the microenvironment of tumors and many studies have proved that such an increase in IL4 helps induce tumor growth or proliferation, as well as preventing classical mechanisms of apoptotic induction (Oh et al., 2010).

To better understand the biological roles of IL4 and IL13, their receptors should be introduced. There are two types of IL4 receptor (IL-4R)(Suzuki et al., 2015). Type 1 IL-4Rα binds exclusively to IL4 and is generally involved in signalling pathways concerning allergies or inflammation. Type 2 IL-4Rα is involved in the JAK/STAT pathway (**Figure 1.7**), which starts with activation of Janus kinases (JAK) by the ligand-receptor binding and ultimately ends, after a cascade of signals, in the activation of the Signal Transducer and Activator of Transcription (STAT) (Viganò et al., 2018). Excessive activation of some of these STAT complexes (namely STAT-3 and STAT-6) has been associated with malignancy of tumors, such as in breast cancer or melanoma. STAT-6 is also of great therapeutic interest as, along with other genes, it induces the expression of BCL2L1/BCL-X(L), two very strong anti-apoptotic mediators (Viganò et al., 2018; Walford & Doherty, 2013).

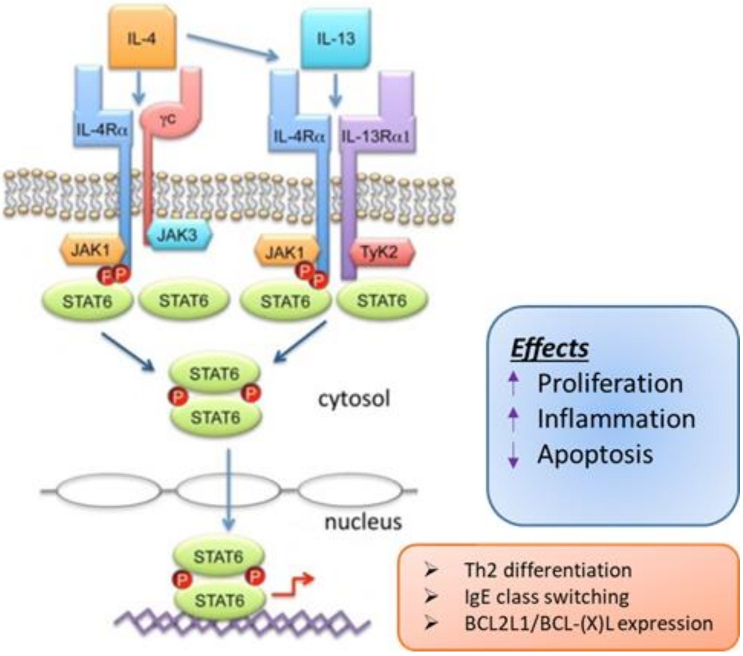

Figure 1.7 : Schematic representation of the JAK/STAT6 signalling pathway by IL4 and IL13. IL4 can bind to an IL-4Rα/γC receptor or to an IL-4Rα/IL-13Rα1 heterodimer, which activates JAK1/JAK3 or JAK1/TyK2 to subsequently phosphorylate STAT6. Phosphorylated STAT6 molecules dimerize, travel to the nucleus and lead the transcription of genes related to anti-apoptosis, cell proliferation and tissue inflammation. Adapted from Rawlings et. al, 2004.

IL4 receptors bind to both IL4 and IL13 which also has its own receptor, (IL-13R), and in many cases, these two cytokines have overlapping functions (**i.e.** regulation of the JAK/STAT pathway, **Figure 1.7**), making them an example for which combination therapy might prove a useful approach. Here, multispecific antibodies such as CODV could eliminate the need to develop molecules targeting IL4 and IL13 separately and could form the basis for an effective antitumor treatment.

1.5 Electron microscopy

X-ray crystallography as applied to biological macromolecules (MX) has proven to be a very efficient technique for high-resolution structure determination of many proteins and is widely used in many fields including pharmacology (Smyth & Martin, 2000). Nevertheless, MX has many limitations, particularly when it comes to addressing the dynamics and conformational flexibility that may be very important in determining mechanisms leading to biological function. Moreover, crystallisation conditions are often far from real physiological environment in which a biological macromolecule would normally find itself. While Small-Angle X-ray Scattering can address some of these areas, it provides only low-resolution structural information (Brosey & Tainer, 2019) and, until recently, there were no techniques that could provide such information at resolutions close to those achievable in MX. However, recent advances in the field of cryo-electron microscopy (Cryo-EM) (Merk et al., 2016) (see also section **1.6**) mean that this technique can now provide high resolution information concerning the dynamics and conformational flexibility of large biological macromolecules. For this reason, cryo-EM was chosen as the technique of choice for the structural investigations of CODV bispecific antibodies described in this thesis manuscript.

1.5.1 Electron microscopes

The transmission electron microscope (TEM) is a type of microscope in which the illuminating source are electrons from an electron gun (Williams & Carter, 1996) (**Figure 1.8**).

In TEM microscopes the electron source is either filament based (tungsten, LaB6, etc) or, more recently, a Field Emission Gun (FEG)(Crewe et al., 1968). The latter is found in high energy microscopes and generates an electron beam which is smaller in diameter, more coherent, denser and brighter beam than that generated by a tungsten filament. As electrons are very sensitive to deflection by air molecules electron microscope are kept under constant vacuum conditions to allow the illuminating source to correctly reach the specimen.

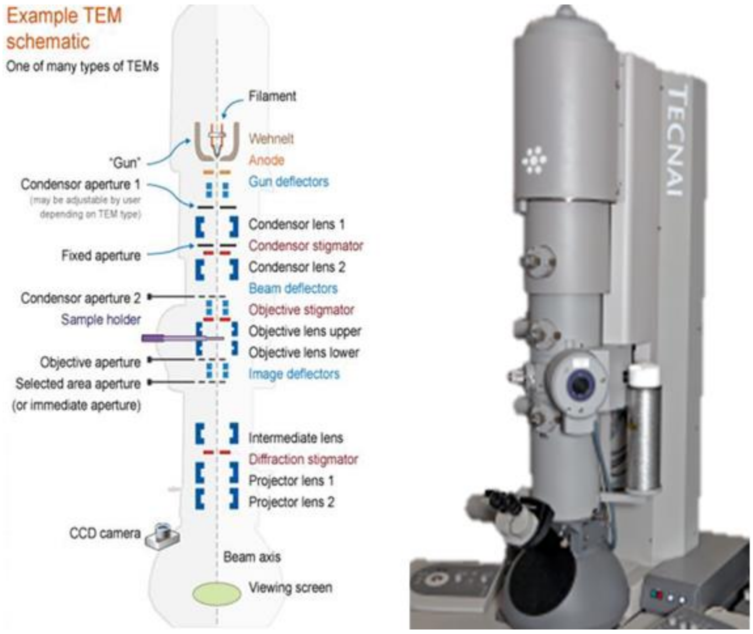

Figure 1.8 : Diagram of a transmission electron microscope and its components. The microscope represented in this figure is a 120 kV Tecnai G-20 cryo-electron microscope used in some of the work described here. Components described on the left show a general approach and may change with each different microscope. Adapted from (http://www.ammrf.org.au/myscope/tem/introduction/)

As in optical microscopes, TEMs use objective, condenser and projector lenses to magnify and focus the illumination source and projected images. However, the lenses are electromagnetic, instead of glass, and more than one of these is usually required to focus the electron beam. TEMs are also equipped with deflector coils which allow for the illuminating beam to be moved to a specific area of the specimen which is imaged using camera (or 'detector') systems. Nowadays, cameras installed in TEMs are usually either CCD (charge-coupled device) or direct detection (DE) instruments. In CCDs the signal resulting from electrons impinging on a photoactive region are converted into digital pixel values. While more sensitive that recording of the signal on films, this process generates noise, which can sometimes obscure small signals. This problem is obviated with DE cameras, based on relatively new technology (Milazzo et al., 2011). Indeed, the advent of DE cameras for electron microscopy has been one of the driving forces behind the recent EM 'resolution revolution' (Kühlbrandt, 2014).

1.6 Cryo-Electron Microscopy

Cryo-electron microscopy is a low-temperature technique based on sample vitrification and was first described by Jacques Dubochet in 1981 (Dubochet & McDowall, 1981). This protocol for obtaining vitreous water for EM was successfullt first published and applied to biological specimens (viruses) a short time later (Adrian et al., 1984).

As implied above, in cryo-EM experiments samples are vitrified prior to imaging in order to preserve the sample in near-native conditions and reduce radiation damage. No stain is used to provide contrast and, instead it is the scattering of electrons from the sample itself that provides the signal. Vitrification is a process in which a specimen is quickly introduced into a liquid cryogen (such as ethane) so that the water achieves a vitreous state (Dubochet & McDowall, 1981). As long as the temperature of the grid is continuously kept low the sample will be fixed and immobile in a near physiological environment while still keeping the ability to wobble, since the vitrified water is not strictly solid. This state can also give information about the dynamics of the protein studied, since the movement allowed by the vitrified ice can trap the protein molecules in different conformations. A major issue in cryo-EM experiments is that signal to noise (S/N) ratio is naturally low. This is for two main reasons: the lack of contrast due to the lack of stain, and the presence of higher noise due to a low electron dose applied in order to reduce damage to radiation sensitive biological molecules.

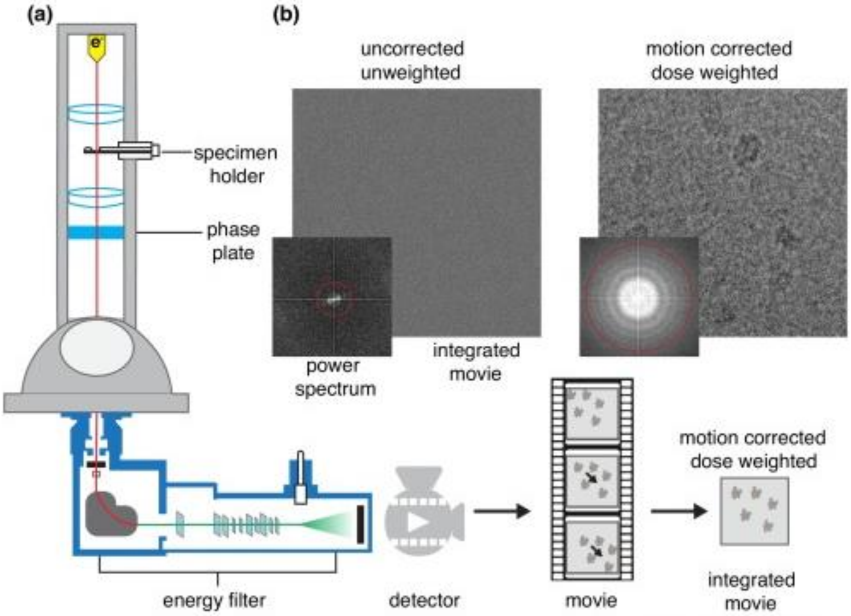

Figure 1.9 : (A) Schematic representation of a TEM, equipped with energy filter and phase plate. The detector collects stacks of frames after the filter removes inelastic electrons **(B)** Transition from uncorrected movies, to aligned averaged frame stacks. Reproduced from Elmlund et al 2017.

The latter has been addressed quite efficiently by the contemporary direct electron detector technology that allows to the collection of “movies”, in which a large total dose is divided into multiple frames. Each frame receives a dose to provide sufficient S/N ratios to identify particles but which is not high enough to heat and induce melting of the vitrified ice. However, the accumulated dose between successive frames result in the movement of the particles embedded in the ice and estimating and correcting for this movement between successive frames and finally adding all the frames to a single micrograph, thereby boosting the S/N ratio to a far better level has been crucial to the cryo-EM 'resolution revolution'. (**Figure 1.9B**). Other factors which have been important in this phenomenon are the use of energy filters (**Figure 1.9A**) (Grimm et al., 1996) to reduce noise contributed by inelastically scattered electrons, and improved methods of phase contrast that help the sample stand out at high contrast from its vitrified environment.

Regarding this latter aspect, originally Defocus Phase Contrast methods exploiting optical aberrations such as spherical aberrations of defocus were used to generate intensity variations in the same specimen. This has the limitation of being inefficient in low-frequency areas and sacrificing resolution to generate contrast (Nagayama & Danev, 2009). Nowadays, especially in Cryo-EM experiments, a device called a phase plate is frequently used to generate phase contrast (Nagayama & Danev, 2009). These modulate the electron wave into different sets of phases to allow for better contrast in images without sacrificing resolution (**Figure 1.10**). The most effective to date is a thin amorphous carbon film plate, called the Volta phase plate (Danev & Baumeister, 2016) that is located at the same level as the objective aperture in a microscope.

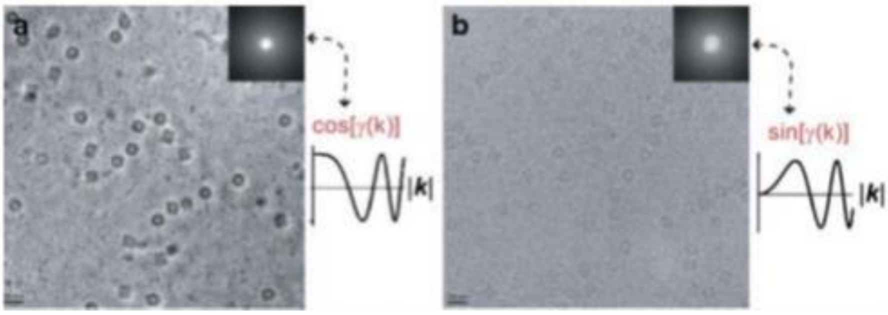

Figure 1.10 : Phase contrast generated from a phase-plate. The same beam may be modulated into a cosine (s) or sine (b) wave function to produce images of very different contrast, which may help especially when working with small molecules or very low-dose conditions. Reproduced from Nagayama and Danev, 2009.

1.7 Sample Preparation for cryo-EM

Vitrification (**Figure 1.11B**) is a process in which particles in an aqueous state are rapidly frozen into an optically transparent amorphous ice, which allows for scattering of the electrons from the particles themselves to form a contrasted image. This special state of water can only be achieved if the solution cools down so fast that crystalline ice does not have time to form.

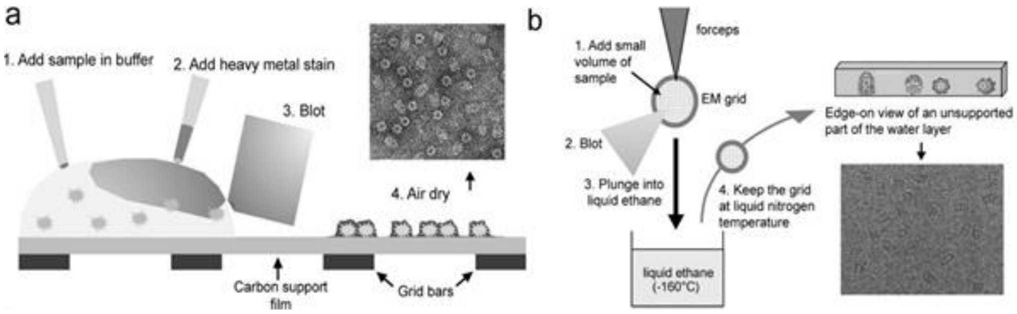

Figure 1.11 The two different techniques used for single-particle electron microscopy sample preparation. Negative staining **(a)** may be performed at room temperature by addition of a heavy atom solution onto a protein sample. Blotting and air drying will fix the specimen onto the carbon for imaging. In vitrification **(b),** sample is added to a grid under humid conditions, and after blotting, the grid will be quickly plunged into liquid ethane in order to vitrify the solution by taking advantage of the unusual freezing properties of water. Adapted from Orlova and Saibil, 2011.

While it was considered not possible for a long time, it was shown (Brüggeller & Mayer, 1980) that for correct vitrification of water two factors are key: a fast coolant (such as liquid ethane) and a small sample volume (very thin layers of water or aerosols). Once vitreous ice is formed, the sample has to be kept within a range of low temperatures; otherwise, the water will irreversibly transform into other states, such as cubic or hexagonal ice, which will not allow to identify particles.

The sample vitrification process for cryo-EM starts by applying a small volume of sample into a 'holey' support held by a 3 millimeter metallic grid. The sample is adsorbed onto the support and the thickness of the solution thinned by blotting with a filter paper. Finally, the grid containing the thin layer of sample is quickly plunged into cooled liquid ethane. The grid is then transferred into liquid nitrogen for storage purposes or direct use in EM. Today, vitrification is performed in a semi-automatic manner with the aid of a plunge-freezing machine (**Figure 1.12**), which contains a chamber for blotting and temperature and humidity preservation; and a fast-plunging arm that will lower the grid onto the liquid ethane container. After the grid is frozen it must be clipped before it is loaded into the microscope, so that it will be held in place when inside the column vacuum. The clipping method varies depending on the microscope used.

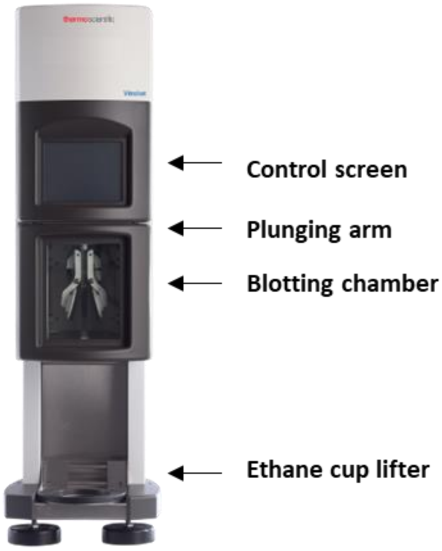

Figure 1.12 : Schematic of a plunge-freezing robot. Example of a Vitrobot Mark IV and its main components. The gridboxes are placed in the ethane cup, which will be lifted towards the blotting chamber. The grid is placed in the plunging arm and after applying the sample, the blotting arms (white) will blot the grid and it will be plunged into the ethane. Reproduced from (https://www.thermofisher.com/ch/en/home/electron-microscopy/products/sample-preparation-equipment-em/vitrobot-system.html).

The grids used for cryo-EM (**Figure 1.13A**) are typically holey grids with copper or gold-based support, with its most-used film of choice being carbon or gold. While gold supports are more expensive, they offer several advantages (no cytotoxicity, reduced support wrinkling and movement due thermal contraction) compared to copper supports. However, when used as a film of choice, gold has the disadvantage that it does not produce Thon rings in the Fourier transforms (or FTs) of the microscope images, which makes crucial tasks such as direct alignments of the microscope during EM data collection setup more difficult. These holey grids are available in many shapes, thicknesses, hole sizes and hole spacings, each of them more or less suited for the system that will be studied (**Figure 1.13B**).

When preparing sample grids for EM experiments, in addition to obtaining a vitreous ice as thin as possible while embedding a single layer of the particle of interest, which will enable higher contrast, a good particle spread and population per image is also highly-desired. Finally, it is also imperative to have the particles in different orientations throughout the ice. As the image processing step of the project will reconstruct a 3D map from 2D projections using Fourier Transform, there is a need for particles (2D projections) to populate as many different views as possible in order to cover the entire Fourier volume and to generate a correct reconstruction. Missing views (also known as preferential orientations) will lead to anisotropic resolution in the resulting reconstruction (Sigworth, 2016).

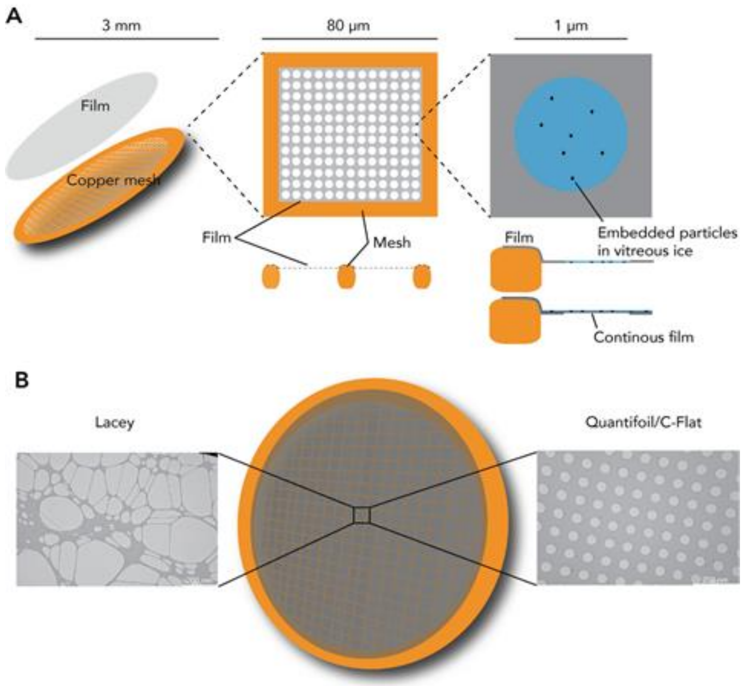

Figure 1.13: Schematic representation of a grid used in cryo-EM. (A) A 3 mm metallic mesh is covered by a support or film of choice. The grid is divided into squares, which in turn are divided into holes, where the particles are embedded on ice. **(B)** Two families of supports for EM: Lacey supports, where the size and spacing of each hole is arbitrary; and Quantifoil/C-Flat type supports, where hole size and spacing is consistent throughout the grid. Adapted from Brillault and Landsberg, 2020.

Blot settings, sample volume and support choice will regulate the thickness of the ice optimal for the sample to be studied. Similarly, sample concentration and buffer composition are some of the factors that will lead to correct particle spread. When molecules exhibit a high preference for the carbon support as opposed to going into the holes, or tend to gather close together, strategies like coating the grid with a graphene oxide layer might be helpful. Particle orientations however, will completely vary from target to target. In some cases, the molecule will naturally lay in different orientations throughout the ice (**Figure 1.14C**), in other cases, particles will adopt only one or few preferential orientations when populating the holes (**Figure 1.14B**). There are other strategies such as the addition of buffer additives and grid treatments that are continuously developed to tackle this issue; it is however a case-by-case scenario and generalizations cannot be made. In cases where preferential orientation still remains an unsolved issue, a tilted-stage data collection is typically attempted.

One of the main challenges during the plunge-freezing step is that it may induce sample aggregation (**Figure 1.14A**). Blotting conditions are usually harsh for proteins and molecules being forced together into a thin layer of ice often translates into contact with the air-water interface, resulting in clustering of hydrophobic residues leading to denaturation and aggregation of the molecules. Minimizing the effect of this phenomenon in the sample is the main focus of much research at the moment (D'Imprima et al., 2019). Glow-discharging or plasma treatment of the grids can help increase the propensity of the support to adsorb protein molecules. Glow discharging is a process in which an electrical current is applied to the grid in order to ionize the support (Aebi & Pollard, 1987). This process causes the support to become more hydrophilic. Other solutions which can be explored to reduce the possibility of sample aggregation are the use of additives such as detergents and state-of-the-art jet-based freezing techniques such as Spotiton (Jain et al., 2012) which do not use a blotting step (Brillault & Landsberg, 2020).

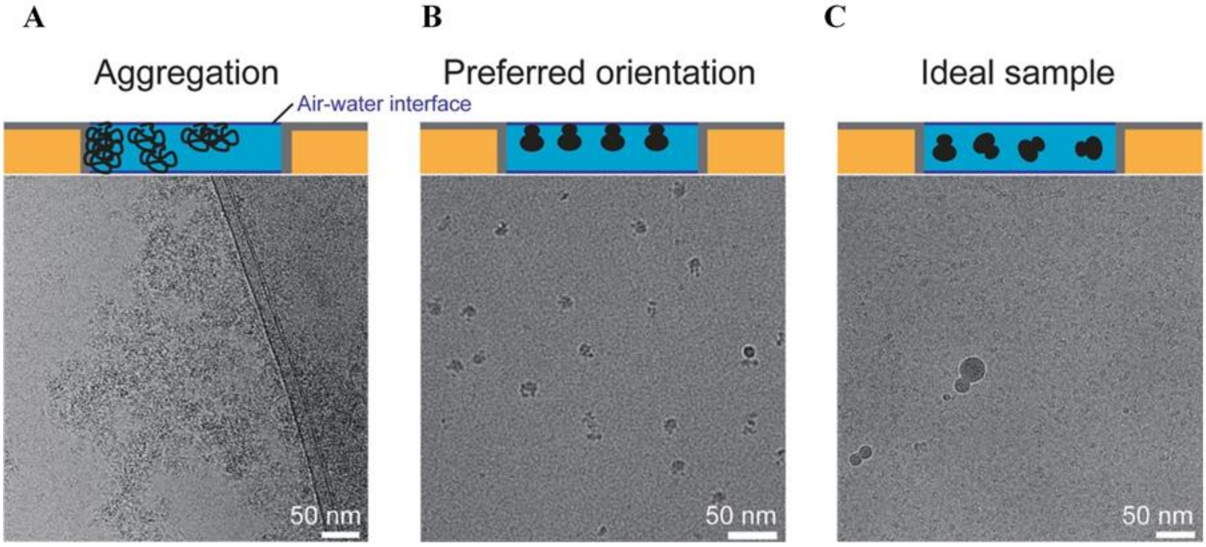

Figure 1.14 : Representative micrographs corresponding to outcomes from the sample vitrification step. **(A)** Particles can aggregate when having their hydrophobic pockets exposed by contact with the air-water interface. **(B)** They can also be forced into one orientation during the plunge freezing**.** **(C)** The ideal micrograph should have correct spread of particles in different orientations, so that image processing can succeed. Adapted from Brillault and Landsberg, 2020.

1.8 Single Particle Analysis (SPA) cryo-EM:

Image processing in SPA includes number of steps and variables to consider before obtaining a scientifically accurate model of the biomolecule under study. A standard EM processing pipeline is shown in (**Figure 1.15**).

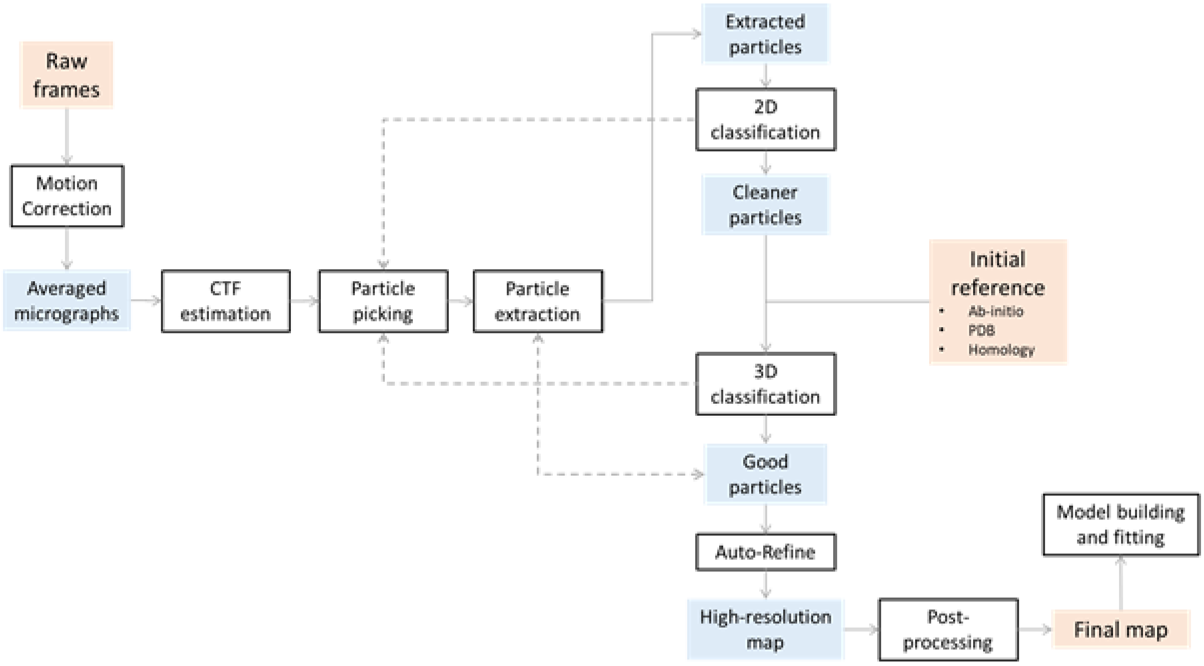

Figure 1.15 : General workflow of single particle image processing. Arrows indicate the flow of the process needed to follow to obtain a final map from initial raw frames collected in the microscope. Dashed arrows refer to optional steps that are usually taken, early per-particle CTF estimation in tilted data and re-extraction of particles for high quality reconstructions.

1.8.1 Motion Correction

The motion induced by the interaction of the vitrified ice with the beam causes the particles to move leading to image drift or blurring that places a hard limit on achievable map resolution. As already noted in section **1.5.1**, the advent of Direct electron detection (DE) cameras has allowed for the development of algorithms for the correction of this (Li et al., 2013). Indeed, on microscopes equipped with DEs, these cameras are used to record ‘movies’, composed of several frames (typically 10 to 40). Each frame is of short-exposure (0.1 to 0.2 seconds), which are used to monitor the discrete particle movement frame-to-frame. These frames are then aligned and compiled into a single micrograph with a higher S/N ratio than would otherwise have been the case.

The first frames of a movie, even at low doses, usually experience strong electron beam-induced motion, which gradually decreases until virtually stabilizing towards the final frames of the movie. This occurs mainly because of the built-up stress during vitrification, and radiation relieves some of it, causing motion (Glaeser, 2016). On the contrary, beam-induced damage to the sample is lower during the first frames because of the lower accumulated electron dose. The most widely used programs such as MotionCor2 (Zheng et al., 2017) use a dose-weighting scheme, in which more weight is given to the first frames due to these containing a higher amount of high-resolution information.

1.8.2 CTF estimation

The image of the sample that is acquired does not strictly correspond to the real image that one would see should they possess an ideal imaging device that does not distort or lose any information. The image formed by an electron microscope is a convolution between the true object and the Point Spread Function (PSF) of the microscope, PSF depends on numerical aperture and wavelength of the microscope.

The Fourier transform (FT) of the PSF is the Contrast Transfer Function (CTF) (Mindell & Grigorieff, 2003), which and can be estimated by the following equation:

$$\mathrm{CTF}(f) = E(f)\,\sin\left(\pi\ Cs\ \lambda^3\ f^4/2 - \pi\,\lambda\,d\,f^2\right)$$

where *E(f)* is the envelope function that describes the attenuation of high-resolution information as a function of frequency (fainter rings at higher frequencies), *Cs* the spherical aberration of the microscope, *λ* the wavelength of the electrons, *f* the spatial frequency and *d* is the defocus (always in negative as images are collected under-focus in SPA).

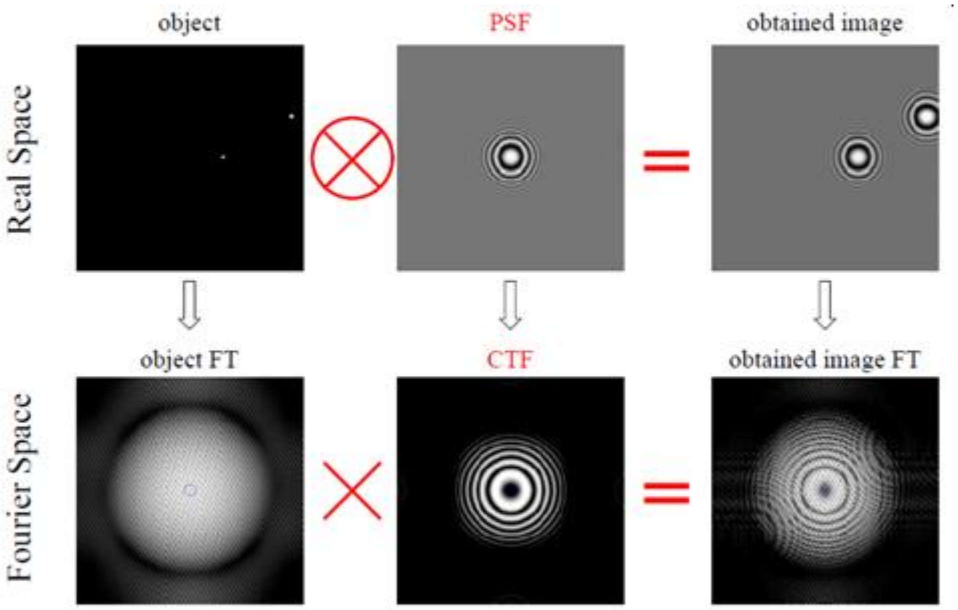

Figure 1.16 : Relationship between real space and Fourier space data. Top row: The image obtained by a microscope is the convolution between the real object and the point spread function. Bottom row: When calculating the FT of the image, Thon rings are present as a result of the presence of the CTF. Estimating the CTF allows the deconvolution of the FT and obtain the real object.

Thus, CTF represents the modulation of the FT of the image as a function of defocus and in the power spectrum of the image, the CTF exhibits as concentric bright and dark rings known as 'Thon' rings. The bright rings correspond to the maxima of the CTF function and the minima represents the spatial frequencies with no signal. Before micrographs are considered for image analysis, it is crucial to inspect for the quality of the CTF and estimate the CTF parameters including defocus and astigmatism as much accurately as possible. (**Figure 1.16**).

1.8.3 Particle picking and extraction

An important and sensitive task in SPA is the identification of images of the target of interest in a micrograph. This can be done either manually or automatically. Automatic particle picking can be done either ab-initio or by starting from a template containing few representative projections. With recent developments in the SPA field, the total number of micrographs acquired for a single data set is so high that a complete manual picking is tedious. Thus, in most cases, particle picking includes a first manual step followed by automated picking.

In manual picking procedures, particles are picked visually based on prior knowledge of their size, oligomeric nature, etc. This is a tedious step but fruitful in producing a set of references which will be used for automated picking. Usually, about 5000-10000 particles are manually picked.

Automated picking aims at drastically reducing the time needed for particle selection. Usually involving CPU or GPU-based calculations, automatic picking might lead to false positives and therefore requires additional cleaning steps.

There are different approaches to automated picking. The most common protocol involves creating templates from manually picked particles or existing structural models and using them as references for picking. Semi-automated picking, uses a machine learning-based approach that tries to emulate few manually picked particles (de la Rosa-Trevín et al., 2013; Wagner et al., 2018). Finally, fully automated picking algorithms are being improved based on Gaussian detection (Voss et al., 2009) or neural network databases (Tegunov & Cramer, 2018) and completely eliminate the need for any manual picking.

Once particles are picked, they can be extracted into a suitable box size. Larger box sizes will have more pixels for background calculations and a higher chance of containing the particle but will also be more prone to picking signal from neighbouring particles. Smaller box sizes, on the other hand, allow for the elimination of unnecessary noise and speed up calculations but will be prone to less accuracy in the determination of the background noise level, thereby potentially resulting in poor particle alignment and therefore are more commonly used in later stages of the image processing pipeline.

1.8.4 2D Classification

2D classification provides the first step towards identifying useable particles and visualizing the different views and conformations of the target molecule. For this thesis, images of individual particle are aligned and categorized into averaged groups (or classes) by cross-correlation using statistical algorithms such as maximum likelihood estimation. The resulting 2D class averages, if at higher resolutions (better than 8Å) can already allow the discernment of secondary structure elements or small conformational and structural changes.

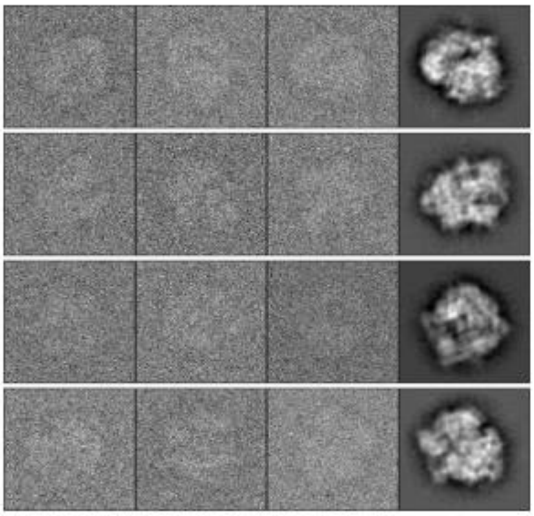

Figure 1.17: Comparison between individual particles and 2D averages. The first three columns of each row represent individual particles picked at random from within the same group (signal to noise ratio: 1/50). By aligning and grouping thousands of such particles together, a 2D average with higher signal can be obtained, which allows for better interpretation of views and conformations. Adapted from Ma et al., 2019.

From 2D classification, one can identify well-aligned and populated classes with diverse views and classes with different conformations, information that is crucial to separate data that will be used in the following 3D steps (Ma et al., 2019). One of the positive side effects of 2D classification is that unfit particles and contaminating ice and carbon are easily identified and removed. Since noise is random, cross-correlation with real particles, which share well-defined signal, will be low, and thus will be averaged out into easily identifiable classes, while those particles that share signal will produce higher S/N class averages (**Figure 1.17**).

Should sufficient views of good quality be obtained, particles from these classes can be used for the generation of a 3D model (Ma et al., 2019).

1.8.5 3D Model generation

In order to perform the image processing steps at a three-dimensional level, a lower resolution surface must be first generated to be used as an initial model. An existing cryo-EM (single particle or tomography reconstruction), crystal structure or a SAXS model can serve as a good initial choice. If this is not possible, there are diverse algorithms that can be used to generate a 3D reference *ab-initio.*

The method used mostly in this thesis for the *ab-initio* generation of initial models is based on Stochastic Gradient Descent (SGD) (Bottou, 2010). SGD is a statistical iterative method based on approximations; whose objective is to determine a global minimum of a gradient descent function with a certain degree of confidence. The algorithm starts with a random value point (generally called *random seed*) and will iteratively calculate the regression function, which by definition is a function defined by a series of variables and weights, using above-said random value. The step-size at each iteration, which is linked to the algorithm's learning rate, will determine how fast a minimum is reached, however too big a step size may lead to false positives (or local minima).

The "stochastic" part of the algorithm's name alludes to a reduction in the data points used by each iteration. Because the amount of data points and features in cryo-EM is overwhelming and very computationally demanding, instead of using the entire range, the algorithm randomly selects a small number of them (called a *mini-batch*) at each iteration, saving a very high amount of calculations. Both the mini-batch size and the learning rate can be manually tuned to quickly arrive to an unbiased and reliable 3D *ab-initio* model.

1.8.6 3D Classification

The basis of 3D classification is essentially the same as 2D classification, consisting of grouping particles into classes that share the same features. In this case, however, particles are aligned against a 3D reference provided. Both in 3D classification and 3D refinement, a Bayesian approach is used to reconstruct maps from particle data. In order to find the correct reconstruction, the approach tries finding the model that has the highest probability of being the correct one considering both the observed data and available prior information. This probabilistic Bayesian approach iteratively learns most parameters of the statistical model from the data themselves, instead of needing expert input from the user at every step. The outputs of 3D classification are two: a series of classes containing all particles corresponding to views of the same model and a 3D model for each class generated by combining the aligned particles belonging to this class (**Figure 1.18**; Simonetti et al., 2008).

Particles belonging to individual classes are subsequently subjected to homologous 3D refinement to achieve the highest resolution possible. 3D classification is also very useful to solve heterogeneity issues within the particles (e.g. protein with and without ligand or inter-domain movements).

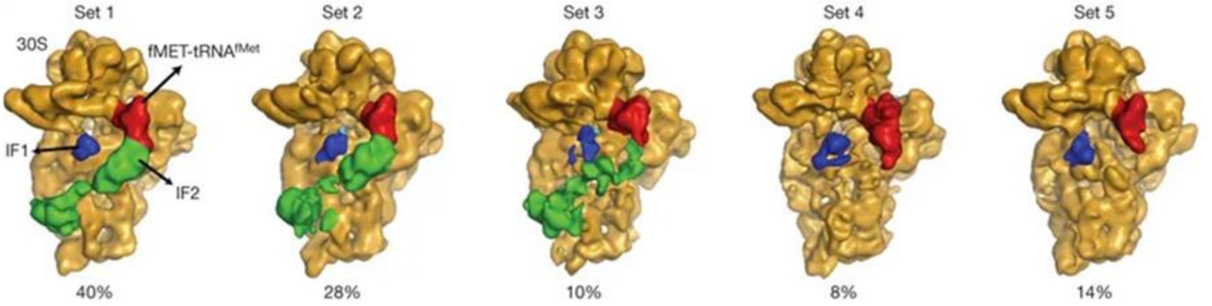

Figure 1.18 : Examples of maps obtained by 3D classification. Each of the maps contains a subset of the total number of particles (indicated by a percentage under the map). Although maps look similar at first glance, the heterogeneity of the particles make possible to discern between different conformational states of the 30S translation initiation complex. Adapted from Simonetti et al., 2008.

1.8.7 3D Refinement

The goal of 3D refinement is to obtain a reconstruction from a given set of particles at the highest possible resolution. Typically, a 3D model, either the ab-initio model or one of the 3D classes, is given as a reference, against which particles will be aligned.

There are many ways to assess the overfitting from 3D classification and refinement. It is based on a quality-measure concept called Fourier shell correlation (FSC) (Harauz & Van Heel, 1986). In this technique, the particle dataset is divided into two random and independent half-sets and for each half-set a 3D reconstruction is performed. At each iteration, the Fourier shells (the shell obtained by combining the Fourier transform of each slice of the model (**Figure 1.19**)) of the two reconstructions are cross-correlated. When these models are low-resolution, the correlation tends to be high, and this value will gradually decrease as higher-resolution information are taken into consideration.

Traditionally, the resolution of the reconstruction (Van Heel & Schatz, 2005) was defined as the frequency value at which FSC is 0, the point in which the half-maps are completely divergent. However, during the past two decades, two other threshold values to most accurately determine a reconstruction’s resolution have been accepted: the point at which FSC is 0.5 (*i.e.* there is still enough information to interpret the 3D volume), and a more statistically accurate one that sets the FSC value at 0.143. The latter value makes reported resolutions more comparable to those reported in X-ray crystallography (Rosenthal & Henderson, 2003). Independent from this, FSC has recently evolved into what is known as "gold-standard" FSC (GSFSC) (Scheres & Chen, 2012), in which overestimation (overfitting) of FSC is avoided due to the reference map's noise bias. This bias is caused because a single model is used as a reference to determine orientations of the particles, and because it is the low-mid frequencies which dictate the orientation, noise can induce alignment errors that will lead to non-real densities.

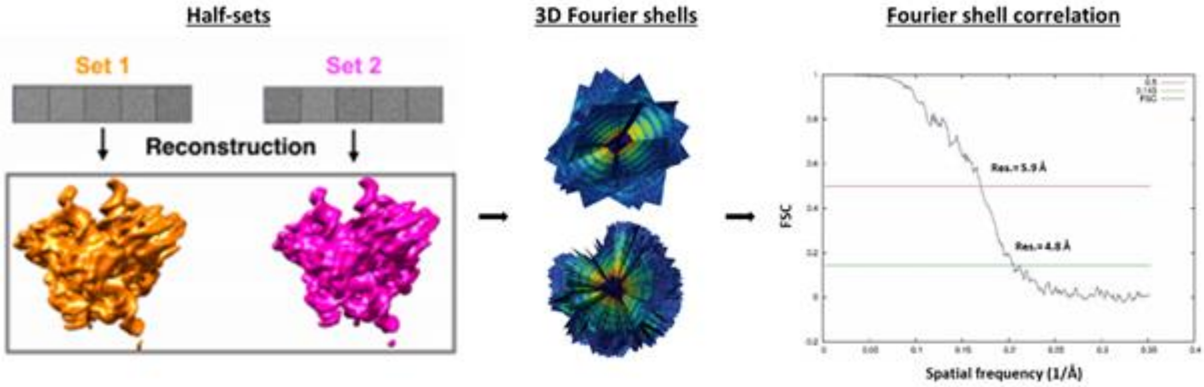

Figure 1.19 : Schematic representation of the Fourier Shell Correlation quality assessment procedure. The particle dataset is divided into two half-sets, which will be independently reconstructed into 3D half-maps. The FT of each map through all the possible orientations (Fourier shell), which contains all the frequencies up to the resolution limit, will be cross-correlated against each other. The resulting curve can be cut at different points to estimate the resolution of the map by interpolation.

It is important to consider that the Fourier shell correlation is a validation tool, and it should be viewed cautiously in that the masks employed in the 3D refinement step for example, can considerably change the resolution of the map depending of their tightness and shape.

1.8.8 Enhancement of the resolution – Polishing and Postprocessing:

An EM density map obtained after a successful step of 3D refinement is usually at the highest possible resolution the data allows. However, the resolution of the map can further be improved. This postprocessing step typically involves using diverse programs to improve the resolution of the target map and usually involves two main processes.

In per-particle CTF estimation, an attempt is made to calculate the real CTF defocus values for each particle. While having the CTF value of the micrograph is an acceptable approximation up until the 3D refinement step, differences in ice thickness, directly affect the defocus values at different points of the micrographs. Estimating these per-particle CTF values is a necessary step to better resolve the target map. In addition, when working on a tilted dataset, this difference in defocus values is higher throughout the micrograph, and this method is thus integrated into the pipeline before the 2D classification step.

In per-particle motion correction, an attempt is made to correct for the independent movement of each particle in a micrograph. Estimating and correcting the movement of every particle throughout a series of frames is very computationally intensive and many different approaches have been presented in order to perform it. For instance, in the Bayesian polishing approach (Scheres, 2012) implemented in RELION 3, micrographs are divided into small patches and beam-induced movement velocity vectors are statistically estimated. Additionally, radiation damage will affect the high-resolution information in the last frames of each movie, and a weight is given to each frame depending on the quantity of information that is estimated to be lost. Another approach is to eliminate frames of a movie (usually the first ones, due to high motion, and last ones, due to high radiation damage) as a way to improve information quality, however the signal-to-noise ratio will be affected.

A final step is an attempt to estimate the B-factor (Rosenthal & Henderson, 2003) on the particles, which in turn gives an estimation of the ‘blurring’ nature of the final 3D reconstruction. Structural heterogeneity, the detector’s modulator transfer function (MTF) or the beam-induced motion are some of the factors that blur the high-resolution information and place a limit on the quality of the map. With an estimation of this B-factor (in Å^2), the last step before model building consists on applying a sharpening (or a negative B-factor) to the map, thereby improving the quality of the map.

1.8.9 Model building and fitting

Model building in electron microscopy is similar to the methods used in X-Ray crystallography, and can be done *ab-initio* by giving an aminoacid sequence or by homology modelling with programs such as SWISS-MODEL (Waterhouse et al., 2018), using an existing structure as a template. Model fitting can be done with software such as COOT (Emsley & Cowtan, 2004), furthermore other crystallographic tools used in model building and restrained refinement such as Refmac (Winn et al., 2003) or Phenix (Adams et al., 2010) have been adapted to electron microscopy data.

As for other electron microscopy tools, many have been recently developed. Examples of the tools used in this project include Flex-EM (Joseph et al., 2016), which can fit flexible structures into EM maps and LocScale (Jakobi et al., 2017a), a tool that allows to use previously existing models to further improve the contrast of the maps, thus allowing for better fitting.

1.9 Preamble to the thesis manuscript

The first part of my PhD work consisted of setting up a valid purification strategy for TBTI and CODV antibody-antigen complexes. Furthermore, throughout the project several biophysical and biochemical characterizations, mostly on *apo*-CODV and its complexes, were performed, to assess several factors such as binding to the IL4 and IL13 antigens, stability under different buffers, molecular weights and stoichiometry, and polydispersity in solution. The SPR analysis results of CODV previously published by Sanofi were also confirmed. All of these observations are collected in **Chapter 2**.

Full antibodies seem to be difficult samples for electron microscopy, as they are for x-ray crystallography. Understanding the complexity of these antibodies for cryo-EM has become necessary. This aim has been formulated as **Chapter 3**, where negative-stain electron microscopy (NS-EM) was shown to be a straightforward and useful for preliminary EM investigations of the antibodies under study. **Chapter 3** includes a general protocol for NS-EM sample preparation which produces routinely good-quality micrographs of *apo*-CODV, TBTI and TDT, and of the complexes of CODV with either or both of IL4 and IL13. Subsequently collected datasets were analysed in order to obtain reliable NS-EM 3D reconstructions of these antibodies. This helped to provide several useful insights on their structures and notably highlighted any important structural differences existing between them.

Chapter 4 starts with early attempts at the vitrification of CODV antibodies and the rationale followed towards successfully acquiring optimal grids for cryo-EM. Once this hurdle has been successfully negotiated, image processing of these flexible molecules has been also difficult. Focus was thus shifted to devising an optimal strategy through the use of different programs and scripts for image processing of the CODV datasets in order to achieve the biochemical goals identified at the beginning of the project:

1. At the whole antibody level, description of relative orientations and surface contact between each of the antibody fragments and assessment of putative steric hindrance

that may answer the positional effect paradox described in section **1.3.2** of the **Introduction** (i.e. no positional effect in vitro, but apparent effects in cellulo or in vivo (Steinmetz et al., 2016).

2. To obtain, at least at a Fab level, an intermediate (7-12 Å) resolution structure in near-native conditions that can lead to understanding the architecture of CODV and its implications on structure-based drug design.
3. Higher resolution refinements at the Fab-Ag interface, which may provide crucial information for affinity maturation.
4. Description of the dynamics of CODV Fab arms using Principal Component Analysis (PCA).

Because of the highly challenging image processing of *apo*-CODV and its CODV-IL4 and CODV-IL4/IL13 complexes following the results of **Chapter 4**, this manuscript ends by proposing and demonstrating the use of a locking Fab, called Tralokinumab, that recognises a second binding site of IL13, as a means of acquiring a high-resolution structure of the antibody-antigen binding interface within the full CODV construct. The resulting EM reconstruction of the FabCODV-IL13-Tralokinumab complex was then compared to previous published and non-published structures.

Chapter 2

Purification and characterization of Antibody/Antigen complexes

Antibody complex preparation and purification

-

Assessment of IL4 and IL13 binding to TBTI and CODV complexes

-

Structural stability of CODV and all its complexes

-

Structural analysis of CODV and TC

2. Purification and characterization of antibody/antigen complexes

Preamble

Electron microscopy (EM) is very sensitive to sample quality. Therefore, in order to obtain a high-resolution reconstruction into which a model can be built and refined, the use of biochemical and biophysical techniques to obtain, and characterise, a sample that is as pure and homogeneous as possible is a necessary prerequisite. However, this is not always sufficient. In particular, the presence of additives such as glycerol or certain detergents, which may be critical during purification and characterization steps, may cause a wide array of issues during the cryo-EM grid preparation step (Glaeser, 2018). Furthermore, grid preparation requires optimisation in order to increase the odds of obtaining a well-vitrified grid with optimal particle dispersion.

This chapter describes the purification, the biochemical and biophysical characterisation, and the optimisation of grid preparation, for the targets of this thesis work.

Methods

2.1 Preparation, purification and initial characterisation

CODV-Ig$_{\text{IL4 x IL1 3}}$ (CODV) was purified from Human Embrionic Kidney (HEK 293) cells (Invitrogen) at Sanofi-Aventis Deutschland Gmbh (Frankfurt-am-Main, Germany). TBTI$_{\text{IL4 x IL13}}$ (TBTI) and TDT$_{\text{IL14 x IL13 / TNF}\alpha}$ (TDT) were obtained from Sanofi R&D Biologics (Vitry-sur-Seine, France). Pre-existing preparations of *apo*-CODV and TBTI were in Dulbecco's Phosphate Buffered Saline (DPBS, Thermo Fisher Scientific) at pH 7.2, while TDT was in Tris Buffered Saline (TBS) buffer. Hexa-histidine-tagged IL4 and untagged IL13 in Phosphate Buffered Saline (PBS, Merck) at pH 7.4 were acquired from Evotec (Lyon, France). Antibodies were stored at 5°C and ligand aliquots were stored at -80°C.

New preparations of *apo*-CODV were stored in His buffer, while the CODV-IL4, CODV-IL13 and CODV IL4/IL13 complexes were all in Sanofi TBS (STBS). Tralokinumab (alternative-site IL13-binding Fab) samples were in TBS. The composition and pH values of the buffers most commonly used throughout the project are shown in **Table 2.1.**

Buffer	DPBS	SB	STBS	TBS	BB	EB	His
Tris		50 mM	50 mM	20 mM			
Phosphate	4.3 mM				20 mM	20 mM	
Histidine							10 mM
NaCl	155.2 mM	95.3 mM	50 mM	50 mM	500 mM	500 mM	150 mM
KCl		2.7 mM					
Imidazole					20 mM	500 mM	
pH	7.2	8.0	8.0	8.0	7.4	7.4	6.0

Table 2.1. The composition of storage and purification buffers most used throughout this work.

2.2 Complex preparation and purification

TBTI-IL4, TBTI-IL13, CODV-IL4, CODV-IL13 and CODV-IL4/IL13 were prepared by mixing antibody and antigen with 4-fold molar excess of IL4 or IL13. The samples were centrifuged at 12100 x g for 5 minutes before injection onto chromatography columns to remove possible aggregates.

TBTI-IL4 and TBTI-IL13 were purified using a Superdex S200 5/150 Increase GL gel filtration column (GE Healthcare) equilibrated with DPBS buffer at 4°C on an ÄKTA Micro chromatography system (GE Life Sciences). Fractions containing the pure complex were then further separated from non-bound antibodies using a HisTrap FF 1 ml nickel affinity chromatography column (Cytiva Life Sciences). Here, the column was equilibrated with BB binding buffer and washed with EB elution buffer. Complexes were then eluted by gradually increasing imidazole concentration from 20 to 500 mM. Fractions containing the complexes were pooled, then buffer exchanged to Gibco DPBS (pH 7.4) with a PD-10 desalting column (GE Healthcare). Finally, the complex was concentrated to 0.33 mg/ml using a 30000 Da MWCO concentrator (Merck Millipore) and stored at 5°C for later use.

Initial purification of CODV-IL4 was performed on a Nexera X2 analytical HPLC system (Shimadzu) on a Superdex 200 Increase 3.2/300 gel filtration column equilibrated with Gibco DPBS buffer. Central peak fractions were collected and concentrated to around ~0.24 mg/ml using a 30000 Da MWCO microconcentrator (Amicon). In an optimized protocol later used, CODV-IL4, CODV-IL13 and CODV-IL4/IL13 were purified using the same column equilibrated with SB on an ÄKTA Pure at 4°C. The samples were collected with an ÄKTA micro module (GE Healthcare) and did not require concentration steps, as they eluted at concentrations in the range of 0.25 to 0.30 mg/ml, suitable for cryo-grid preparation. The purified complexes were stored at 5°C.

For the purification of the CODV-IL13-Tralokinumab triple complex (TC) and the CODV-IL4/IL13-tralokinumab quadruple complex (QC), a single high-resolution size exclusion chromatography step was performed, using a Superose 6 3.2/300 increase column equilibrated with SB. The flow setting used was very slow (0.04 ml/min) to allow for the correct separation of peaks. A high initial concentration was used (1 mg/ml of CODV) to avoid concentration steps that could lead to partial loss of complex or aggregation. In TC, IL13 was added first in 4-fold molar excess and after 15 minutes Tralokinumab was added, also in 4-fold molar excess. For QC, IL4 was added last, 15 minutes after Tralokinumab, in 4-fold molar excess. Only the centre of the peak was collected for storage.

Throughout all purification procedures, eluted fractions were analysed using denaturing 15% sodium dodecyl sulphate polyacrylamide gel electrophoresis (SDS-PAGE). Protein concentration was checked using a Nanodrop ND-1000 spectrophotometer (Thermo Fisher Scientific) in combination with the theoretical absorption coefficients calculated using the PROTPARAM online tool provided by ExPASy (Gasteiger et al., 2005).

To assess aggregation in TBTI-IL4 purification fraction peaks, dynamic light scattering (Berne & Pecora, 2000) (DLS) was performed on a Zetasizer (Malvern) machine. Three 50 µl fractions were added to low-volume quartz cuvettes for analysis.

For TBTI-IL4, complex formation was verified by Western blotting using a FITC rabbit polyclonal anti His_6-tag antibody (Abcam) targeting IL4 with signal photodetection performed using a Typhoon fluorescence scanner (Amersham Biosciences). Here, a 5% native-PAGE gel was run to evaluate binding at a full-antibody level and the blot was transferred from the gel onto a PVDF (Polyvinylidenfluorid) membrane, hydrated for 15 minutes in transfer buffer (for 1 L: 1 g SDS, 3.03 g Tris, 14.41 g glycine, 10% ethanol). A sandwich was built (from negative to positive electrode), containing 4 layers of Whatman filter paper, the gel, the PVDF sheet and 4 more layers of Whatman paper. The samples were blotted for 45 minutes at 100 V at room temperature. The membrane was put into a Falcon tube saturated in 2.5% milk powder, 0.1% tween-20 in 1x PBS to reduce unspecific binding of the antibody added in the next step. After the initial wash, the membrane was stained overnight at 4°C with anti-His-tag antibody in a

Falcon tube rotator. After overnight incubation, the antibody solution was removed, and three wash steps of 20 minutes were performed before fluorescence analysis of the membrane on a Typhoon scanner.

For CODV-IL4, to assess whether the IL4 antigen was not only present but was actually bound to the antibody in the SEC fractions purified, a His_6-Tag based pull-down experiment was performed in a 0.2 ml bed volume Ni-NTA spin column (QIAGEN). Two experiments were performed in parallel, a 50 µl CODV-IL4 run and a negative control with 50 µl *apo*-CODV. Here, the columns, placed inside 2 ml Eppendorf tubes, were first equilibrated with 600 µl NPI-20 buffer (50 mM sodium phosphate, 300 mM NaCl, 20 mM imidazole, pH 8). After centrifugation for 2 minutes at 890 x g, the flow-through was discarded and the samples were added into their corresponding tube. Tubes were then centrifuged at 270 x g for 5 minutes and the flow-throughs collected. Columns were then washed twice with 100 µl NPI-20 and each time, after centrifugation at 890 x g for 2 minutes, the flow-through was also collected. Elution was performed with identical methodology using an NPI-500 buffer (50 mM sodium phosphate, 300 mM NaCl, 500 mM imidazole, pH 8). The five flow-throughs of each run were examined with a 15% SDS-PAGE. Samples containing pure CODV-IL4 were dialyzed overnight at 4°C against STBS buffer.

Finally, all samples were subject to analysis by mass photometry (Sonn-Segev et al., 2020), a new technique for the rapid estimation of the proportions of all proteins contained in samples of microliter-range volumes and with sub-micromolar concentrations. Here, 15 µL volumes of 100 nM dilutions of CODV, CODV-IL4, CODV-IL13, CODV-IL4/IL13 and TC were analysed using a One^{MP} mass photometer (Refeyn Ltd, Oxford, UK), previously calibrated with SB buffer to find the focal point and estimate background noise. After the measurements, image processing was performed as described in Sonn-Segev et al. (Sonn-Segev et al., 2020) using the DiscoverMP (Refeyn Ltd) software package and graphs of intensity vs molecular weight plotted.

2.3 Analysis of binding affinities in CODV-antigen complexes

Antigen binding and affinity parameters for CODV-IL4 and CODV-IL13 were measured by Surface Plasmon Resonance (SPR) in a Biacore 8K SPR system (GE Healthcare). A dextran CM5 sensor chip was used for the protocol, which immobilized anti-human IgG-Fc overnight via amine-coupling. Flow-cell 1 (FC1) was used as a reference while FC2 was utilized for capturing CODV and the ligand. The buffer used for the runs was STBS with the addition of Tween P20 0.01% to lower the surface tension and reduce non-specific binding.

For the evaluation of the dissociation constants (K_D) of IL4 and IL13 binding to CODV, several runs were performed with serial dilutions of the antigens (**Table 2.2**). Following the determination of the binding parameters, final SPR runs were carried out with concentrations of 1.5 µg/ml (7.6 nM) CODV, 3 nM IL4 and 25 nM IL13.

Dilution	**1**	**2**	**3**	**4**	**5**	**6**	**7**	**8**
IL4 (nM)	$3 \cdot 10^{-4}$	0.001	0.006	0.032	0.16	0.8	4	20
IL13 (nM)	$3 \cdot 10^{-3}$	0.013	0.064	0.32	1.6	8	40	200

Table 2.2: Concentrations of IL4 and IL13 used against 1.5 µg/ml of CODV in each of the binding runs of SPR to determine the KD of ligand binding.

2.4 Analysis of buffer stability for CODV and it complexes with IL-4 and IL-13

In order to identify the buffers in which CODV, CODV-IL4 and CODV-IL13 are most stable, their melting temperatures (T_m) were measured in a wide array of buffers using nano-DSF (Differential Scanning Fluorimetry) carried out in a Prometheus NT.48 (NanoTemper) device. For this, samples were diluted to a final concentration of around 15 µg/ml (for CODV) and 7 µg/ml (for complexes), which was observed to be sufficient for an optimal signal after a first screening step in their initial buffers. Measurements were then performed with 100% light intensity and a temperature ramp from 20 to 90°C (1°C/minute increase). The 10 µl capillaries were filled with a mixture of 0.5 µl sample, 0.5 µl buffer to be tested and 9 µl of 50mM NaCl to provide the ionic strength. This way, the ratio of target buffer to original buffer was 20:1 (50 mM new buffer, 2.5 mM old buffer). The list of buffers tested is shown in **Table 2.3.**

Buffer (1 M)	pH
AMPD	9.3
Glycine	9.2
Bis Tris propane	8.8
Tris Control	8.2
Bicine	8.1
Tricine	8
Tris HCl	7.5
HEPES	7.4
MOPS	7.1
Bis Tris propane	7
HEPES Na	6.9
ADA	6.4
Bis Tris	6.3
MES	5.9
Na cacodylate	5.8
Succinic acid	5.4
DL-Malic acid	5.3
Na acetate	4.3
Na citrate	4.2
Citric acid	4.1

Table 2.3: List of stock buffers and their pH values tested by nano-DSF for assessment of thermostability of CODV and its complexes.

2.5 BioSAXS of CODV

Small angle X-Ray scattering (SAXS) is a technique utilized to analyse molecular shape, and in many cases elucidate tertiary or quaternary structure in solution (Koch et al., 2003). It can also provide additional information about the sample being studied, such as indications of the flexibility of the molecule and the number of domains it contains (Hura et al., 2009). Moreover, SAXS analysis of biological macromolecules (BioSAXS) can yield low-resolution envelopes of the solution structure of the molecule under study. These can sometimes be used as a starting reference for electron microscopy image processing (Franke et al., 2017).

With the help of Dr. Mark Tully at the ESRF BioSAXS beamline at BM29 (Pernot et al., 2013), SAXS measurements from solutions of CODV and TC were obtained using X-rays of 12.5 keV energy (λ= 0.99 Å) and a Pilatus 1M pixel array detector (Dectris). Data analysis was carried out using Scatter (Förster et al., 2010) and low-resolution envelopes of the solution structures obtained using the ATSAS (Franke et al., 2017) online tool from EMBL Hamburg. Before SAXS experiments, in order to normalize buffer conditions 200 µl of *apo*-CODV solution (see above) was dialyzed for 48h at 4°C against 1L of DPBS buffer. Four concentrations of antibody were used for this experiment: 1.14, 1, 0.75 and 0.5 mg/ml.

For TC, 100 µl of freshly purified antibody was used at a concentration of 1 mg/ml in the SEC-SAXS variant of the technique (Watanabe & Inoko, 2009), where an HPLC step is run just prior to the sample scattering in the beam. The column and flow rate used were identical to the those used in the purification of TC (Superose 6 Increase 3.2/300 at 0.04 ml/min), while the chromatography system was a Nexera X2 HPLC (Shimadzu) and the buffer used was SB with the addition of 1 mM tris (2-carboxyethyl) phosphine (TCEP) to protect the sample from radiation damage (Jeffries et al., 2015).

Results

2.6 Complex production and purification

2.6.1 TBTI-IL4 and TBTI-IL13

As CODV was not available at the start of the project, TBTI was used in IL4 and IL13 binding experiments in order to identify putative purification and validation steps that would yield CODV-antigen complexes of sufficient purity and concentration for structural studies.

Because samples for cryo-EM use small volumes, and to overcome any undesirable concentration effects, SEC runs were performed on an ÄKTA Micro system equipped with a Superdex S200 15/150 at 4°C. TBTI was mixed with IL4 in a 1:4 molar ratio in a 50µl reaction volume (50 µM TBTI, 200 µM IL4). The chromatogram (**Figure 2.1A**) showed three main peaks, two of them early in the elution volume, with the third (C10) appearing towards the end of the purification and attributed to excess IL4. Dynamic light scattering (DLS) analysis of fractions corresponding to the two peaks (B3 and B8) and the intervening shoulder (B6) showed a clear difference in size and volume of the species contained in B6 and B8 compared with that for B3 (**Figure 2.1B**), suggesting two states, possible aggregation and a peak containing the non-aggregated complex.

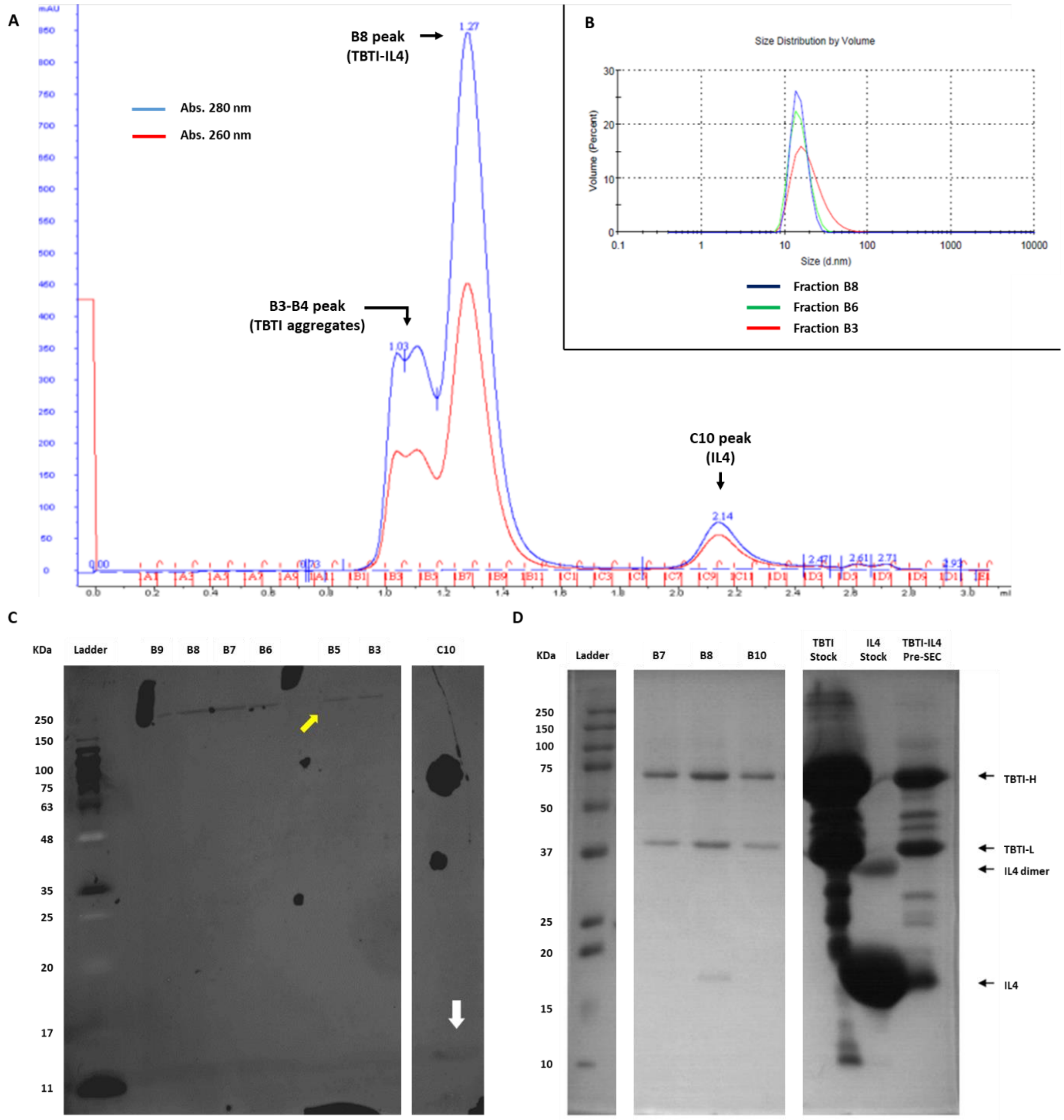

Figure 2.1: Purification and validation process of TBTI-IL4. (A) SEC with Superdex S200 5/150 after complex preparation, 3 main peaks are observed. **(B)** DLS of fractions B3 (first peak), B5 (beginning of the main peak) and B8 (centre of the main peak). B3 (red) showed a broad size and volume spectra, characteristic of aggregates, different from a sharp peak in B6/B8 (green/blue). **(C)** Anti-His$_6$ western blot analysis of the fractions and of the fraction C10 (excess IL4) showed bands in all of them, intense in the main peak and faint (yellow arrow) in the aggregated B3/B5 fractions and C10 (white). **(D)** SDS-PAGE 15% of fractions after affinity chromatography, where IL4 was faint but present in the peak centre.

To confirm this a Western Blot analysis (**Figure 2.1C**) was performed using an anti-His$_6$ antibody as a marker to verify the presence of the His$_6$-tagged IL4 in the complex. A stronger signal in Western Blot lanes corresponding to the B7-B8 SEC fractions (main peak) confirmed that indeed the TBTI-IL4 complex was mainly or solely present in these fractions, while in other fractions the signal was diluted, as was the case of aggregates (yellow arrow) and the low-signal peak of excess IL4 (white arrow).

The fractions corresponding to the main peak were thus pooled and further purified by affinity chromatography as described in **2.1**. Only a single peak, at around 75% total imidazole concentration (375 mM) was detected in the elution step (**Figure 7.1** in **Annex**). An array of fractions was analysed on a 15% SDS-PAGE along with controls and presence of the complex was confirmed in a number of fractions, with that corresponding to the peak centre showing the highest concentration (**Figure 2.1D**). This fraction was then buffer exchanged to DPBS using a PD-10 column to remove the imidazole. The final sample concentration was determined to be 0.33 mg/ml by absorbance measurement at 280 nm.

For the TBTI-IL13 complex, the purification order was changed in order to skip the buffer exchange step (*i.e.*, affinity chromatography was performed first and SEC second). The yield obtained with this protocol was very low, and was attributed to the harmful concentration step with the imidazole from the affinity chromatography step.

2.6.2 CODV-IL4, CODV-IL13 and CODV-IL4/IL13

For CODV-IL4, different approaches were tried in order to improve the yield of the complex as well as to skip harsh steps such as concentrations, used for TBTI-IL4 and TBTI-IL13 (see above), that may lead to aggregation or denaturation of the proteins.

Complex preparation was performed using a 1:6 molar ratio incubated for 10 minutes to ensure complete binding. The shift in the elution peak of CODV-IL4 (**Figure 2.2A**) compared to those seen for IL4 and *apo*-CODV, run as separate controls, clearly indicated complex formation, as confirmed by SDS-PAGE analysis (**Figure 2.2B**). The fraction corresponding to centre of the peak was collected directly at a concentration of 0.3 mg/ml, which was sufficient for negative-stain and cryo-EM experiments and thus did not require concentration steps. CODV-IL13 and CODV-IL4/IL13 were purified in a similar manner (**Figure 2.2**).

As can be seen in **Figure 2.2B**, SDS-PAGE analysis of the peak centre fractions showed clear bands corresponding to the heavy and light chains of CODV and to the antigens themselves. To further confirm complex formation, MW analysis using mass photometry was also performed (see **2.7.2**).

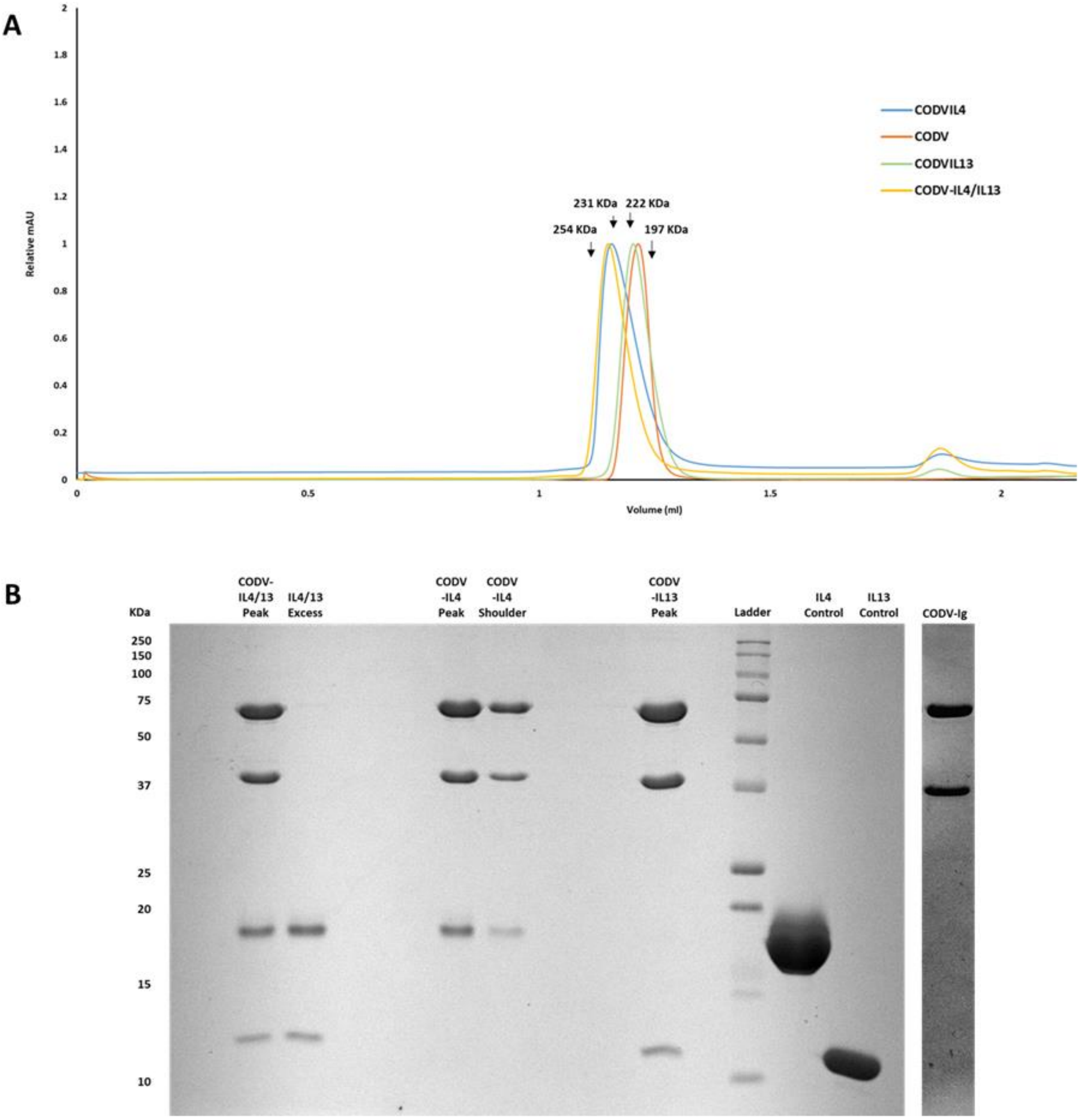

Figure 2.2: Purification of CODV-antigen complexes. (A): Size exclusion chromatography elution peaks for apo-CODV (orange), CODV-IL4 (blue), CODV-IL13 (green) and CODV-IL4/13 (yellow), with their theoretical MWs shown. All elution profiles showed a single main peak corresponding to the complex with a small peak, appearing much later corresponding to excess ligand**. (B)** SDS-PAGE analysis of purified CODV-antigen complexes and, as positive controls, of IL4 and IL3. SDS-PAGE analysis of purified CODV was run separately (rightmost panel).

2.6.3 CODV-IL13-Tralokinumab (TC) and CODV-IL4-IL13-Tralokinumab (QC)

For the preparation and purification of the CODV-IL13-Tralokinumab complex a similar approach to that outlined in **2.2** was used. IL13 was first added in a 4-fold molar excess to CODV and incubated for 15 minutes at 4°C. Tralokinumab, also at a 4-fold molar excess, was then added to the sample tube. The solution was incubated for a further 15 minutes. The sample was then centrifuged at 12000 x g for 5 minutes and loaded onto a Superose 6 Increase 3.2/300 column.

The resulting chromatogram (**Figure 2.3A**, in grey) was compared to a CODV-IL13 control run in the same SB buffer. This showed a large shift in the elution peak indicating CODV-IL13-Tralokinumab complex formation which was confirmed by SDS-PAGE analysis. The fractions containing the ternary complex were then pooled and concentrated to 0.45 mg/ml. In later SEC purifications (**Figure 2.3A**), only fractions close to the elution peak centre were analysed in SDS-PAGE and pooled (**Figure 2.3B**). For SEC-SAXS experiments, the sample was concentrated at low speed (8000 rpm) to 1 mg/ml.

The CODV-IL14/IL13-Tralokinumab quadruple complex (QC) was prepared in a similar manner to TC with the exception that IL-4, in a 4-fold molar excess, was added to the solution of CODV-IL13-Tralokinumab (see above) and the sample incubated for 15 minutes. Purification followed the same protocol as for TC (**Figure 2.3A**), with SDS-PAGE analysis of the main elution peak (**Figure 2.3B**) confirming the presence of both ligands.

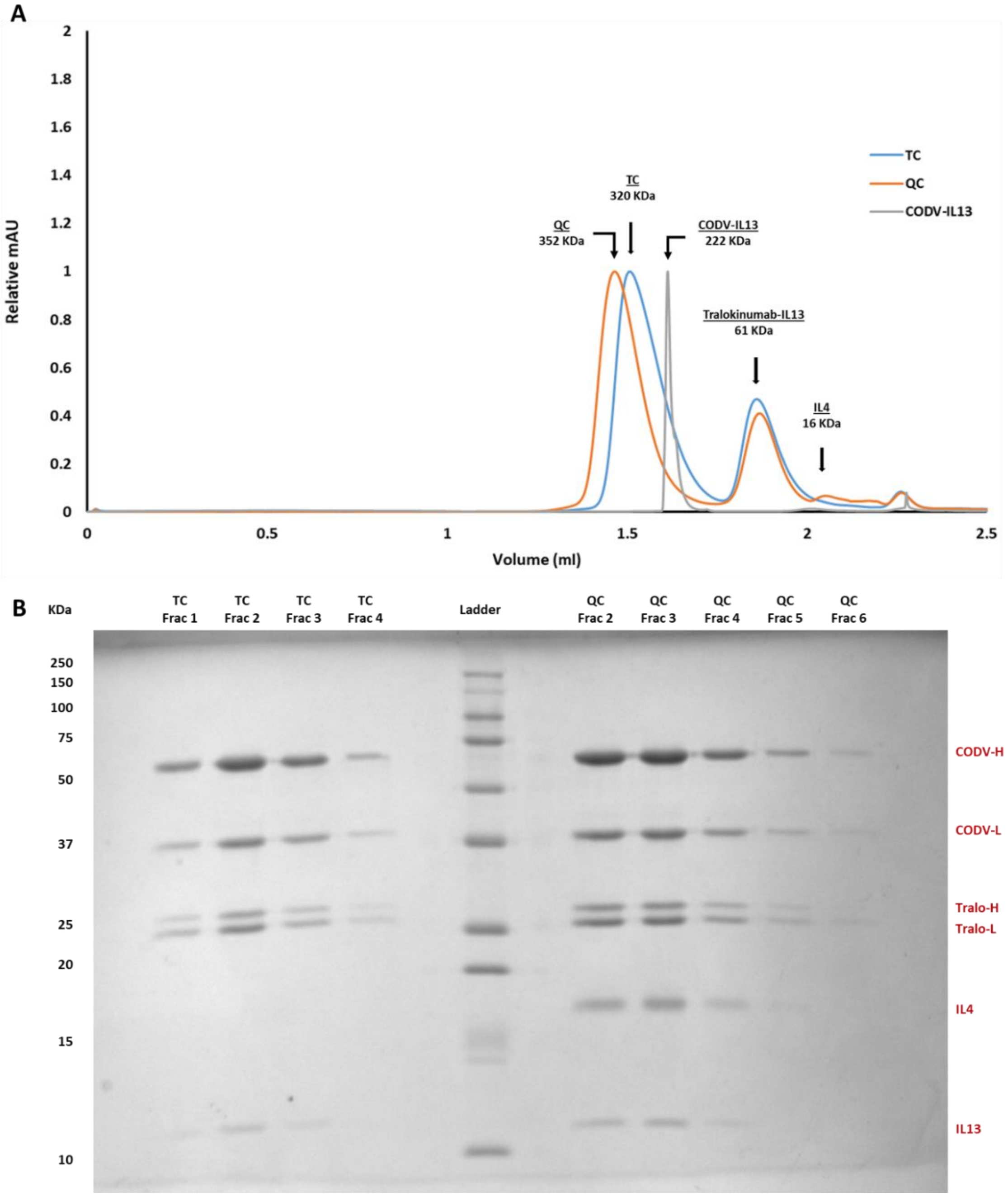

Figure 2.3: Purification and characterization of the CODV-IL13-Tralokinumab and CODV-IL4/IL13-Tralokinumab (QC) complexes. (A) Superose 6 3.2/300 Increase high-resolution SEC elution peak profiles for CODV-IL13-Tralokinumab (blue) and CODV-IL4/IL13-Tralokinumab (orange) the controls CODV (green) and Tralokinumab-IL13 (blue). **(B)** 15% SDS-PAGE of the two runs, where fraction 2 of each run corresponds to the peak of the fully bound triple complex and quadruple complex.

2.7 Assessment of the binding of IL4 and IL13 to CODV

2.7.1 Surface Plasmon Resonance Measurements

Although previous studies had shown that both IL4 and IL-13 bind to CODV (Steinmetz et al., 2016), exact binding parameters had not been determined. To obtain detailed information concerning these, Surface Plasmon Resonance (SPR) assays were performed. Here, two protocols were used. The first comprised the use of serial dilutions of the IL4 and IL13 antigens with the aim of calculating the equilibrium dissociation constants (K_D) for CODV-IL4 and CODV-IL13 in PBS P+ buffer pH 7.4 (0.2 M phosphate buffer with 27 mM KCl, 1.37 M NaCl and 0.5% Tween P20).

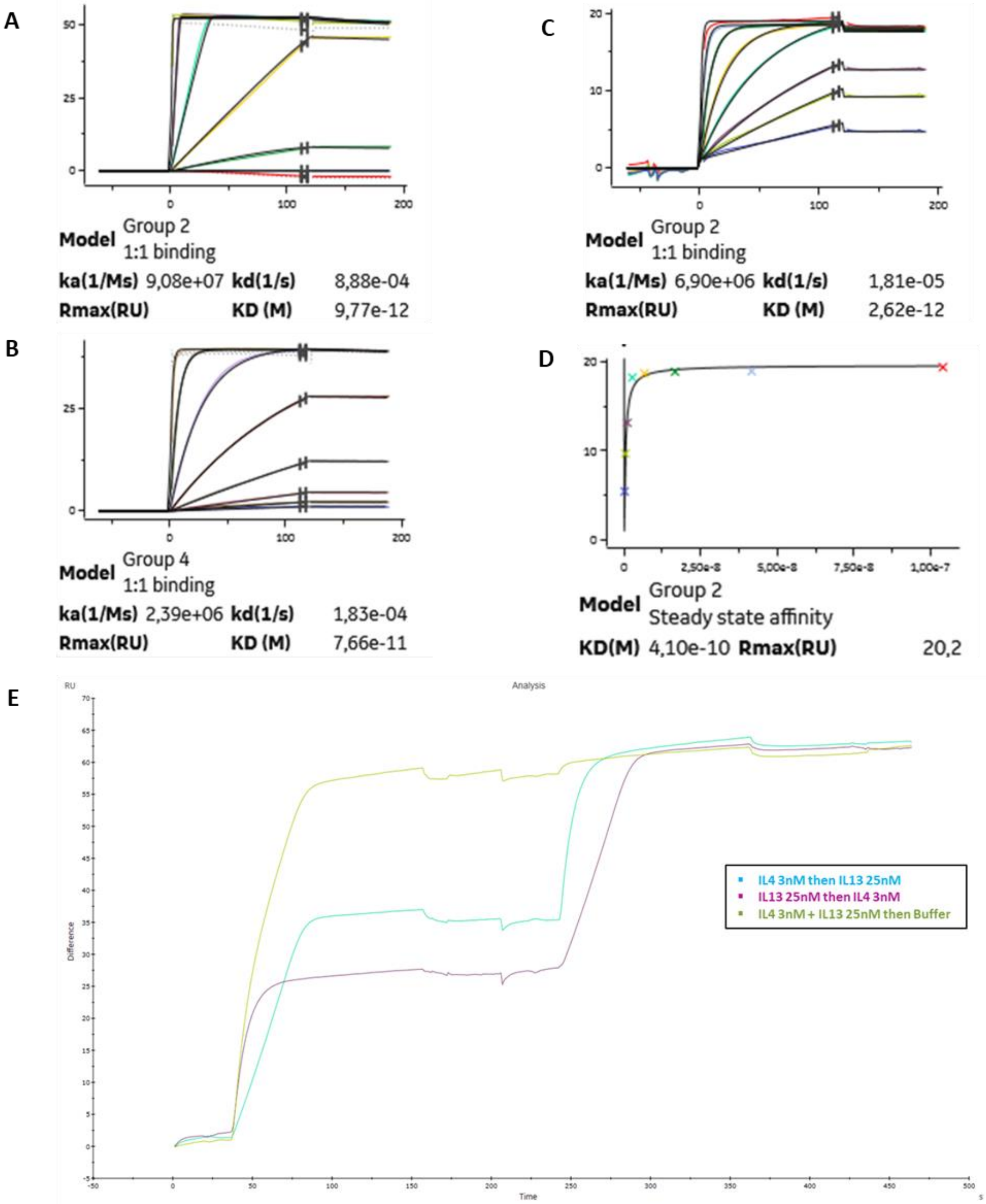

Figure 2.4: Binding assays of CODV-antigen complexes as measured by SPR. Binding curves at different concentrations of IL4 **(A)** and IL13 **(B)** evidence high affinity typical of mature antibody-antigen interactions. IL4 has a higher affinity than IL13. This affinity is also in the picomolar range for IL13 when IL4 is already bound, measured by **(C)** 1:1 binding or **(D)** steady-state models. **(E)** The signal reaches its maximum plateau no matter the order of the antigens added. The curve for IL4 added first is in blue, that for IL13 added first in purple, the curve when both IL4 and IL13 are added simultaneously is shown in green.

Prior knowledge was used to estimate the range of concentrations of ligand to use (see **Table 2.2**), The sensograms obtained (**Figures 2.4A, B**) yielded K_D values confirming very high affinity in both cases: 76 pM for CODV-IL13, 9 pM, for CODV-IL4 using a 1:1 stoichiometry model. Using a 1:2 model did not change values significantly, so we kept the 1:1 results.

A second, similar, binding experiment was performed to confirm the above K_Ds. This time, each antigen was used with standalone concentrations of 3 nM for IL4, and 25 nM for IL13, to ensure saturation. Here, once the signals reached a plateau, the flow of antigen was stopped and TBS was flowed through the cell for 5 hours in order to measure antigen dissociation rates (**Table 2.4, Figure 7.2** in **Annex**).

Once the binding characteristics of single antigens had been determined, an assessment of the 'order effect' of IL4 and IL13 binding to CODV was performed. This experiment reproduced the methods published in (Steinmetz et al., 2016) with 3 nM IL4 and 25 nM IL13 and confirmed that the binding of either of the antigens first does not significantly obstruct the binding of the other, nor does the binding of both antigens at the same time (**Figure 2.4E, Table 2.4**). In these experiments, a minor difference between adding IL4 or IL13 second is that binding of IL4 following that of IL13 produces a non-exponential curve towards the plateau (**Figure 4E**). This is typically indicative of a mass transport phenomenon or "titration regime"(Jarmoskaite et al., 2020), which can happen when the analyte is added in a concentration more than 100 times the K_D. While this does not impact on the conclusion made above (*i.e.* that pre-binding of IL13 to CODV does not affect the binding of IL4), the change in shape means that at the concentration used K_D measurements become unreliable and are thus not shown here.

Binding parameters	**IL4 alone (normal method)**	**IL13 alone (normal method)**	**IL4 (stop-flow)**	**IL13 (stop-flow)**	**IL13 with IL4 bound (1:1 binding)**	**IL13 with IL4 bound (steady-state)**
k_{on} ($M^{-1}s^{-1}$)	9.8×10^{7}	2.39×10^{6}	1.01×10^{7}	4.32×10^{6}	6.9×10^{6}	9.8×10^{7}
k_{off} (s^{-1})	8.88×10^{-4}	1.83×10^{-4}	1.89×10^{-5}	6.29×10^{-5}	1.81×10^{-5}	9.21×10^{-6}
K_D (M)	9.77×10^{-12}	7.66×10^{-11}	1.87×10^{-12}	1.45×10^{-11}	2.62×10^{-12}	1.22×10^{-12}

Table 2.4: Rates of association/dissociation calculated for all ligands bound to CODV, using different methods.

The SPR sensorgrams obtained for IL13 binding following that of IL4 are shown in **Figures 2.4C** (IL13 K_D with IL4 pre-bound, 1:1 binding model) **and 2.4D** (IL13 K_D with IL4 pre-bound, steady-state model). The K_D's calculated were similar in both cases (**Table 2.4**).

As will be seen later in the manuscript, and despite the observations during SEC purification and SPR experiments, positions for antigen binding in CODV-IL4, CODV-IL13 and CODV-IL4/IL13 complexes could not be clearly identified in NS-EM. Mass photometry and a Ni-NTA pulldown experiment were therefore also used to verify that the IL4 and/or IL13 antigens remained bound to CODV in solution prior to EM experiments.

2.7.2 Mass photometry

In all Mass Photometry experiments, other than a residual noise peak in the 70-90 KDa molecular weight range, which can be identified when the peak is mirrored on the negative side of the graph, only a single peak was observed (**Figure 2.5**). In all cases, and within the error of the technique (Young et al., 2018), this corresponded to the expected molecular weight. Moreover, for CODV-IL4 and CODV-IL4/L13 the technique clearly suggested a 1:2 or 1:2:2 stoichiometry, meaning each of the antibodies has antigens bound to each of the Fabs.

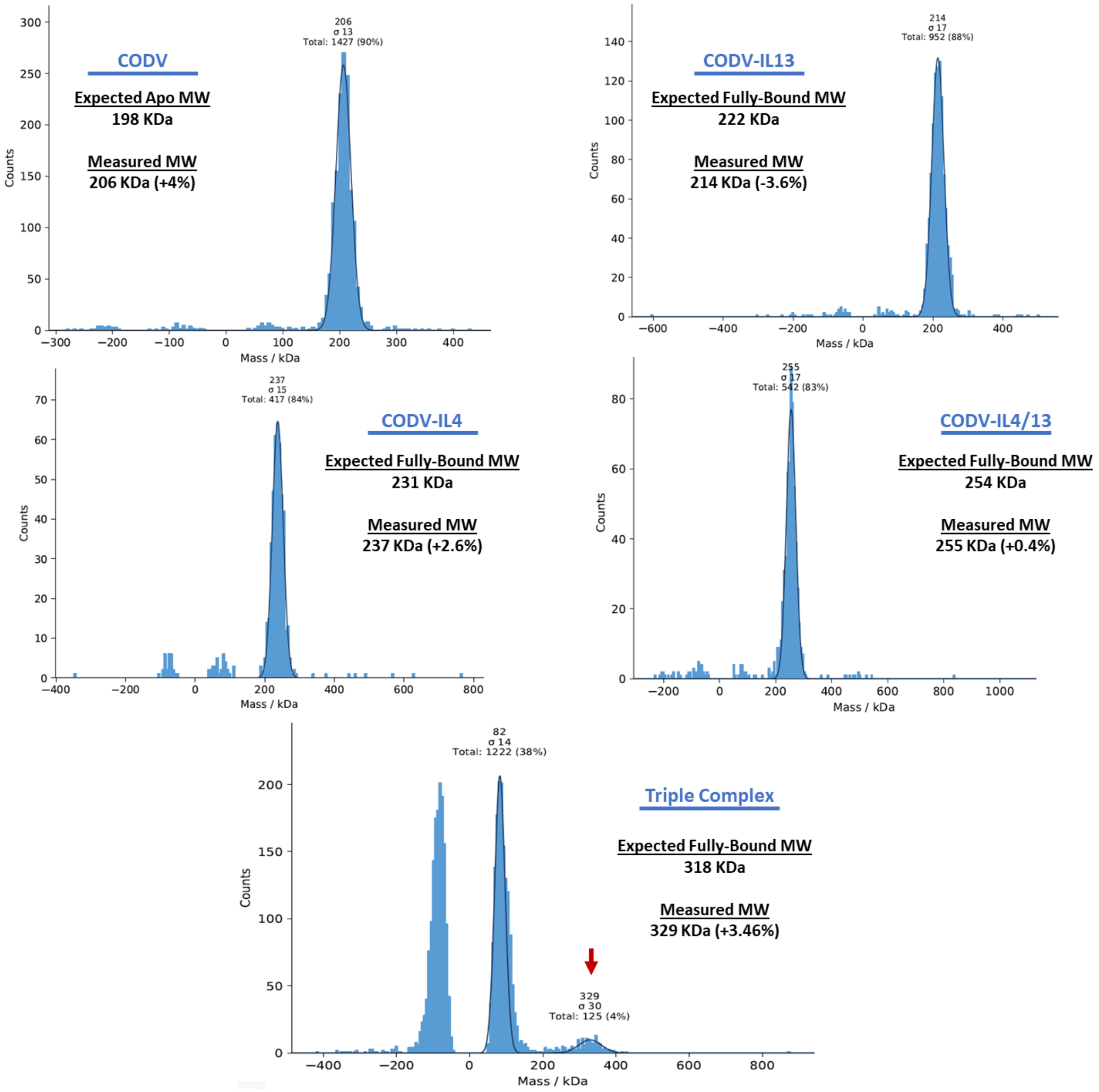

Figure 2.5: Mass photometry of CODV-Ig and its complexes. The main peaks in all experiments confirm a 1:2 stoichiometry binding of ligands to the antibodies within a maximum expected 5% error. CODV-IL13 showed an experimental MW that was between a single- and double-bound complexes. It was thus concluded that complexes with both 1:1 and 1:2 stoichiometries are present. For the triple complex (bottom), a peak at around 329 KDa can be observed, which approximately coincides with a 1:2:2 stoichiometry. There is a large peak at 82 KDa that can be attributed to noise, since its signal in the negative side of the graph is mirrored.

For the CODV-IL13 complex the binding stoichiometry was less conclusive, with the experimentally obtained MW of 214 KDa falling between 1:1 (209 kDa) and 1:2 (221 kDa). Following a discussion with the developers of the technique, it was concluded that due to the resolution limit of the technique, should there be two very close peaks on a sample, there is a possibility that the observed peak corresponds to the average of both signals. As a result, it was concluded that species with both 1:1 and 1:2 stoichiometries were present.

Overall, these results confirm the existence of a 1:2 stoichiometry for all the complexes but indicate that for CODV-IL13 a 1:1 stoichiometry is also present. They also reinforce the results of the SPR experiments performed, which show no positional effect when binding different antigens onto the same Fab. The SPR calculations were attempted using both 1:1 and 1:2 models, but no significant difference was observed and did not change the interpretation.

2.7.3 CODV-IL4 Ni-NTA pull-down experiment

To further confirm that CODV and IL4 were strongly bound to each other a Ni-NTA was performed, taking advantage of the His$_6$ tag present at the N-terminus of the IL4 construct used in this work. SDS-PAGE analysis (**Figure 2.6**) of both the binding and control runs evidenced that CODV was indeed bound to IL4 within the sample tube, as the antibody did not elute during the washing steps without imidazole and only appeared in the steps where high concentrations of imidazole were used. The control *apo*-CODV, on the other hand, eluted at all steps irrespective of the usage of imidazole.

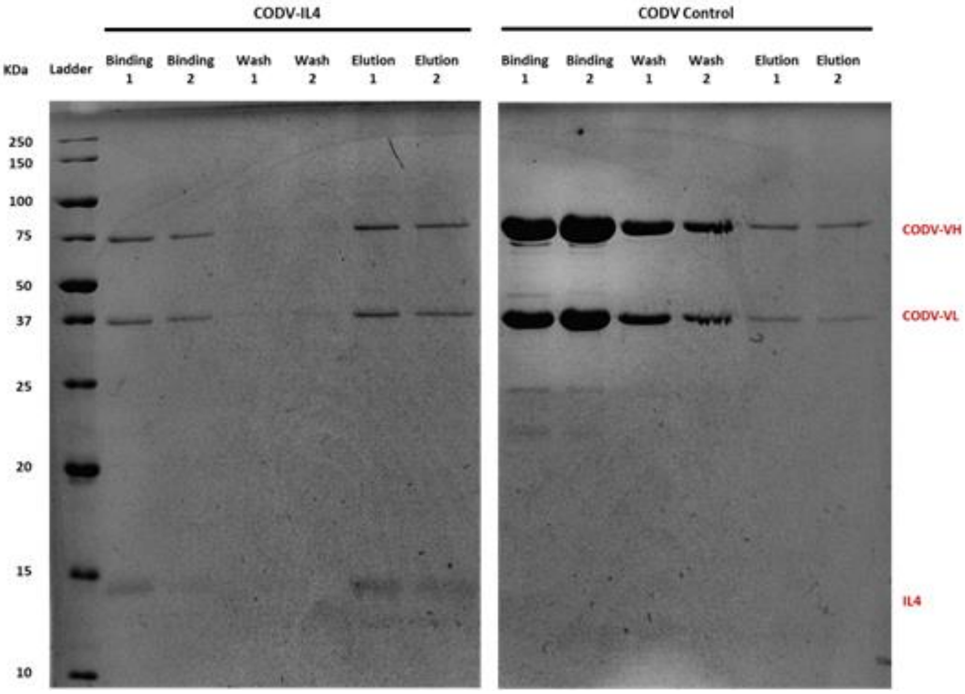

Figure 2.6: SDS-PAGE analysis of the CODV-IL4 Ni-NTA pulldown experiment. Both excess CODV and CODV-IL4 eluted during the binding step, but excess free CODV kept eluting in all subsequent steps while CODV-IL4 stayed specifically bound to the Ni-NTA resin during the washing steps. Only when high concentrations of imidazole were applied during the elution step did the bound complex elute.

2.8 Structural stability of *apo*-CODV and its complexes

The results of the experiments described above clearly suggest that antigen binding to CODV is robust and does not cause significant sample aggregation. Aggregation can, however, be caused by vitrification during cryo-EM grid preparation. In order to try to reduce this possibility, measurements, in various different buffers, of the melting temperatures of (T_m) of *apo*-CODV and its complexes with antigens were carried out. Here, it was hypothesized that a buffer that could provide a constant increase of T_m across *apo*-CODV and its antigen complexes could help diminish potential aggregation caused by harsh freezing conditions. Furthermore, a stabilizing buffer could also potentially aid in restricting the heterogeneity during EM data collection. A total of 20 buffers (**Table 2.3**) were tested for *apo*-CODV, CODV-IL4, CODV-IL13 and CODV-IL4/IL13**.**

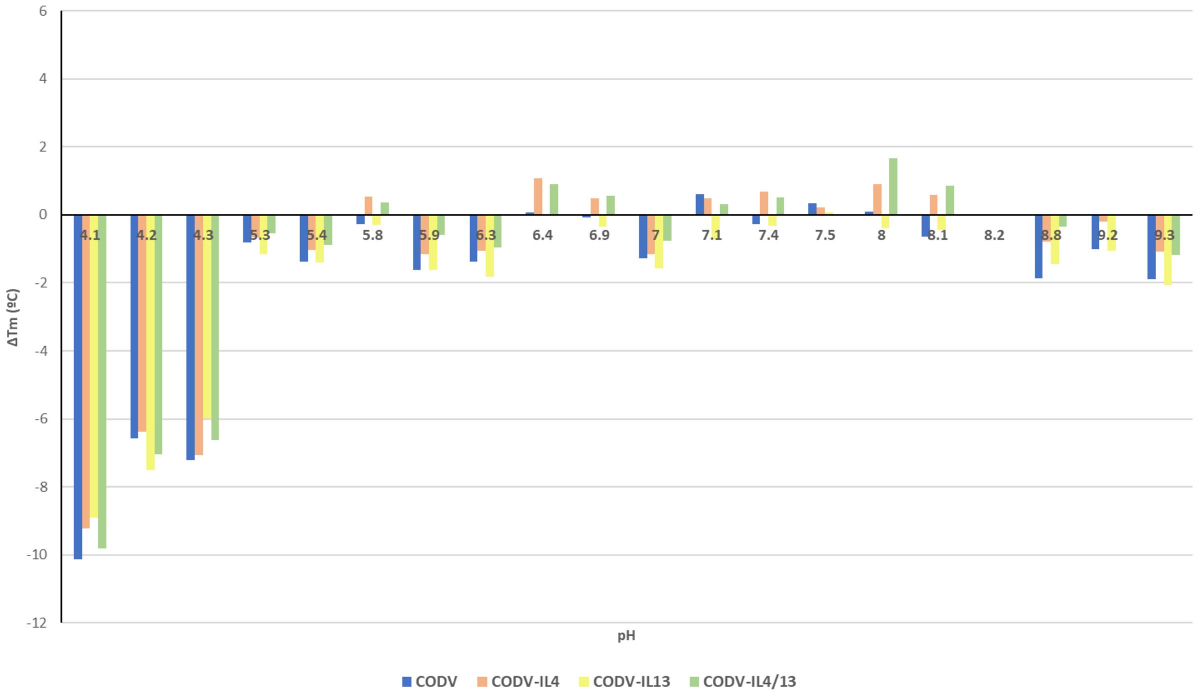

Figure 2.7: Thermostability of CODV and its complexes in different buffers. A total of 20 buffers were tested in the pH range of 4.1 to 9.3. Free CODV (blue) shows the biggest Tm changes in most cases compared to a TBS pH 8.2 control; however, all samples follow a similar pattern. The most pronounced drops in stability occur in buffers under pH 5.

The results obtained by nano-DSF (**Figure 2.7**) evidence a pattern of constant thermostability in the pH ranges between 6.4 and 8.2. However, buffer conditions under pH 5 result in a strong destabilizing effect. Moreover, in the different buffers analysed for each sample, no buffer-linked aggregation could be observed (**Figure 2.8**) except for those that produced drastically lower T_m values. *Apo*-CODV and its complexes thus seem to exhibit resistance to aggregation in solution over a large range of pH values, and do not seem to aggregate at cold or room temperature.

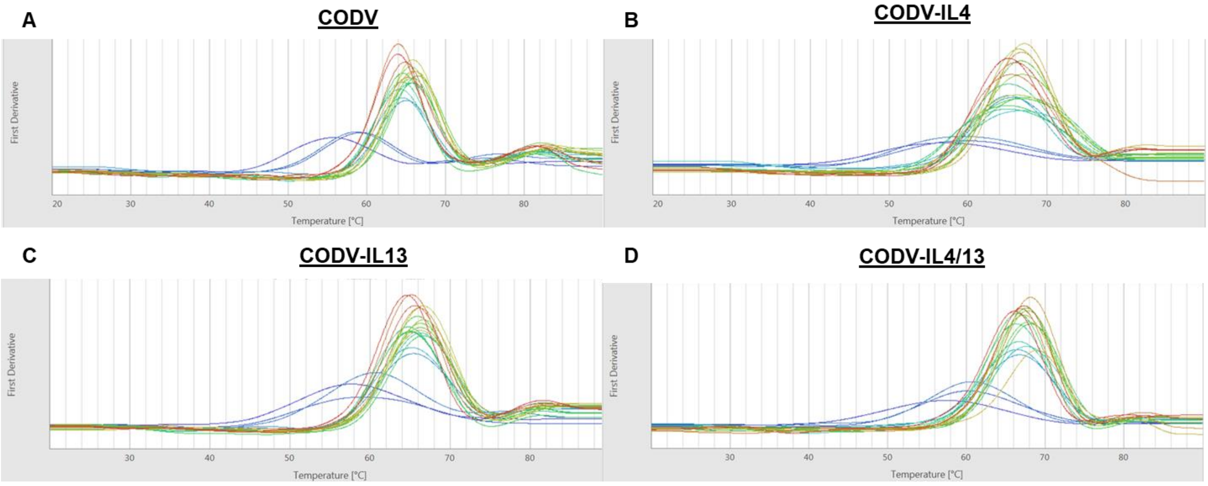

Figure 2.8: Melting temperatures of CODV, and its complexes with antigens, as analysed by nanoDSF. CODV **(A),** CODV-IL4 **(B),** CODV-IL13 **(C)** and CODV-IL4/IL13 **(D).** All plots show the first derivative of the melting curves obtained and show a well-fined Tm in all cases. Traces for the three buffers under pH5 (citric acid (pH 4.1), sodium citrate (pH 4.2) and sodium acetate (pH 4.3) are shown in darker blue.

With these conclusions in mind, we decided to continue using a low-salt Tris pH 8 buffer (SB or STBS) for all further EM experiments.

2.9 Structural analysis of CODV using BioSAXS

Small-angle X-ray Scattering (SAXS) is a solution scattering technique which can be used to generate low resolution envelopes of the solution structures of biological macromolecules. In addition to this shape information, SAXS can also be used to provide information as to the flexibility and number of domains a biomolecule contains. With this in mind, and with the idea that the technique might provide a low-resolution solution structure envelope which could be used to guide 3D refinement in cryo-EM SAXS experiments on *apo*-CODV and CODV-IL13-Tralokinumab were carried out (see section **2.1** for experiment details).

2.9.1 *Apo*-CODV

Figure 2.9 shows the scattering curve obtained for *apo*-CODV. It also shows the Kratky and P(r) pair-distribution plots obtained for the antibody. The Kratky plot obtained (**Figure 2.9B**) is typical of that obtained from a highly flexible or partially unfolded protein while the SIBYLS plot (**Figure 2.9C**) has a plateau, typical of those seen for multidomain, flexible proteins (Rambo & Tainer, 2011). The pair-distance or P(r) distribution function **(Figure 2.9D)** shows a maximum intramolecular dimension of the molecule (d_{max}) of 209 Å, almost identical to the maximum diameter of 210 Å observed during NS-EM of *apo*-CODV (see section **3.4.3**). It should also be noted that P(r) displays three distinct regions, a peak and two shoulders. This suggests CODV comprises three domains, consistent with the known domain structure of the antibody.

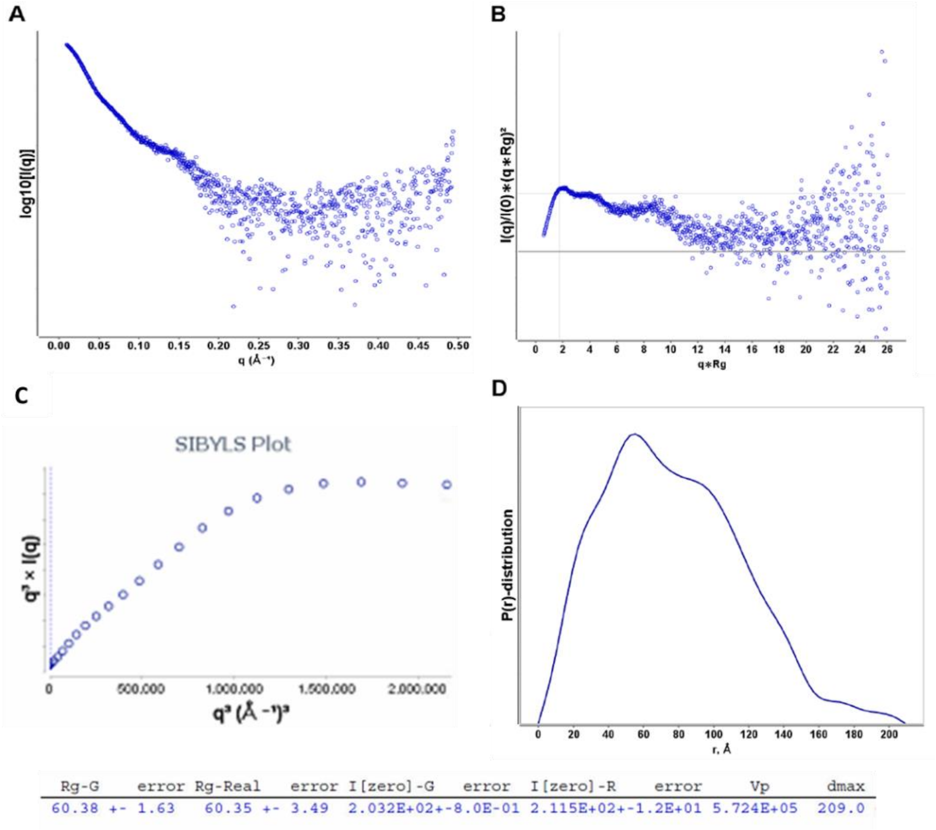

```
Rg-G     error Rg-Real    error I[zero]-G     error  I[zero]-R     error      Vp        dmax
60.38 +- 1.63    60.35 +- 3.49  2.032E+02+-8.0E-01 2.115E+02+-1.2E+01 5.724E+05  209.0
```

Figure 2.9: SAXS-analysis of apo-CODV. (A) Experimentally measured solution scattering curve. **(B)** The Kratky plot shows a curve typical from highly flexible or partially unfolded proteins. **(C)** The SIBYLS (q3 x I(q) vs q3) plot showed a plateau, typical from multidomain, flexible proteins. **(D)** The refined P(r) distribution demonstrates the existence of three clearly distinguishable domains, with a dmax of the molecule of 209 Å and a Rg of 60.38 Å (bottom).

As the SAXS data seemed to be consistent with what was previously known regarding CODV, the generation of a low-resolution molecular envelope using DAMMIF (Franke & Svergun, 2009) was attempted. However, although several *ab-inito* models were obtained, none was representative of CODV. This usually happens when molecules studied are highly flexible and thus, in this case, SAXS was not considered a candidate for obtaining an initial 3D model when working with *apo*-CODV.

2.9.2 CODV-IL13-Tralokinumab

For the CODV-IL13-Tralokinumab ternary complex a SEC-SAXS experiment was performed (**Figure 2.10**). As for *apo*-CODV (see above), the Kratky plot (**Figure 2.10B**) suggested a highly flexible molecule, with the SIBYLS plot showing a plateau characteristic of multi-domain very flexible proteins (Rambo & Tainer, 2011). As observed with CODV, the P(r) distribution also showed three domains (**Figure 2.10C**), which fit well with a maximum dimension of 306 Å. In this case, the estimated molecular weight range of the molecule was measured between 220 and 270 KDa, consistent with a 1:1:1 CODV:IL13:Tralokinumab stoichiometry.

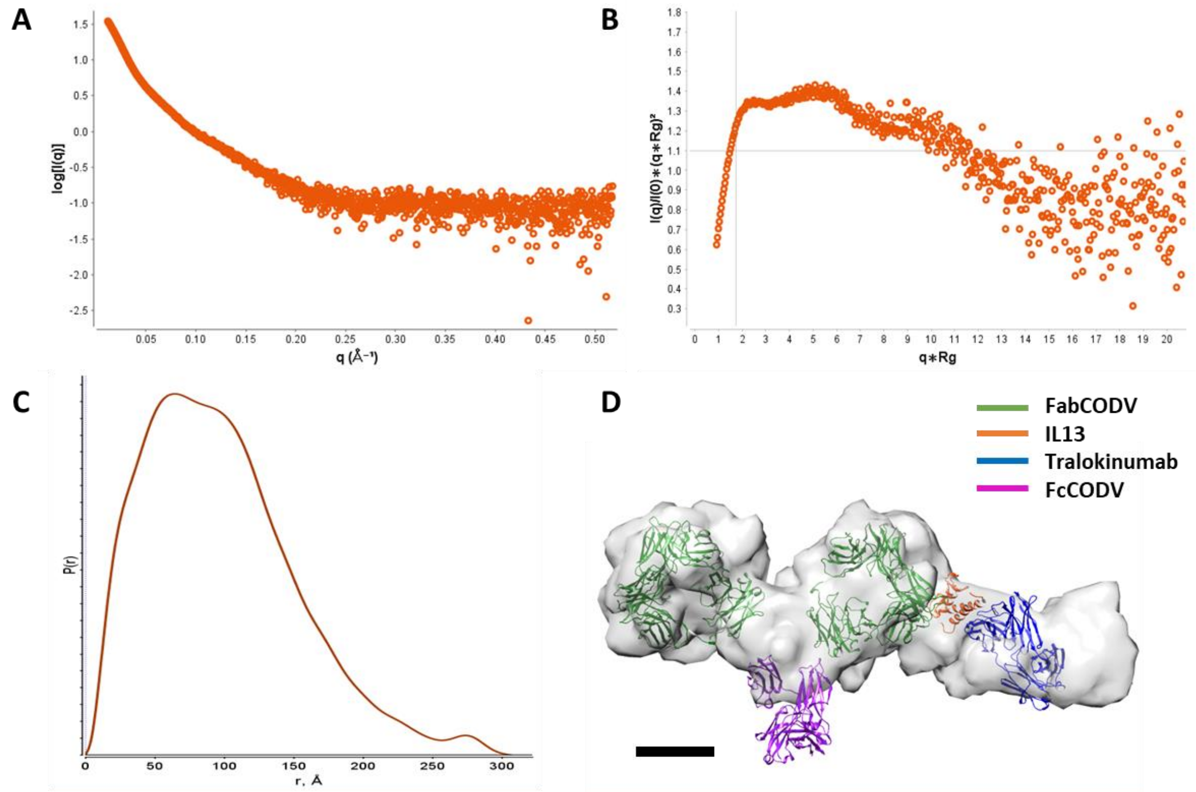

R_g	real	V_c	Volume	MW 1.07	MW 1.1	Protein	RNA	r	d_{max}	R_c	P_x
76.69	79.29	1429.5	**4.1E5** 3.8E5	**2.6E5** 2.5E5	**2.7E5** 2.5E5	**2.2E5** 0E0	**1.6E5** 0E0	98.0	306	0.00	3.0

Figure 2.10: SEC-SAXS analysis of CODV-IL13-Tralokinumab. (A) The average scattering curve obtained. (B) Similar to apo-CODV (Figure 9), the Kratky plot is typical of partially unfolded or very flexible proteins. (C) The P(r) distribution suggests three clear domains. After the refinement step several parameters could be estimated, such as the MW range. (D) DAMMIF ab-initio model results suggest a shape for 1:1:1 TC when fitted with Fab-CODV and Fab-CODV-TC (green). Density of Fc (pink) does not show likely due to flexibility. Scale bar: 50 Å.

Ab initio modelling carried out with DAMMIF (**Figure 10D**) is also indicative of a 1:1:1 CODV:IL13:Tralokinumab stoichiometry. Moreover, the low-resolution envelope obtained of one of the Fabs is similar in shape to that obtained from NS-EM analysis (see section **3.6**). However, unlike the 2D classes observed in NS-EM, where CODV showed was seen in both 1:1:1 and 1:2:2 stoichiometries, *ab-initio* models derived from the SAXS data were much more consistent with a 1:1:1 CODV-IL13-Tralokinumab complex. This contradicts the experimental molecular weight measured in mass photometry (**Figure 2.5**) where TC was shown to have a 1:2:2 stoichiometry (329 kDa). The explanation to this stoichiometry that we think seems more convincing is that in SAXS, where more than one species populates a sample, it is the points of conformer with the majority of the signal which is taken to explain the global properties of the protein in terms of size and shape. Therefore, if the single bound version of TC were to be the most populated species in equilibrium, the results could correspond to it.

That NS-EM and SEC-SAXS experiments yield similar low-resolution shapes for CODV-IL13-Tralokinumab suggesting that, in favourable cases, SAXS may be used to replace the NS-EM steps in the EM analysis of *apo*-CODV and its complexes with antigens. Nonetheless, NS-EM should always be performed even without the aim of obtaining an initial model, as it provides information about the particle behaviour and the concentration to image distribution relationship.

Chapter 3

Negative-stain electron microscopy of multispecific antibodies

Structures of apo-antibodies

-

Structures of CODV-antigen complexes

-

Antigen labelling experiments

3. Negative-stain electron microscopy of multispecific antibodies

Background

Although the protein-characterization techniques described in the **Purification and characterization** chapter give various insights on the homogeneity of the samples, they are not sufficient to assess the suitability of a protein sample for cryo-EM. In this regard, negative-stain electron microscopy (NS-EM) is a straightforward and powerful tool and is always recommended as a first step in an electron microscopy project. Compared to cryo-EM, sample preparation and image acquisition are faster and NS-EM can give ideas concerning sample quality and the relationship between sample concentration, particle dispersion and coverage in the EM grid, thus saving numerous trial and error iterations in cryo-EM sample preparation (Booth et al., 2011). Images acquired in NS-EM can also be analysed to generate low-resolution 3D reconstructions that can be used as a reference in cryo-EM data analysis (Carroni & Saibil, 2016).

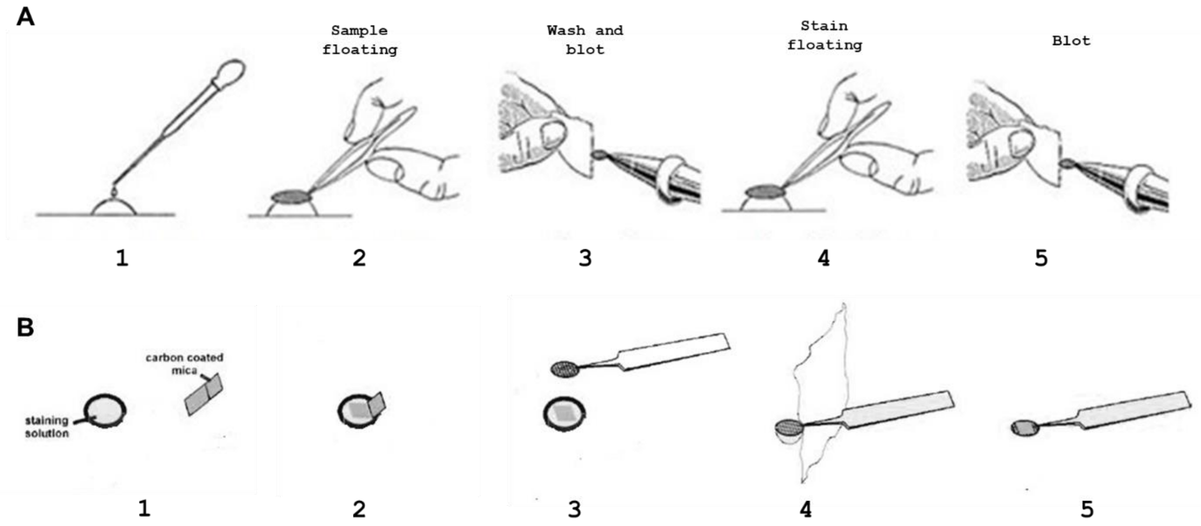

Figure 3.1: The two different techniques used in NS-EM sample preparation. The “droplet” method (A), in which the sample is either pipetted or floated onto the grid, washed several times in either water or buffer to remove excess sample and finally stained by floating the grid on a stain droplet. In the “sandwich” method (B) the carbon containing the sample is floated onto the stain and the grid added on top. Finally, the grid is blotted and air dried. Figure adapted from Doane & Anderson, 1987.

In the process of negative staining, a few µl of the sample is applied onto EM grids, usually made of copper with a continuous carbon support, treated with an appropriate stain (see below) and finally air dried. Two commonly used methods are: the *droplet* method, where the sample is applied on one of the faces of the grid and then stained; and the *sandwich* method, where the sample is loaded between a carbon coated mica sheet, stained and then deposited onto the grid (**Figure 3.1**). While both methods are effective, an advantage of the *sandwich* method is that it allows a finer regulation of the thickness of the carbon needed to adapt to different samples. The *droplet* method, on the other hand, has its main strength in the convenience of ready-made pre-coated grids, thus aiding in reproducibility of conditions. Grid treatment, with compounds or proteins (Williams, 1977) that may aid in sample dispersion or stability, is also possible in this technique.

The complexity of the microscopes used for NS-EM is typically lower than those of cryo-EM as there is less requirement for factors such as contrast enhancement or temperature control. As explained in section **1.5**, in an electron microscope, the image formation is due to scattering of the electron beam by the sample. In NS-EM the stain will appear dark as it is opaque to electrons, while the mainly carbon-rich protein sample, due to scattering of electrons, will appear in varying intensities of white. Stain opaqueness is proportional to its atomic number; the higher the number, the higher the contrast that will be achieved. Most negative-stains compounds thus consist of heavy-atom salts (Booth et al., 2011), typically uranium, tungsten, osmium or molybdenum with the particular stain being chosen depending on the pH and coarseness of grain required. The sodium silicotungstate (SST) stain used in this project has a relatively fine grain and suitable for small to medium molecular weight (~200 kDa) samples. Although the contrast obtained when using SST is not strong, it can be titrated to neutral pH which is an advantage for the samples studied in this thesis.

In the following sections, NS-EM will be shown as a valid tool for not only acquisition of 2D and 3D references of TDT, TBTI and of *apo*-CODV and its complexes with antigens, but also as a potential technique for rapid assessment of antibody-antigen binding.

Methods

3.1 Grid preparation

Staining was performed using the “sandwich” method (**Figure 3.1B**). Of the various stains tried, 2% SST was found to be suitable for all three types of antibodies. For sample preparation, 3 µl of a solution containing antibody or antibody-antigen complexes were pipetted in between a mica-carbon sheet which, after few seconds of incubation, was slowly inserted into the well containing the stain. The mica sheet was then carefully removed and the sample left in the stain for about 20 seconds, after which a 400-mesh copper grid was deposited onto it. As a last step, the whole carbon-grid assembly was picked up using a tweezer and blotted against a filter paper and air-dried. For good particle distribution, the optimal sample concentrations were observed to be around 10 µg/ml for CODV-antigen complexes and 15 µg/ml for *apo*-CODV alone. For TBTI and TDT, the concentrations used in NS-EM experiments were 7.5 µg/ml and 12 µg/ml, respectively.

In order to try to definitively identify the position of IL4 in the CODV-antigen complexes, NS-EM with gold labelling was also attempted. Here, Ni-NTA-bound 5 nm Nanogold® beads (Nanoprobes) that should bind to the N-terminal hexa-histidine tag of IL4 were used. Two methods were tried for this labelling technique.

In the first, Nanogold® beads at 0.5 µM in Au binding buffer (20 mM Tris, 150 mM NaCl, 0.1% Tween 20, pH 7.5) were mixed with 10 µg/ml of CODV-IL4 at molar ratios of 1:5 or 1:10 in excess of beads. The resulting solution was incubated for at least 30 minutes before being transferred into a grid for imaging. The grids were prepared using both the sandwich method and the droplet method with SST as the stain. In various attempts, before staining, an extra washing step was performed with washing buffer (20 mM Tris, 150 mM NaCl, 20 mM imidazole, pH 7.5) to remove non-specifically bound Nanogold® beads.

In the droplet method, 4 µl of CODV-IL4 (7.5 µg/ml) was first applied onto a carbon pre-coated copper grid. The excess solution was blotted and the grid was floated for 1 minute on a drop of 0.1% BSA solution in DPBS. The grid was blotted again and then floated on a drop containing a 5nm Nanogold® solution (protein:gold molar ratio of 1:10 or 1:20) in DPBS with 0.1% BSA to remove non-specific interactions. After 20 minutes, the grid was blotted and washed 3 times by floating it on water droplets and finally stained by floating on a drop of 2% SST for 20 seconds.

3.2 Data collection

All NS-EM experiments were carried out at the Grenoble Partnership for Structural Biology (PSB) electron microscopy platform (Institut de Biologie Structurale, Grenoble, France; https://www.psb-grenoble.eu/spip.php?rubrique34). To optimize the grid preparation conditions, initial screening was carried using a Tecnai T-12 120 keV transmission electron microscope (Thermo Fisher Scientific) fitted with an Gatan Orius SC 600 camera (AMTEK). Once good conditions were found, to obtain better quality NS-EM data for further image analyses, grids were re-prepared and imaged using a Tecnai F-20 200 keV microscope equipped with a 4K x 4K Ceta CMOS (Thermo Fisher Scientific) camera. Micrographs (see **Table 3.1** for details of all NS-EM data collections) were recorded using the Digital Micrograph software (Gatan) under low-dose mode.

Sample	Magnification (pixel size in A)	Defocus range	No. of micrographs
TBTI	62000x (1.7)	1-2 µm	54
TDT	50000x (2.1)	1.5-3 µm	64
CODV	62000x (1.7)	1-3 µm	150
CODV-IL4	62000x (1.7)	1-3 µm	71
CODV-IL13	62000x (1.7)	1-3 µm	116
CODV-IL4/IL13	50000x (2.1)	1-3 µm	71
CODV-IL13-Tralokinumab	62000x (1.7)	1-3 µm	81
CODV-IL4/IL13-Tralokinumab	62000x (1.7)	1-2.5 µm	62

Table 3.1: Data collection parameters for all antibody and antibody-antigen complexes imaged by negative-stain EM.

3.3 Image Processing

The general workflow used for the processing of the NS-EM micrographs obtained is shown in **Figure 3.2**. Estimation of CTF parameters was carried out using CTFFIND4. (Rohou & Grigorieff, 2015) Unless otherwise specified, particles were picked fully automatically using the Laplacian or Gaussian (LoG) blob detection algorithm implemented in RELION 3.0

(Kimanius et al., 2016). Due to limited resolution available from the NS-EM images, particles were extracted with flipped phases and not full-CTF correction. For all the NS-EM datasets further image processing (**Figure 3.2**) was performed using RELION. Model fitting inside the EM density was carried out using the rigid-body fit module of UCSF Chimera (Pettersen et al., 2004).

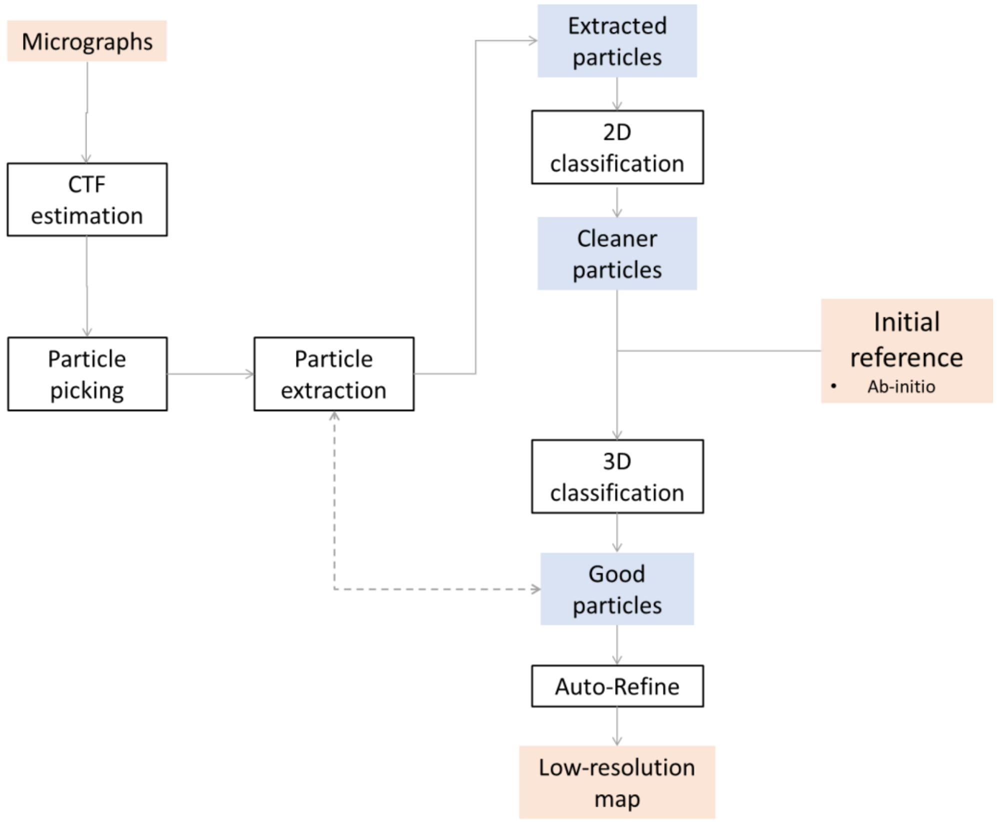

Figure 3.2: Schematic workflow of NS-EM micrograph processing. Start and end points are represented in orange and particle sets in blue. As indicated by the dotted arrow-line, the process can be iterative to optimize the picking and extracting centred particles.

Results

3.4 Structures of *apo*-antibodies

3.4.1 TBTI

For TBTI (**Figure 3.3**), around 30000 particles were automatically picked using 180 Å and 230 Å as the minimum and maximum particle diameters of the LoG filter. A high picking threshold was necessary to minimize false positive hits from the micrographs. Particles were extracted with a box size of 200 pixels (338 Å) and then subjected to 2D classification.

Several 2D classes with reasonably well-defined electron densities for individual domains of TBTI were obtained when relatively high *Tau-Fudge T* values (4 and 5) were used. In few words, T essentially determines how much weight the high frequency region of the power spectrum of images has when aligning particles. Higher values may mean higher resolution but also higher noise overfitting (Scheres, 2012). Classes with poorly defined densities were removed. The final set of 2D class averages (**Figure 3.3B**) exhibited flexibility between fragments, and within each Fab domain as well. Notable flexibility was observed in Fv2, which likely interferes with the alignment of this domain leading to blurry densities (second 2D class, **Figure 3.3B**). This coincides with previously published data (Jakob et al., 2013) that points towards a “saddle-like” movement caused by multispecific antibody domain linkers and already referred to in the **Introduction** chapter**.**

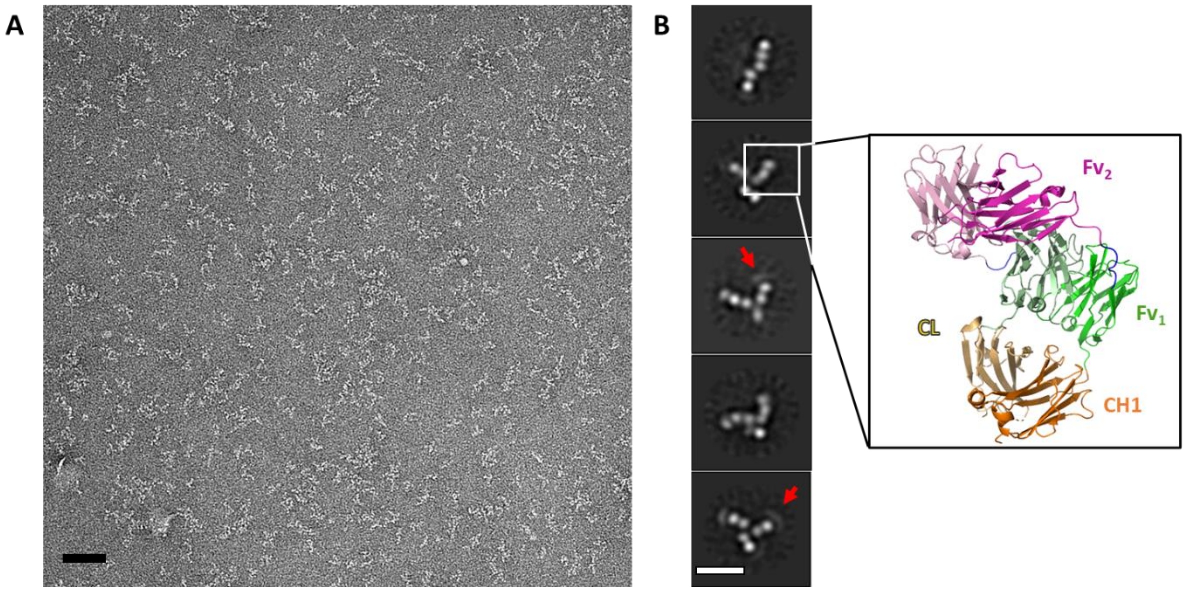

Figure 3.3: Negative-stain electron microscopy of TBTI. (A) Representative micrograph of TBTI at a magnification of 62000x (1.69 Å/pix) (scale bar = 500 Å). **(B)** The 2D classes obtained suggest considerable flexibility of the molecule, especially at the Fv2 domain (red arrow). Nonetheless, in many cases all three Fab domains of the antibody (box, structure of a similar DVD-Ig (PDB code: 4HJJ; (Jakob et al. 2013)) can be identified. Scale bar = 100 Å.

While densities corresponding to the Fab domains (namely CH1, Fv1 and Fv2) appear very frequently in the class averages, it is only in some cases where Fc is discernible. While CH1 and Fv1 have clear densities across all classes, thus evidencing a more limited movement of this domain, Fv2 seems blurrier in many classes suggesting a more dynamic movement (marked with a red arrow in classes 3 and 5 of **Figure 3.3B).** A characteristic turn or bend of the Fab arms can be seen in most classes (magnified in **Figure 3.3B**). The flexibility became more apparent when trying to generate 3D maps from the particles, which did not converge to a TBTI-like reconstruction and therefore was not included here.

3.4.2 TDT

Data collection for TDT (**Table 3.1**, **Figure 3.4**) consisted of a total of 100 micrographs of which 36 were collected with a magnification of 62000x and 64 at 50000x (pixel sizes 1.69 Å and 2.09 Å, respectively). Due to lower particle density per micrograph, only the data set at 50000x was considered for further image analysis (**Table 3.1**). About 42000 particles were automatically picked using 180 Å and 230 Å as the particle diameter limits and extracted using a box size of 150 pixels (313.5 Å). After removing bad classes from the 2D classification with T=1, 21598 good particles were subjected to another round of 2D classification with a very high T value (T=10). This yielded better class averages, some of which are shown in **Figure 3.4B**.

Unlike TBTI (see **Figure 3.3**), the 2D class averages of TDT have higher signal to noise for all three antibody fragments, in particular showing better definition for Fc. Coinciding with this observation, the 3D reconstruction obtained from TDT particles (**Figure 3.4C**) shows density for all the three fragments. However, conformational flexibility still can be observed, especially between fragments rather than within each of the Fabs. The inter-fragment flexibility can be explained due to the nature of the hinge binding them, while the general reduction in Fab-flexibility might be due to the self-supporting architecture of the CODV-Fab and the absence of a third domain in the anti-TNFα IgG-Fab.

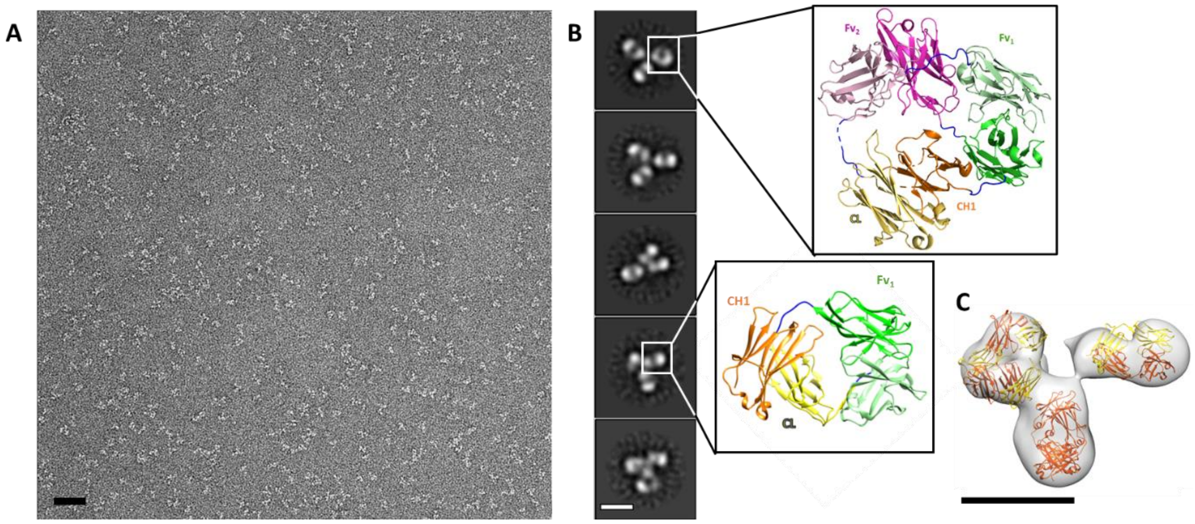

Figure 3.4: NS-EM analysis of the trispecific antibody TDT. (A) Representative F20 micrograph collected at 12 µg/ml and a magnification of 50000x (scale bar: 500 Å). **(B)** The 2D classes obtained show easily recognizable fragments in different orientations. The Fc appears as a clear domain, while the IgG-Fab (bottom box, PDB code: 3FZU; (Houde et. al 2009)) and CODV-Fab (top box, PDB code: 5HCG; (Steinmetz et al. 2016)) can be distinguished in most cases. **(C)** Example of a 3D class of TDT. The Fabs are well resolved and can be identified, while the Fc density (PDB code: 4NQS; (Elliott et. al 2014)) shows lower resolution (scale bar = 100 Å). Heavy chains are orange, light chains are yellow.

3.4.3 *apo*-CODV

For *apo*-CODV (**Figure 3.5**), a total of 57772 particles were picked automatically with RELION (200 Å and 260 Å as particle diameter limits) and extracted to a 2x binned box size of 84 pixels (284 Å, pixel size 3.38 Å). 2D classification on these particles yielded good class averages in which all three fragments of the antibody were visible (**Figure 3.5B**). As expected, the class averages also exhibited inter-fragment flexibility.

However, and unlike for TBTI and TDT (see above), most class averages of CODV corresponded to only a few views, suggesting preferential orientation on the EM grid, an additional complexity to reach high resolution. However, as much of this thesis work is focussed towards the cryo-EM analysis of *apo*-CODV and its complexes with the antigens, image processing was continued further in order to obtain a 3D NS-EM reconstruction of CODV which could be of help as an initial model for the processing of cryo-EM images.

A total of 39243 particles from the cleaned 2D classes were thus selected and the initial 3D model generation was spread through 10 classes with the aim of tackling the flexibility issue. The *ab-initio* 3D initial model generation job was launched with RELION 3, through 500 iterations and a C1 symmetry, only performing phase flipping for the CTF correction. The models obtained have density for all the three fragments (**Figure 3.5C**). However, as this is larger than expected for the Fab fragments indicates sub-optimal alignment due to flexibility. A continuous heterogeneity can be envisaged as all the 10 models were equally populated with notable differences in the orientation between the fragments, just as in the 2D classes (classes 1-3 in **Figure 3.5B**, for example). This continuous large-scale flexibility/heterogeneity is likely a result of the hinge, which do not place hard constraints on the movement of the individual CODV domains. The flexibility at Fc, has already been described as an advantage towards extending the Fab range of antigen capture (Sandin et al., 2004).

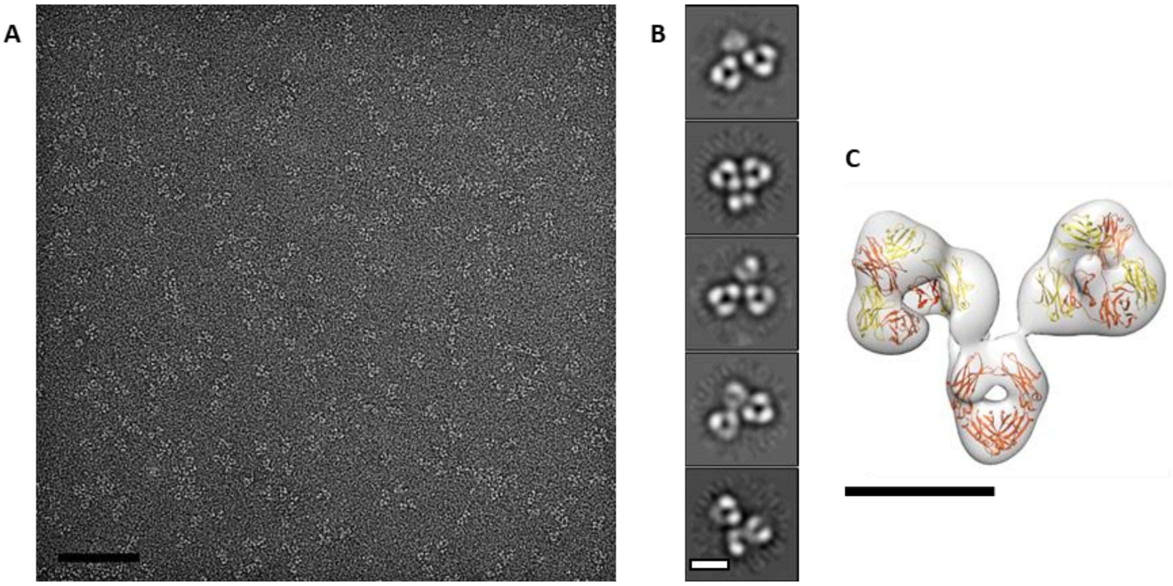

Figure 3.5: NS-EM analysis of CODV. (A) Representative micrograph of CODV at 15 µg/ml with SST at 62000x magnification (scale bar = 100 nm). Particles were sufficiently well-spread and identifiable, although closer-to-focus imaging led to images with lower contrast. **(B)** Representative 2D classes showing all domains of the protein in different conformations (scale bar = 100 Å). **(C)** Example reconstruction of CODV after 3D classification, fitted with crystal structure of knob-in-hole Fc (PDB code: 4NQS; (Elliott et. al 2014)) and Fab-CODV (PDB code: 5HCG; (Steinmetz et al. 2016)) (Scale bar = 100 Å).

The NS-EM analysis of TBTI, TDT and CODV at moderate resolution (20-30 Å) confirms that all three antibodies exhibit flexibility at different levels depending on the type and length of linkers between fragments and domains and as well on the type of Fab domains. Based on the analysis carried out here, TBTI has the highest flexibility between the three fragments (2 Fabs and Fc) leading to complete absence of Fc density in most classes. Moreover, it is clear that the linkers connecting the Fvs result in higher degrees of freedom in movement for this domain resulting in blurry density.

TDT and CODV (**Figure 3.4**, **Figure 3.5**) exhibit comparable levels of flexibility between and within their Fab fragments. Having a short or self-supported Fabs, as it is the case with CODV and TDT, clearly results in better NS-EM densities. However, in the case of CODV the similar size of all three domains of the Fab seems to lead to particle alignment issues. This often leads to an extra density in the Fab regions of low-resolution 3D models obtained. In terms of structure analysis, the binding of antigens to specific Fab domains might help to overcome this alignment issue.

3.5 Structures of CODV-antigen complexes

3.5.1 CODV-IL4

All CODV-antigen complexes were prepared as described in the **Purification and characterization** chapter**.** For NS-EM analyses of CODV-IL4 (**Figure 3.6**), 71 micrographs with good CTF and particle distribution (**Figure 3.6A**) were selected, from which 49996 particles were picked automatically using 190 and 210 Å as the minimum and maximum particle diameter limits. These were then extracted to a box size of 100 pixels (338 Å, binned 2x) and subjected to reference-free 2D classification.

Representative 2D classes are shown in **Figure 3.6B**. While the Fc region of the antibody is blurred in most of the classes, indicating higher inter-fragment flexibility, the electron densities for Fab domains appear to be of better resolution than seen for CODV. A reasonable explanation for this is that the binding of IL4 to the Fab domains has either reduced the inter-domain flexibilities of the Fab fragments or resulted in better alignment of these domains. Unexpectedly, however, and despite the fact that binding of IL4 to CODV in solution has been confirmed using CODV-antigen chromatography, western blotting, pulldown affinity experiments, mass photometry and SDS-PAGE (see the **Purification and characterization** chapter), and that SPR experiments showed a very strong CODV-IL4 affinity (k_D =10 pM), density attributable to the IL4 antigen was not discernable in any of the classes.

To explain the lack of IL4 density in the class averages, one can think of two possible explanations: 1) As IL4 is relatively small (14 kDa) compared to either Fab or Fc, and the CODV molecule exhibits high level of inter-domain flexibility, the alignment of such flexible fragments could make the electron density corresponding to IL4 less discernible; 2) Although less likely due to the high binding affinity between CODV and IL4 in solution, the CODV-IL4 complex dissociates on the EM-grid. To verify the latter, NS-EM gold-labelling experiments were performed using Ni-NTA-bound 5 nm Nanogold® beads that bind to 6X-histidine tags. (see section **3.6.1**).

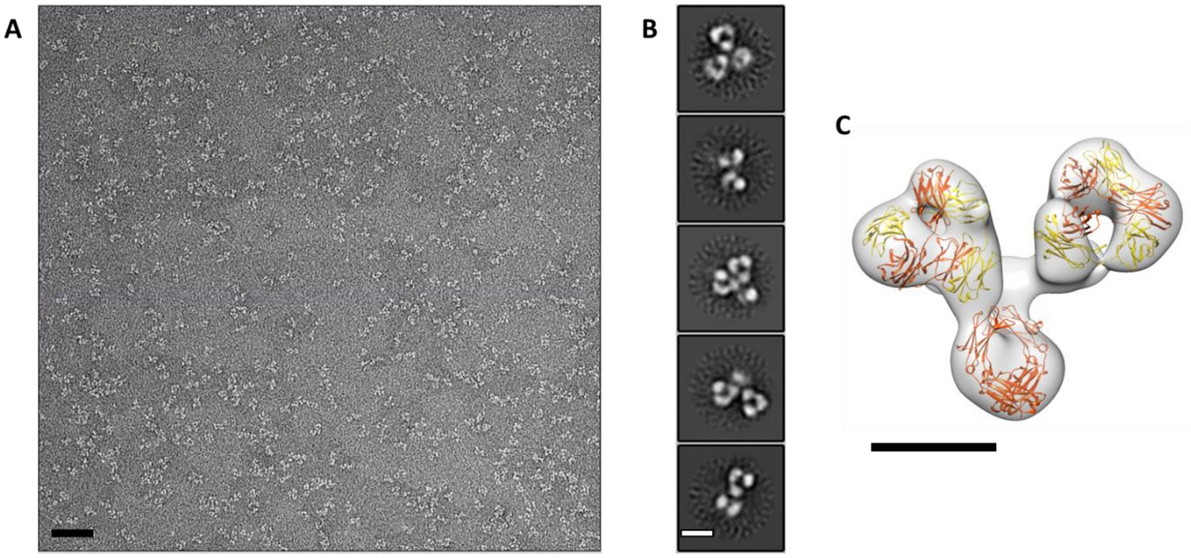

Figure 3.6: NS-EM analysis of CODV-IL4. (A) Representative micrograph of CODV at 10 µg/ml with SST at 62000x magnification (scale bar = 500 Å). **(B)** A selection of 2D classes showing many different conformations of the antibody and in some cases (such as the first class), when using high T values, the clear density of the rhomboid-shaped Fc could be discerned (scale bar = 100 Å). **(C)** Representative 3D class of CODV-IL4, fitted with structures of IgG Fc (PDB code: 4NQS; (Elliott et. al 2014)) and Fab-CODV (PDB code: 5HCG; (Steinmetz et al. 2016). Fc was visible in very few classes and that area was therefore less well-defined during 3D classification steps (scale bar = 100 Å).

3.5.2 CODV-IL13

For the CODV-IL13 dataset (**Figure 3.7**), 116 micrographs were autopicked using a LoG filter with diameters ranging from 180 to 240 Å. 30666 particles were picked with a box size of 100 pixels (338 Å, 2x binned), and after several 2D classification steps for cleaning, a subset of 12556 particles were used for 3D *ab-initio* model generation and classification. Because of the flexibility observed during the 2D steps (**Figure 3.7B**), for 3D classification a high T value (T = 10) proved more successful in obtaining classes with density for all the three domains of the Fabs. It should be noted that while high T values can often result in overfitted classes, their use when noise particles are cleaned allows better 2D classification of flexible molecules. This is due to higher values of T giving more weight to higher frequencies (therefore, finer detail) of the particles' power spectra when performing alignment (Scheres, 2016).

3D auto-refinement performed on the most highly populated 3D classes resulted in reconstructions in the 25-30 Å resolution range showing densities for all the three fragments (one of the reconstructions is shown in **Figure 3.7C**).

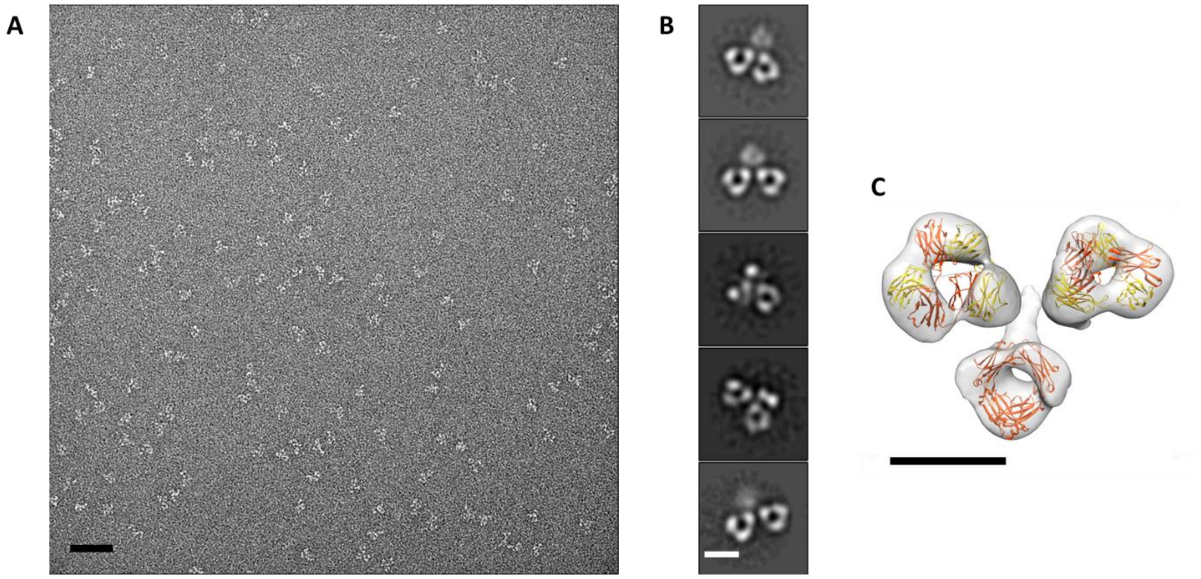

Figure 3.7: NS-EM analysis of CODV-IL13. (A) Representative micrograph of CODV-IL13 at 11 µg/ml with SST at 62000x magnification (scale bar = 500 Å). **(B)** The 2D classes obtained showed different conformations for the same view, but overall resembled the results obtained for apo-CODV (scale bar = 100 Å). **(C)** Representative 3D reconstruction of CODV-IL13. Fc was more present in 2D classes compared to CODV-IL4 probably due to an increased particle number, and as a result 3D classes were better defined. (scale bar = 100 Å).

Unfortunately, as in the case of CODV-IL4, density for the IL13 antigen was not observed in either the 2D or the 3D steps of the image processing pipeline. Thus, in parallel to attempts at confirming the presence of the bound antigen on the EM grids using Tralokinumab binding for IL13 (see section **3.6.2**), we also analyzed the CODV-IL4/IL13 double complex with the ideas that: 1) The binding of two antigens might help stabilize the Fab domains (i.e. less flexibility); 2) The double complex will be of larger size that could aid the alignment.

3.5.3 CODV-IL4/IL13

71 micrographs with correct CTF estimation (**Figure 3.8A**) were subjected to LoG picking with minimum and maximum diameter filters of 180 and 280 Å. This resulted in 60696 particles, which were then extracted to a box size of 90 pixels (376.2 Å, 2x binned). 2D classification was performed to remove bad particles, resulting in 45938 particles. Interestingly, many of the 2D class-averages look different from those observed for CODV, CODV-IL4 and CODV-IL13. In particular, in the class-averages with higher particle count (last

two classes in **Figure 3.8B**), only two regions of density were seen for each fragment. Compared to projections obtained from the surface generated for the CODV-Fab crystal structure (PDB: 5HCG), it is possible that these classes indicate the top view of the Fabs.

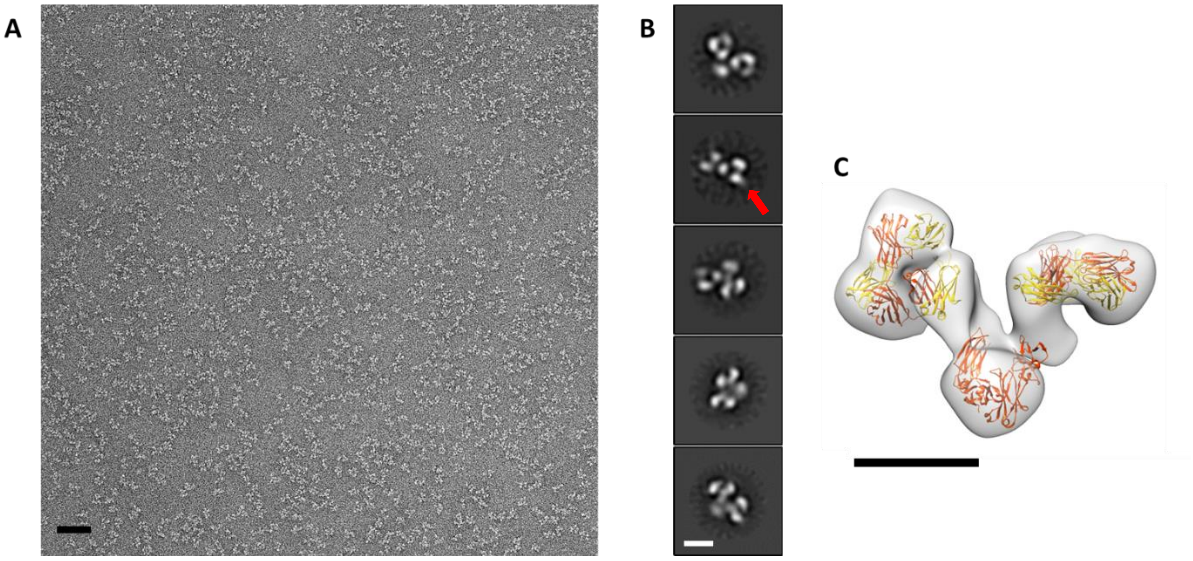

Figure 3.8: NS-EM analysis of the CODV-IL4/IL13 double complex. (A) Micrograph at 50000x magnification of CODV-IL4/IL13 at 9 µg/ml with SST (scale bar = 500 Å). **(B)** Representative 2D classes showing different orientations of the molecule such as front (first class) and top (last two classes) views (scale bar = 100 Å). A possible extra density at Fv2 is marked with a red arrow in class 2. **(C)** Representative 3D class of the double complex, with a characteristic orientation of the CODV-Fabs perpendicular to each other. This specific conformation may be noted in class 3 of **(B).** Scale bar = 100 Å.

2D classification steps were attempted with different number of classes and T values and, perhaps due to a higher particle count within the dataset, a few classes presented an extra, blurred density at Fv2 (such as the second class (red arrow) in **Figure 3.8B**) which might correspond to the binding site of IL13. However, reconstructions from the 3D *ab-initio* and 3D classification steps (**Figure 3.8C**) did not show any additional density at Fv2 and instead resemble a *apo*-CODV in a similar manner to the single complex datasets processed.

3.6 Antigen labelling experiments

As described above and in the **cryo-EM of CODV antibodies** chapter, all analyses by both NS-EM and cryo-EM aimed at discerning the binding positions for IL4 or IL13 in binary CODV-antigen complexes did not produce any conclusive results. This is despite the fact that biophysical characterization confirmed antigen binding in solution. It was therefore decided to verify the presence of bound antigens on the EM grids. Here, gold labelling was used to target the N-terminal His_6-tag of IL4 (CODV-IL4 complex) while a conventional Fab moiety

(Tralokinumab) which binds to IL13 was used in experiments analysing the IL13 binding to CODV.

3.6.1 Gold labelling of IL4

As shown in **Figure 3.9**, in most cases, gold beads (red arrows) were seen in the background and not bound to antibodies. Imidazole washing steps when having high gold ratio also did not help to remove the excess unbound gold and led to breakage of the carbon support. Considering the 50 Å diameter of the gold beads, steric hindrance was not considered an explanation for the non-binding observed, as the N-terminus to which the NTA-gold binds is exactly opposite to the epitope on IL4 when observed on UCSF Chimera (**Figure 3.10**).

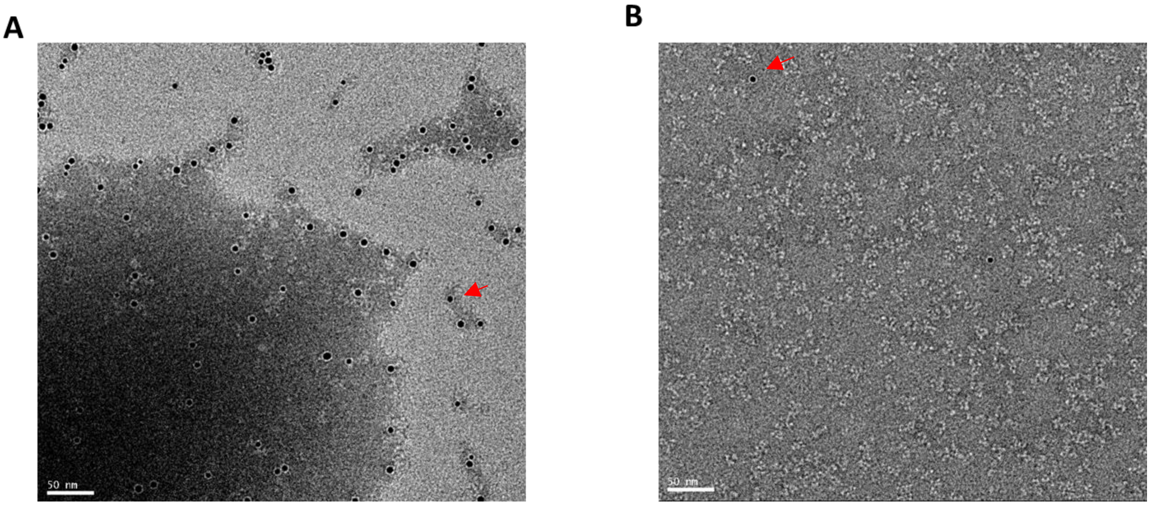

Figure 3.9: NS-EM micrographs following gold labelling of CODV-IL4. Attempts to clearly label the His6-tag of IL4 were unsuccessful, with micrographs not showing specific binding (red arrow) only in cases with a higher concentration of Nanogold **(A)** and not binding to any protein when at very low concentrations **(B).** Scale bar = 500 Å.

Labelling using the BSA protocol was also unsuccessful, as excess BSA covered the entirety of the grid and obstructed the density corresponding to the antibodies, irrespective of the number of washing steps performed.

This experiment, therefore provided no conclusive evidence that IL4 remains bound to CODV on EM grids. With these results in mind, alternative strategies were considered in order to successfully label antigens bound to CODV in EM experiments.

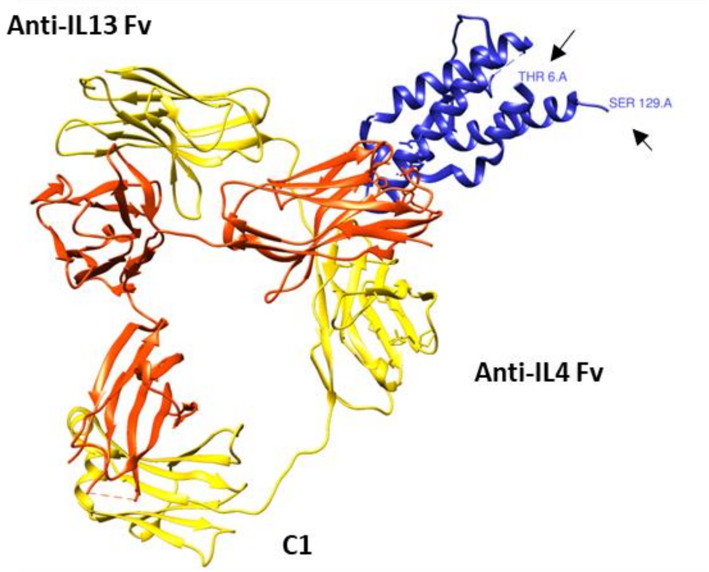

Figure 3.10: FabCODV-IL4 crystal structure. IL4 (in blue) has both N and C termini opposite to the binding site, therefore there is sufficient space for molecules to bind to the histidine tag at the N-terminus. Heavy and light chains of FabCODV are in orange and yellow, respectively. PDB code: 5FHX (Steinmetz et al. 2016).

3.6.2 Fab labelling of IL13

As the IL13 construct used in the experiments described here does not contain a His_6 tag, gold labelling to confirm its binding to CODV on the EM grid could not be attempted. Fortunately however, a conventional Fab, (Tralokinumab (Popovic et al., 2017), PDB:5L6Y), binding with high affinity and selectivity to IL13 is available. Moreover, as IL13 exhibits different binding sites (one for CODV and Lebrikizumab (Ultsch et al., 2013), another for Tralokinumab) which are on opposite sides of IL13 (**Figure 3.11**), labelling of IL13 with Tralokinumab could indicate the presence of IL13 in CODV antigen complexes containing IL13. On this basis, a ternary CODV-IL13-Tralokinumab complex (TC) was purified for NS-EM and cryo-EM experiments (see **Purification and characterization)**.

During the grid optimization steps at the Tecnai T12 microscope, it was already easy to identify particles containing the additional tralokinumab (**Figure 3.12A**). In order to perform image analysis, better quality micrographs (sample concentration 9 µg/ml) were recorded on the PSB EM platform's Tecnai F20 microscope. From this latter dataset, 36 micrographs were selected according to their CTF using GCTF (Zhang, 2016), where good quality Thon rings and no apparent astigmatism were observed. Similar to the other antibody data sets, particles were picked automatically using the LoG algorithm (11900 particles), with upper and lower diameter filters of 300 to 440 Å, respectively. In order to account for CODV-IL13 particles bound to two Tralokinumabs, which had been observed in raw images as extended particles, a larger box size of 140 pixel (473 Å and 2x binned) was used for extraction. Reference-free 2D classification produced several 2D classes exhibiting clear binding of Tralokinumab to CODV-IL13, and for the first time the IL13 antigen was visible. Furthermore, in all the classes, the Tralokinumab Fab attachment to IL13 is at a fixed angle of approximately 135 degrees relative to the IL13 paratope of the CODV-Fab (**Figure 3.12B**), indicating rigidity at the IL13-Tralokinumab junction.

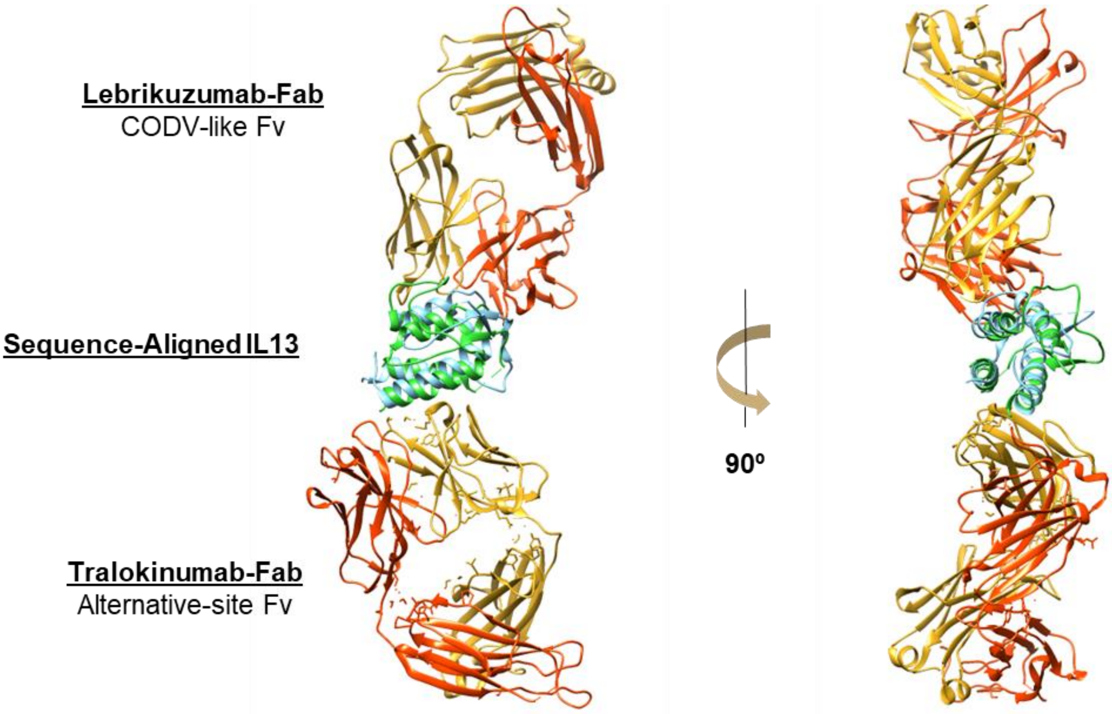

Figure 3.11: Comparison of the Lebrikizumab (CODV-like) and Tralokinumab binding sites on IL13. CODV binds to the same epitope as Lebrikizumab (PDB: 4I77; (Ultsch et al. 2013)) which is opposite to that for Tralokinumab (PDB: 5L6Y; (Popovic et al. 2017)). These antibodies have different mechanisms of action when preventing binding of IL13 (blue for Lebrikizumab, green for Tralokinumab) to IL13 and IL4 receptors. Heavy chains are in orange, light chains in yellow.

Using default parameters in 2D classification in RELION along with a wider mask (440 Å) resulted in classes having either one of the CODV Fab regions bound to IL13-Tralokinumab (**classes 1-3 in Figure 3.12B**), and classes containing CODV bound to both one and two IL13-Tralokinumab complexes (**classes 5 and 6 in Figure 3.12B**). A subset of classes also hinted at a small population of *apo*-CODV with no density for IL13-Tralokinumab (example in **class 4 of**

Figure 3.12B). It is not clear at this stage whether this latter class contained *apo*-CODV particles dissociated of IL13-Tralokinumab or whether it was an effect from the alignment.

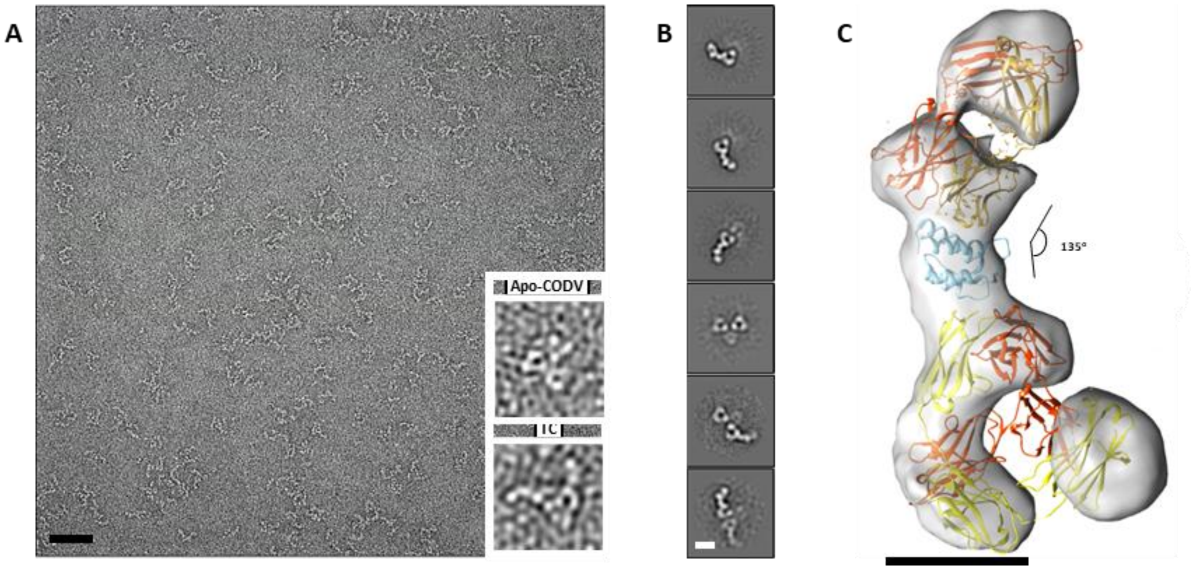

Figure 3.12: NS-EM analysis of the CODV-IL13-Tralokinumab triple complex. (A) 9 µg/ml micrographs at 62000x magnification (scale bar = 500 Å), with comparison of raw particles from apo-CODV and TC datasets. **(B)** The 2D classes obtained were diverse, alignment mainly driven by the stable IL13 binding interface (scale bar = 100 Å). In some classifications free-CODV (class 4), single-bound (5) and double-bound (6) complexes could be obtained. **(C)** When using a Fab-IL13-Fab focused approach, 3D reconstructions such as the one shown here could be obtained, and rigid body fitted with the crystal structures of CODV (PDB: 5HCG) and Tralokinumab-IL13 (PDB: 5L6Y). Scale bar = 50 Å.

As the FabCODV-IL13 interface in the ternary complex was better defined owing to the binding of Tralokinumab, different views could be identified with confidence. In order to boost the signal for the FabCODV-IL13-Tralokinumab regions, a slightly different approach, aligning the particles by focussing only on this part of the triple complex was attempted. Here, a tighter mask of about 220 Å diameter was used. This yielded several classes with better densities for the above three components. sAn initial model of FabCODV-IL13-Tralokinumab with the 3407 refined particles corresponding to the 4 best classes was thus generated. A 3D refinement was performed using the initial model obtained and a tight mask generated from the initial model in order to avoid the signal from the neighbouring parts of the full complex. The resulting map clearly showed the densities for CODV-Fab, IL13 and Tralokinumab and a model was generated in UCSF Chimera by the rigid body fitting of the crystal structures of Tralokinumab-IL13 and CODV-Fab (**Figure 3.12C**).

Analysing the results obtained above, there are two possible reasons why IL13 could be seen during the image processing step for the ternary complex and not for CODV-IL13 alone: 1) The Tralokinumab Fab aids in the correct particle alignment and thus the antigen signal-to noise can be boosted; 2) Tralokinumab stabilizes binding of IL13 to CODV, thus ensuring IL13 remains attached to CODV during EM grid preparation.

To test which of these assumptions might be true, a quaternary IL4-CODV-IL13-Tralokinumab complex was prepared (see **Purification and characterization**) and NS-EM analysis carried out. Here (**Figure 3.13**, 62 micrographs collected and processed following the same procedure as for CODV-IL13-Tralokinumab. After 2D and 3D cleaning, a subset of 15165 particles was selected for further processing. The 2D classes obtained (**Figure 3.13B**) did not show an additional density at Fv1 corresponding to IL4. Additionally, 3D classification outputs (**Figure 3.13C**) also showed no density for IL4 in all the models produced.

The results outlined above clearly suggest that EM imaging of CODV in complex with small antigen requires stabilisation of CODV-antigen binding interface in some way or another. Using an antibody fragment to assess correct orientations of the particles during the classification steps is useful but does not seem to be the key factor in helping see the antigen. What we believe is contributing to the signal of the antigen showing is the presence of a clear, larger density accompanying it.

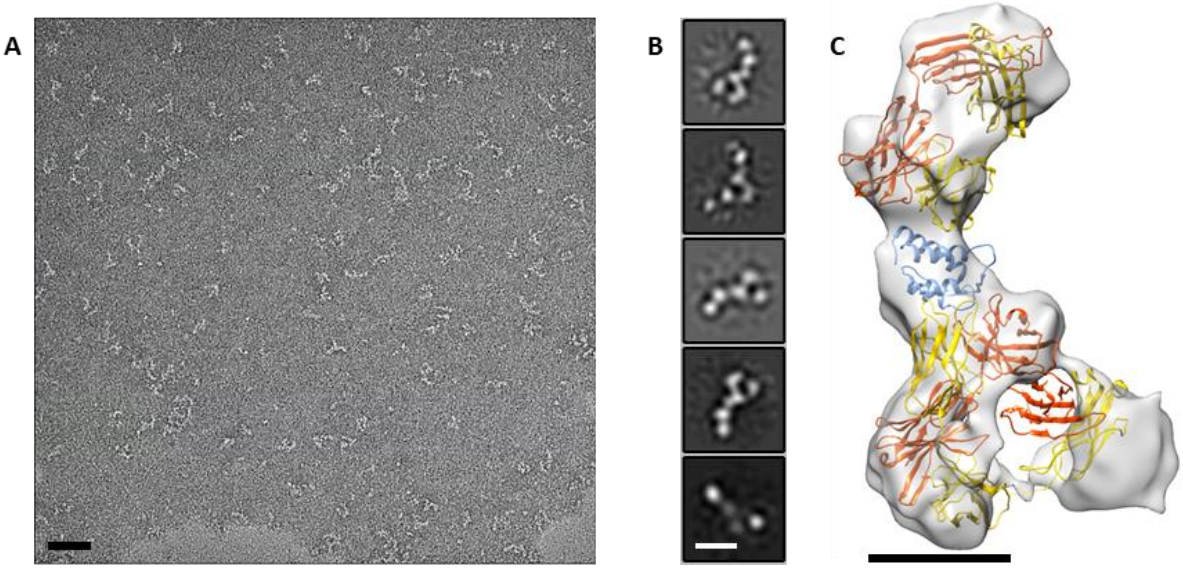

Figure 3.13: NS-EM analysis of the CODV-IL4/IL13-Tralokinumab quadruple complex (QC). (A) Representative micrograph at 9 µg/ml, which showed lower particle coverage compared with other CODV datasets. (Scale bar = 500 Å). **(B)** 2D classification produced similar results to those obtained for CODV-IL13-Tralokinumab (Figure 11) and no IL4 density could be discerned at Fv1 (scale bar = 100 Å). **(C)** IL4 was also not present on the 3D classification jobs performed on the dataset, when rigid body fitted with the crystal structures of CODV (PDB: 5HCG) and Tralokinumab-IL13 (PDB: 5L6Y). (scale bar = 50 Å)

The crystal structure of CODV-IL4 (PDB: 5FHX) reveals that both N- and C- termini of IL4 are located opposite its CODV binding site. Thus, for CODV-IL4, one possibility not further investigated here, is the use of an antibody (anti-His_6 Fab or scFv) that can bind to the N-terminal His_6-tag of IL4. While not strictly locking or stabilizing proteins, these fragments might aid in EM image processing by adding an additional density.

Based on the results outlined above, CODV was considered as the main target for the cryo-EM part of the project. While NS-EM experiments clearly revealed a high level of flexibility, the self-supporting Fab architecture of CODV restricted intra-Fab movement and, at least during the 2D steps of the pipeline, made antibodies themselves easily identifiable. It was hoped that this restriction of movement would translate into a better chance of successfully obtaining a single particle cryo-EM reconstruction at reasonable resolution, which was considered one of the primary goals of this work. Additionally, the anti-IL4/IL13 CODV construct has a higher therapeutic interest (see **Introduction**) than the other formats investigated using NS-EM.

Chapter 4

Cryo-electron microscopy of CODV antibodies and its complexes

Design of a cryo-EM pipeline for multispecific antibodies

-

CODV-IL13 structure solution complexed with Tralokinumab

4. Cryo-EM of CODV antibodies and their complexes with antigens

Background

Recent advances in both hardware and software have pushed the limits in size and resolution (Kühlbrandt, 2014) attainable in cryo-electron microscopy with the result that the technique is now routinely used in the study of increasingly complex systems. Moreover, as the results of more and more studies are published it has become increasingly easier to elucidate starting points for the testing and optimisation of EM sample preparation conditions. This latter aspect particularly concerns the search for the optimal preparation of cryo-EM grids for use in single particle reconstruction experiments.

Unfortunately, most publications describing cryo-EM studies of antibodies (Hao et al., 2019; Oyen et al., 2018) have, thus far, focused on their Fab regions, with the goal of elucidating the interaction of their CDRs (complementarity determining regions) with their corresponding antigens. While it is reassuring to witness the development of cryo-EM to the point where antibody-antigen interfaces can be resolved at high-resolution, thus solidifying the role of the technique in therapeutical research and development, there are, as yet, no single-particle EM studies detailing the structures of full antibodies. This is probably because Fab domains present less flexibility and are less prone to aggregation than whole antibodies (Chennamsetty et al., 2009; Li et al., 2016). Additionally, Fabs are also easier to purify and handle than are full antibodies. Where EM has been used to study the structures of whole antibodies (i.e. immunoglobulin G (Bongini et al., 2005; Sandin et al., 2004; Zhang et al., 2015) these have been carried out exploiting EM-tomography with results confirming an high level of flexibility of all fragments of the molecule, and it is argued that especially thanks to the movement the hinge, Fabs and Fc are less spatially restricted and may have a higher accessibility to ligands or receptors.

Given the academic and pharmaceutical interest in this area, the absence of high-resolution cryo-EM studies of antibody-antigen interactions within the whole-antibody context clearly needs to be addressed and methodologies developed to enable these. As will be seen below, this will require strategies for optimal sample vitrification as well as those which will limit the flexibility of the antibodies themselves.

Methods

4.1 Vitrification of CODV antibodies

4.1.1 *Apo*-CODV

After extensive trials to optimise the grid conditions (please refer to **Annex**), C-Flat Au-C (Protochips) grids (holey grids with gold support with carbon layer) were found to be the only one suitable to diminish aggregation and obtain good particle density and thinner ice for all the CODV complexes. Other grid types, with copper as the support material, were observed to introduce more aggregation and UltraFoil (Quantifoil) Au grids (gold support with gold layer) also didn't seem to be useful for good particle density. However, it was observed that C-flat Au-C grids, owing to their thin carbon foil and therefore fragile, needed to be glow discharged only for short time (30 seconds) and at lower currents (typically of 7mA). Glow discharging the grids at either longer or higher currents resulted in fewer intact grid squares, and therefore less areas for data acquisition. All glow discharging experiments were done using an easiGlow® glow discharge machine (Pelco) and vitrification was performed using Vitrobot Mark IV (Thermo Fisher Scientific). A total of three datasets (CODV1, CODV2 and CODV3) were collected for *apo*-CODV antibodies at different stages of grid optimisation (**Table 4.1**). For these three datasets, the vitrification was performed at 4°C under a humidity of 100%. The other vitrification details specific to each dataset is listed in the table below.

Dataset	Grid type	Sample volume (µl)	Concentration (µg/ml)	Glow Discharge time (current)	Blot Force / Blot Time (seconds)	Additives
CODV 1	CF 2/1 Au-C 300	3.5	300	40 sec (25 mA)	-2 / 3	1 mM DTT
CODV 2	CF 2/1 Au-C 300	3.5	250	40 sec (25 mA)	-2 / 3	0.67 mM DTT
CODV 3	CF 2/1 Au-C 300	4	175	30 sec (7 mA)	0 / 4.5	0.06 mM DDM

Table 4.1: Summary of the grid preparation for the three *apo*-CODV datasets collected during this work.

4.1.2 CODV-IL4 and CODV-IL4/IL13

Grid preparation and vitrification for cryo-EM data collections for CODV-IL4 and CODV-IL4/IL13 (**Table 4.2**) presented only small variations compared to that for CODV3 above. The most important of these variations was lowering the concentration of DDM to 0.03 mM, since 0.06 mM pushed particles too close to each other around the hole edges. Here again, the entirety of the screening process is recorded in the **Annex**.

Dataset	Grid type	Sample volume (µl)	Concentration (µg/ml)	Glow Discharge time (current)	Blot Force / Blot Time (seconds)	Additives
CODV-IL4	Au 300 CF 2/1	4	175	30 sec (7 mA)	0 / 4.5	0.03 mM DDM
CODV-IL4/IL13	Au 300 CF 2/1	4	150	30 sec (7 mA)	0 / 4	0.03 mM DDM

Table 4.2: Summary of the grid preparation for the CODV-IL4 and CODV-IL4/IL13 datasets collected during this work.

For graphene oxide coated grid preparation used in some CODV-IL4 trials, the protocol described by Martin et al. was followed (Martin et al., 2016). Here, a 2 mg/ml graphene-oxide solution (Sigma) was diluted 10-fold in distilled water and then centrifuged for 20 seconds at 300 x g in order to precipitate aggregates. A 3 µl drop of the solution was pipetted into freshly glow-discharged Au C-Flat 2/1 400 mesh grids and then incubated for 1 minute at room temperature. After 1 minute, excess liquid was blotted by using filter paper and the grid was washed 3 times with 20 µl drops of water (2 times face-down and 1 time face-up). Grids were then allowed to dry for at least 5 minutes before being used in the Vitrobot. Unlike with conventional grids, when using graphene-oxide grids the sample was applied from the back side (grid-bar side) of the grid, to prevent graphene-bound proteins from interacting with the filter paper during blotting (Palovcak et al., 2018).

4.1.3 CODV-IL13-Tralokinumab

For both tilted and untilted CODV-IL13-Tralokinumab triple complex datasets, grid preparation and vitrification followed similar processes and conditions as to those for CODV-IL4 and CODV-IL4/IL13 (**Table 4.3**). 3 µl of the sample at a 300 µg/ml concentration supplemented with 0.03 mM DDM were applied to an Au-CFlat 1.2/1.3 grid and vitrified after blotting for 7 seconds with a blot force of 2. Glow discharging time was reduced to 20 seconds as it was noted this did not compromise support hydrophilicity and grids were less likely to break.

Dataset	Grid	Sample volume (µl)	Concentration (µg/ml)	Glow Discharge time (current)	Blot Force / Blot Time	Additives
TC	Au 300 CF 1.2/1.3	4	300	20 sec (7 mA)	2 / 7	0.03 mM DDM

Table 4.3: Summary of the grid preparation for the CODV-IL13-Tralokinumab triple complex dataset collected during this work.

4.2 Cryo-EM data collection

Part of the early screening for vitrification conditions was performed on a 200 keV LaB_6 Tecnai G20 (Thermo Fisher Scientific) paired with a 2.7k by 2.7k Gatan Orius SC600 CCD camera (AMTEK), at Sanofi Pasteur (Marcy l'Étoile, France), where micrographs were acquired using Digital Micrograph software (Gatan) at x29000 magnification (pixel size 2.22 Å).

Procurement of a 200keV Glacios microscope equipped with both Falcon II detector (Thermo Fisher Scientific) and a Gatan K2 detector (AMTEK) at the IBS EM platform, facilitated the majority of screening sessions for vitrification conditions.

When grids with acceptable particle distribution and ice thickness were found, in some cases, small datasets (**Table 4.4, Table 4.5**) were collected on the IBS Glacios microscope (Tilted CODV-IL4 and untilted TC test datasets). All high-resolution data collections were performed on the ESRF CM01 beamline (Kandiah et al., 2019) using a 300 keV Titan Krios Microscope (Thermo Fisher Scientific) equipped with a 4k x 4k Gatan K2 Summit direct electron detector (AMTEK) and a Gatan Bioquantum LS/967 energy filter. On both Glacios and Krios microscopes, EPU software EPU software (Thermo Fisher Scientific) was used for automatic image acquisition. For the TC data collection at the IBS Glacios, a K2 detector was used instead of the Falcon II camera. In this case SerialEM (Mastronarde, 2018) was used as an image acquisition software.

The first dataset for *apo*-CODV (CODV1 in **Table 4.4**, which contains collection parameters for all untilted datasets) comprised 660 movies (before curation during image processing) and was collected using a Volta phase plate (Danev & Baumeister, 2016) and applying a small defocus range of -0.5 to -1.0 µm, with a total dose of 46 $e^-/Å^2$ fractionated over 40 frames in super-resolution mode. The magnification used was x130000 yielding a pixel size of 0.53 Å.

To increase the contrast without resorting to the use of the phase-plate, the dataset CODV2 (654 movies) was collected with a defocus range of -1.0 to -3.0 µm, objective aperture of 70 µm and a higher dose of 60 e^-/Å^2 over 40 frames. Counting mode (pixel size of 1.067 Å) at x130000 magnification was used for this dataset.

With an improved grid preparation, a CODV3 dataset with 2444 raw movies was acquired with a defocus range of -1.5 to -3.5 µm, objective aperture of 70 µm and a dose of 46 e^-/Å^2 over 40 frames. The pixel size was 0.83 Å (counting mode, x165000 magnification).

Dataset	Microscope (detector)	Defocus range (µm)	Objective aperture (µm)	Magnification (pixel size, Å)	Number of movies	Total Dose (e^-/Å^2)
CODV 1	Krios (K2)	-0.5 to -1.0	NA	130000	660	46
CODV 2	Krios (K2)	-1.0 to -3.0	70	130000	654	60
CODV 3	Krios (K2)	-1.5 to -3.5	70	165000	2444	46
CODV-IL4	Krios (K2)	-1.5 to -3.5	100	165000	7044	60
CODV-IL4/IL13	Krios (K2)	-1.5 to -3.5	100	130000	2919	60
Triple complex	Krios (K2)	-1.2 to -3.0	100	165000	14010	46

Table 4.4: Summary of the parameters used in the collection of 'untilted' datasets analysed during this work.

For the antibody-antigen complexes, the CODV-IL4 dataset collected (7044 movies) had defocus ranges of -1.5 to -3.5 µm, objective aperture of 100 µm and a total dose of ~60 e^-/Å^2. The movies had a pixel size of 0.827 Å. The CODV-IL4/IL13 dataset (2919 movies) was collected with identical settings but at one magnification lower (pixel size 1.053 Å).

For CODV-IL13-Tralokinumab untilted datasets (14010 movies in total) were collected in two sessions and later merged together as the settings were identical and both were collected from the same grid. The magnification was 165000x (pixel size: 0.83 Å) with a dose of 46 e^-/Å^2 over 40 frames. The defocus values used ranged between -1.2 and -3.0 µm.

From 2D and 3D class averages of both *apo*-CODV and its antigen-complex datasets, it was observed that there was a preferred orientation problem (refer to **Results**). To overcome this, tilted dataset collections (**Table 4.5**) were attempted for both CODV-IL4 and CODV-IL13-Tralokinumab. The CODV-IL4 tilted dataset (2571 movies) collection at the ESRF Krios was performed with a -30° stage tilt and 2 exposures per hole along the tilt-axis. Unlike the previous datasets, the zero-loss energy filter was set to 10 eV instead of 20 eV to avoid the plasmon peak that is shifted when tilting the stage. 40 frame movies were fractionated throughout 10 second exposures. For CODV-IL13-Tralokinumab the tilted dataset comprised (1188 movies), tilted data collection at 40° was set-up with a 52 $e^-/Å^2$ total dose over 40 frames.

Dataset	Defocus range (µm)	Objective Aperture (µm)	Tilt	Magnification (pixel size, Å)	Number of movies	Total Dose ($e^-/Å^2$)
CODV-IL4	-1.5 to -3.0	100	30°	165000 (0.827)	2571	44
Triple complex	-1.5 to -2.5	100	40°	165000 (0.827)	1188	52

Table 4.5: Summary of the parameters used in the collection of 'tilted' datasets analysed during this work.

4.3 Cryo-EM image processing

4.3.1 Dataset pre-processing and EM map acquisitions

CODV1, CODV2 and CODV3 were processed, wherever appropriate, with four different data processing packages: RELION 2.1 and RELION 3.0 (Zivanov et al., 2018), cisTEM (Grant et al., 2018) and Xmipp 3.0 (de la Rosa-Trevín et al., 2013). Preprocessing was attempted using both Unblur (Grant & Grigorieff, 2015) and MotionCor2 (Zheng et al., 2017) for motion correction and dose weighting of movies, and CTFFind 4.1.8 (Rohou & Grigorieff, 2015) or GCTF (Zhang, 2016) for CTF and phase shift estimation. Particle picking was carried out as implemented within the processing programs or using Gautomatch (Zhang, 2018). EM density maps obtained were visualized with UCSF Chimera (Pettersen et al., 2004) and published structures of CODV-Fab$_{IL4 \times IL13}$ (PDB code: 5HCG; Steinmetz et al., 2016) and the knob in hole IgG-Fc (PDB code: 4NQS; Elliott et al., 2014) were used for docking.

The datasets for CODV-IL4, CODV-IL4/IL-13 and CODV-IL13-Tralokinumab were also mostly processed within the cryoSPARC 2 (Punjani et al., 2017) environment. However, for certain steps RELION 3.0 and 3.1, EMAN2 (Tang et al., 2007) or command-line GCTF (Zhang, 2016) were also used.

In all cases, EM surfaces and projections from PDB files were performed using *molmap* (UCSF Chimera) and EMAN2, while general image manipulation was done with the *relion_image_handler* command and the Bsoft program (Heymann, 2001).

All the required inter- and intra-program file and format manipulations were performed with self-written *python*, *sh* and *tcsh* scripts or with the *UCSF pyem* package by Daniel Asarnow (Asarnow et al., 2019).

4.3.2 EM map refinement and fitting

Per-particle CTF refinement and Bayesian polishing were performed within Relion 3.1. The global resolution of the final map was estimated according to the gold standard Fourier shell correlation (GS-FSC) with a cutoff of 0.143 (Rosenthal & Henderson, 2003). Local resolution variability was estimated using ResMap (Kucukelbir et al., 2014a), with half-maps as input volumes.

Models for fitting and refinement were obtained by homology modelling using SWISS-MODEL (Waterhouse et al., 2018), based on NCBI *BlastP* (Johnson et al., 2008) alignment between our sequences and the already published individual PDB structures of Tralokinumab-IL13 (Popovic et al., 2017; PDB code: 5L6Y) and CODV-Fab (PDB code: 5HCG; Steinmetz et al., 2016). For further map refinement and rigid and flexible fitting, the *CCPEM* (Wood et al., 2015) and *Phenix* (Adams et al., 2010) packages were used, specifically *Real Space Refine* and *Autosharpen* within *Phenix*; and *MRC to MTZ* conversion and *LocScale* (Jakobi et al., 2017b) in *CCPEM*. Model building and validation was performed in *Coot 0.9.2* (Emsley & Cowtan, 2004) and *Molprobity* (C. J. Williams et al., 2018) respectively.

Results

4.4 Design of a cryo-EM pipeline for multispecific antibodies

4.4.1 Screening of vitrification conditions for CODV

An exhaustive list of all vitrification conditions tested can be consulted at the **Annex**. Because there was no literature regarding the vitrification of full antibodies, the screening process started with well-established settings used on the preparation of grids for test samples (Kandiah et al., 2019). Initial conditions included Cu-Quantifoil 1.2/1.3 grids, a standard DPBS pH 7.4 buffer and an antibody concentration (150 µg/ml) ~20 times that used in NS-EM trials, which is generally a good rule of thumb to set an initial value when switching from negative-stain to cryo-EM (Thompson et al., 2016). During this initial stage, particles could not be observed in the holes due to high carbon affinity, non-optimal ice thickness or a too low sample concentration, therefore in subsequent trials, many different settings exploring different aspects of the grid preparation process were surveyed.

In brief, different grids and support materials including Quantifoil and Lacey (EM Sciences) grids were tried. Several support hole (1.2/1.3, 2/1 or 2/2 µm) and grid mesh sizes (300 and 400 squares/inch) were also tested. Sample volume of 3.5 µl was kept constant for these early trials, however sample concentrations explored ranged from 150 to 1290 µg/ml. Glow discharging settings and blotting time were also changed as means to achieve an ice thickness that allowed visualization of the sample under the electron beam.

Initial screening of conditions for the imaging of *apo*-CODV was carried out using a Tecnai G-20 microscope at Sanofi Pasteur (**Figure 4.1A**). 300-mesh copper grids with Quantifoil® 2/1 were used, along with a 90 second plasma cleaning step. *Apo*-CODV in PBS at 1290 µg/ml with a volume of 3.5 µl was applied and the blotting settings were as follows: blot force of -8; blot time of 2 seconds; wait time of 10 seconds. However, *apo*-CODV was found to be completely aggregated and seemed to have a preference for the foil.

Numerous parameters were changed in the following attempts: the buffer in which the sample was contained was changed from PBS to HEPES (PBS is not frequently used in cryo-EM due to its low performance at cold temperatures); the concentration of *apo*-CODV was gradually lowered from 1290 µg/ml; new supports, namely SiO_2, and 2 nm continuous carbon coated grids, were used; wait times during blotting was also reduced to 0 seconds, because even if this setting were to allow for proteins to disperse into the holes, it may also expose the proteins towards the highly-denaturing and aggregating air-water interface for a longer time (Glaeser, 2018).

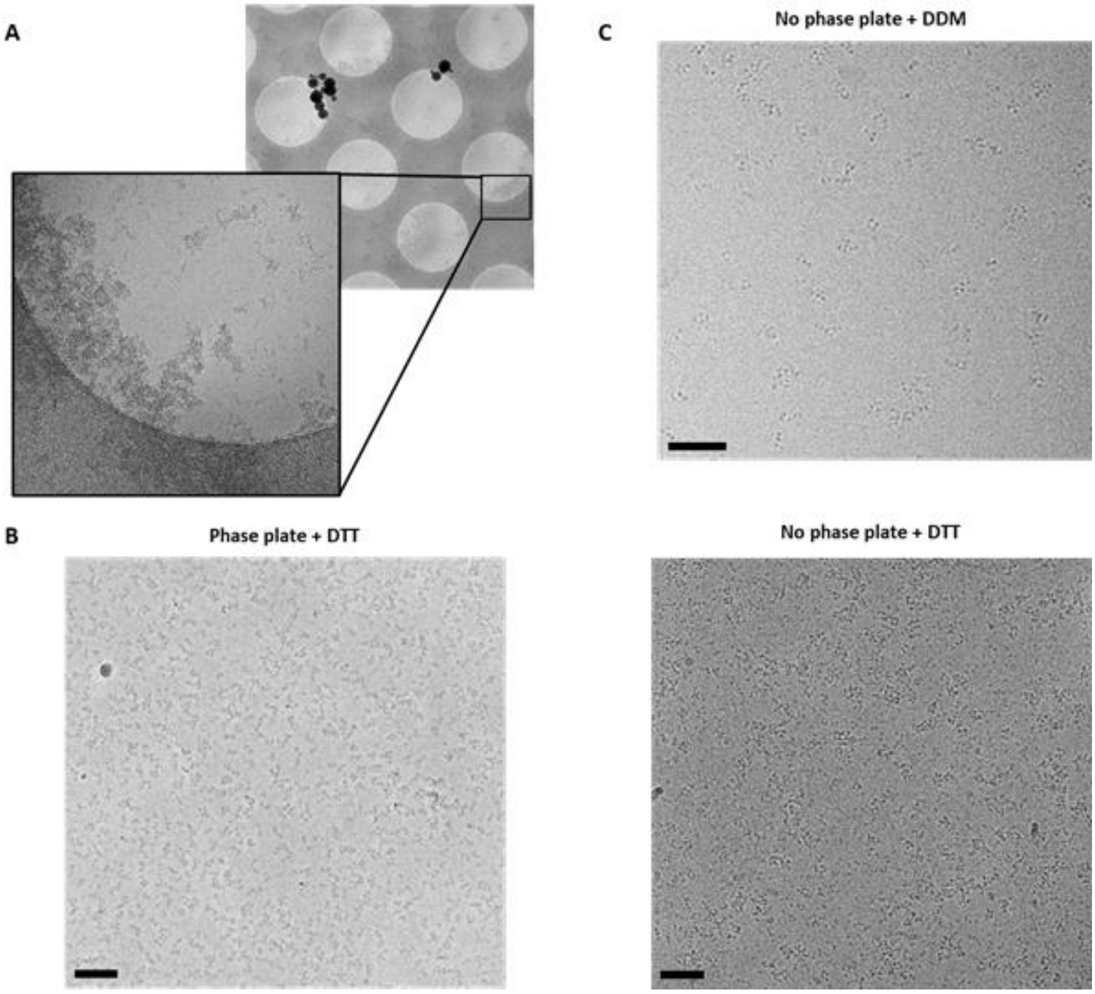

Figure 4.1: Cryo-EM screening and data collection for *apo*-CODV. (A) Representative micrograph of the on-grid aggregation observed during the initial screening stage. Zoomed magnification: 29000x. **(B)** Comparison of *apo*-CODV + DTT micrographs acquired with phase plate (Left, CODV1) in super-resolution mode (0.53 Å/pix) and without phase plate (Right, CODV2) in counting mode (1.067 Å/pix). The contrast is higher and the image is smoother for CODV1. **(C)** Representative micrograph from the CODV + DDM (CODV3) dataset. Here particles are well-dispersed and easily identifiable. See **Table 4.1** for full details. In all images, the scale bar is 500 Å.

Unfortunately, none of these strategies proved successful in solving the two issues presented. DTT was then considered as an additive to the HEPES buffer, as low concentrations of the molecule are known to prevent protein oxidation and unwanted disulphide bonds while preserving protein activity (Cleland, 1964). Grids were also changed to Au-C C-Flat, which has a gold support and a carbon foil. Adding 1mM DTT to the buffer and using Au-C C-Flat 2/1 grids allowed *apo*-CODV to distribute into in the grid holes so a grid prepared using these conditions was used for the collection of dataset CODV1 (0.3 mg/ml and 1 mM DTT) at the ESRF Titan Krios (**Figure 4.1B**, see **Table4.1**, **Table 4.4** for full details). Collection of this dataset also exploited the use of the Volta phase plate, which allowed to see the particles with good contrast. As can be seen in **Figure 4.1B**, even though particle density and identification were acceptable, they were still not uniformly present over the grid.

To try to improve this, grids were prepared with 0.25 mg/ml *apo*-CODV and 0.67 mM DTT and following vitrification a cryo-EM dataset (CODV2; **Table 4.1**, **Table 4.4**) was collected on the ESRF Titan Krios. Here, and because the use of phase plates had proven difficult for dataset CODV1, a conventional data collection protocol which included and using a smaller objective aperture (70 µm), higher electron dose and far-from-focus values in order to introduce sufficient contrast was adopted. Unfortunately, however, the particle distribution and ice thickness were similar to those observed for CODV1 (**Figure 4.1B, right**).

While 1mM DTT is safer to use for antibodies that contains several disulphide bonds, its use perhaps is still not optimal as it might still damage the disulphide bonds, leading to new conformational changes and as it is behind the scope of this project to characterise the effect of DTT concentration on the structural integrity of antibodies, we decided to not to use DTT. Alternative conditions were thus screened in attempts to reduce sample aggregation. Grids containing gold UltrAuFoil grids (gold grids, gold support) were used in trials, but this proved unsuccessful. Based on a Fab-based study of Oyen *et. al.* (Oyen et al., 2018) , a breakthrough in optimal grid preparation appeared when using the increased concentrations of the non-ionic detergent n-dodecyl β-d maltopyranoside (DDM) as a surfactant (see **Annex** for full details). Here, the addition of 0.06 mM DDM, along with new blotting settings improved ice thickness and particle dispersion (**Figure 4.1C**) and a full dataset (CODV3, see **Table 4.1**, **Table 4.4** for full details) was collected at the ESRF Titan Krios. In the micrographs obtained CODV could directly be identified in its full antibody form and particles, while rather scarce, had a distribution suitable for manual particle picking.

It should be noted here that, in addition to the relatively simple expedient of using DDM as a buffer additive, a very wide screening of conditions to improve cryo-EM grid vitrification for *apo*-CODV and its complexes with antigens was also carried out. Full details of these can be found in the Annex. Regarding alternative detergents, NP-40 and CHAPS were tried. Sugars were also considered as additives, since old studies (De Carlo et al., 1999) had hinted at possible cryoprotectant properties of compounds such as trehalose. There was no improvement in any of these cases when comparing with the DDM-based protocol used for *apo*-CODV above.

At an intermediate stage of optimization, we concluded that full antibodies suffer from denaturation due to the air-water interface, resulting in heavy aggregation (**Figures 4.1A, B**). In order to explore an alternate to surfactants, the use of stable substrates such as graphene oxide was tried out to reduce the denaturation effect on *apo*-CODV from air-water interface (Palovcak et al., 2018) and hence good particle density with different orientations. However, graphene-grids prepared in-house have a graphene coverage of only 10%, very likely due to its intricate preparation or the absence of plasma cleaning treatment as suggested in (Russo & Passmore, 2014). In the areas of these grids covered with graphene, the antibodies could be discerned. However, particle distribution resembled that seen in DDM-based experiment conditions and not better.

Finally, different buffer conditions were also screened (see **Annex**). Mildly acidic buffers such as citrate and sodium acetate were previously reported very useful for antibody work with ligands (Lee et al., 2013). However, for *apo*-CODV and its complexes with antigens these caused aggregation and denaturation during grid preparation, evidence supported by nanoDSF experiments (section **2.8** of the **Purification and characterization** chapter). When *apo*-CODV was in either succinic or malic acid buffers, buffers suggested to be slightly better for *apo*-CODV stability according to nanoDSF results, grid quality was similar to that seen when using Tris Buffered Saline (TBS), the purification and control buffer. It has thus not yet been possible to establish a clear relationship between thermostability and vitrification stability.

To summarise, despite extensive screening, the best condition for *apo*-CODV grid preparation clearly depended on the use of DDM as a buffer additive. These resulted in the collection of the dataset CODV3 (**Table 4.1, Figure 4.1**). Moreover, similar vitrification parameters were also found to be suitable for the cryo-EM analysis of CODV-IL4, CODV-IL4/IL13 and CODV-IL13-Tralokinumab. It should be noted though, that in DDM-based grid screenings (hole sizes of 2 µm), good particle distribution of *apo*-CODV and its complexes with antigens only occurs in thicker ice. While this distribution is acceptable, it inherently translates into a slight loss of high-resolution information. In grids with thinner ice, particles tend to aggregate at the center of the foil holes due to the higher propensity to being in the air-water interface while the edges contain only a few discrete particles. C-Flat grids with smaller hole sizes (1.2 µm) helped to a certain extent to obtain uniform thinner ice in the foil hole with good particle distribution also at the centre, enabling imaging at the centre of the foilholes.

4.4.2 cryo-EM image processing workflow for CODV datasets

4.4.2.1 Processing of CODV datasets

4.4.2.1.1 Datasets CODV1 and CODV2

For the dataset CODV1, CTF estimation was done using GCTF, and only micrographs with good CTF fit were included for further image analysis. Close particle proximity made the manual picking very difficult but, nevertheless, 903 particles were manually picked and 2D classification carried out. These classes were used as templates for auto-picking in RELION 2.1, with a 30 Å low-pass filter. 438000 particles were auto-picked and after few rounds of cleaning bad classes, 156251 particles were chosen and further classified into 20 classes.

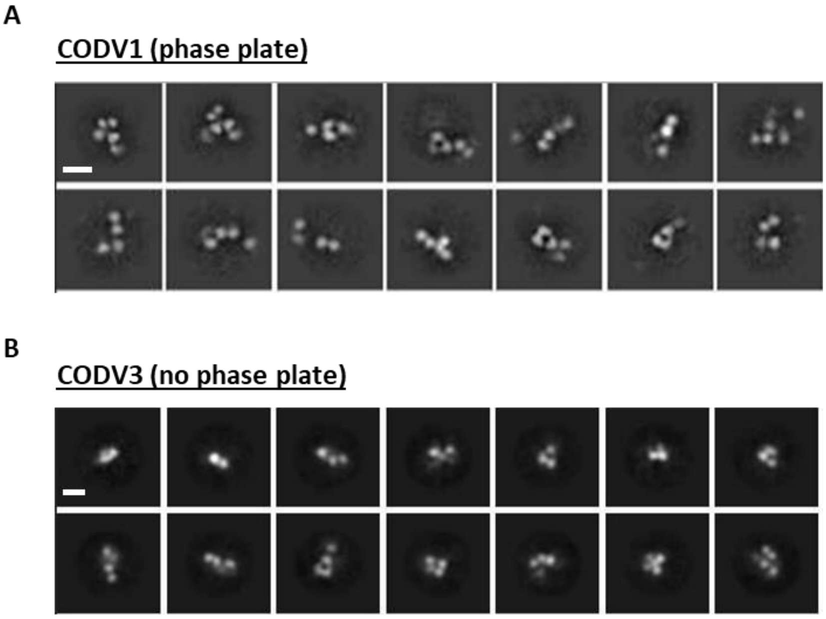

Figure 4.2: 2D classification output of CODV with and without phase plate. Representative 2D classes of CODV with **(A)** and without phase plate (but with DDM) **(B)** in cryoSPARC evidence the struggles of auto-picking multidomain antibodies that are close to each other. Additionally, classes that might suggest a full antibody (class 2 of figure A) cannot be correctly centered. Scale bar is 100 Å in both images.

The classes obtained proved more divergent compared to the 2D projections of an antibody. Some classes showed one or two domains, while other showed three, sometimes not connected to each other, again evidencing the difficulties in picking and 2D classification. Other particle-picking capable software, namely cisTEM (Grant et al., 2018), Xmipp3 (de la Rosa-Trevín et al., 2013) (within Scipion (de la Rosa-Trevín et al., 2016)) and Gautomatch (Zhang, 2018) which use different picking algorithms were tried out and thus particles picked were further classified using RELION and cisTEM. However, none of these programs produced good 2D classes therefore work on the dataset was stopped. Later in the project the dataset was revisited on cryoSPARC, but the classes obtained were similar to those in RELION (**Figure 4.2A**).

Because the phase plate dataset, CODV1, seemed difficult to work with in image processing even at the 2D step, a second dataset (CODV2) was collected without phase plate. However, it was also difficult to perform automatic picking and hence 2D classification on this dataset too. Minor particle aggregation observed in these two cases could be the reason.

4.4.2.1.2 Dataset CODV3

The presence of DDM helped considerably to reduce the aggregation and individual particles were discernible in the micrographs. However, the grids from this batch of vitrification seem to have empty holes along with ice-filled holes in the same grid square. In spite of careful selection during setup of data collection, the dataset contained micrographs with empty holes as well as micrographs with huge drift owing to very thin ice. Therefore, the CODV3 dataset was thoroughly screened for good micrographs prior to performing any picking.

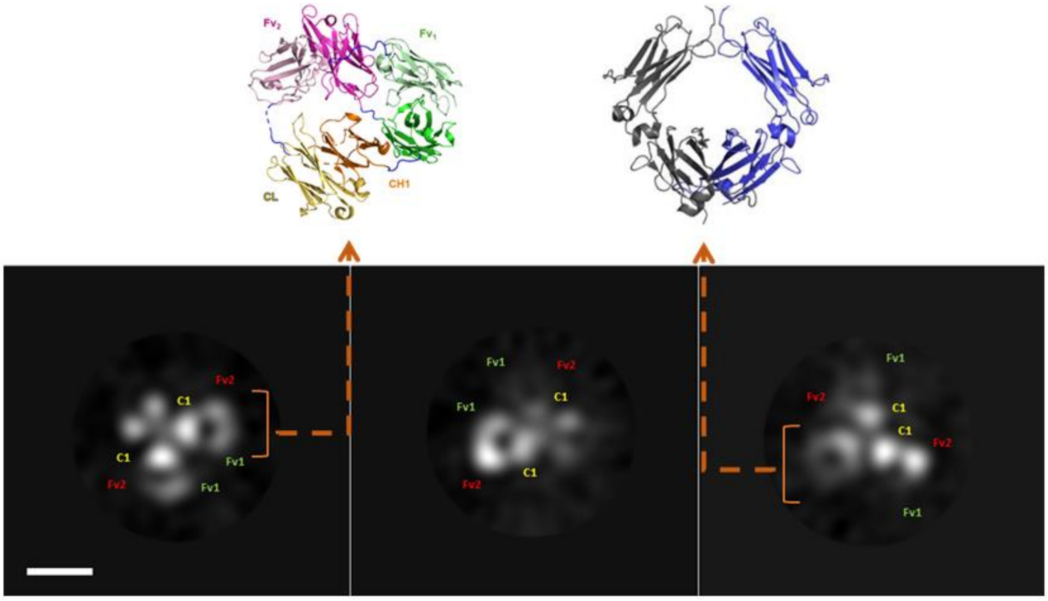

Figure 4.3: Representative 2D classes obtained after manual picking of the CODV3 dataset in RELION. As was also noted in the classes obtained in NS-EM, CODV exhibits a triangular structure with three domains. By measuring the distance between these domains, corresponding to the linker lengths, Fv1 (green), Fv2 (red) and C1 (yellow) could be clearly identified. In some cases, the hollow rhomboid-like structure of the IgG-Fc domain, which has been provided for visual comparison (PDB entry: 4J4P), (orange), can also be distinguished. Scale bar = 100 Å.

This curation resulted in a dataset containing 1408 micrographs, from which a subset of 100 higher-defocus range micrographs was chosen for manual picking of particles. The presence of clearly identifiable full-length *apo*-CODV molecules allowed for manual picking of 2000 particles from the subset and particle extraction was performed using a box size of 400 pixels and a binning factor or 2 (new box size: 200 pix, new pixel size: 1.66 Å). The successful early 2D classifications **(Figure 4.3)** used a T value of 1, resolution limit (E-step) of 20 Å and was finely sampled for higher accuracy in rotations and alignments (1 degree of angular sampling and a 10-pixel offset search range).

The 2D classes obtained after manual picking showed, for the first time, a full *apo*-CODV antibody as imaged by cryo-electron microscopy. Despite low resolution and an average of about 250 particles per class, some features of the antibody were easily recognizable. For example, the triangular-shaped Fabs could be identified, formed by 3 globular shapes (C1, Fv1 and Fv2), and in some views (class 3 in **Figure 4.3)**, the hollow rhomboid shape of the Fc region could also be identified. From this small manually picked particle set, CODV appeared to be very flexible at the inter-domain level, with a rotation axis around the area corresponding to the hinge.

Unfortunately, using the 2D classes obtained as templates for auto-picking was still not sufficient for accurate picking by RELION and it was not possible to proceed to the 3D step.

4.4.2.2 cryo-EM processing of CODV complexes

4.4.2.2.1 *CODV*-IL4

The first untilted dataset of CODV-IL4 (**Table 4.4**) was collected as an attempt to partially stabilize CODV by adding a very high-affinity ligand to the antibody. However, as observed for *apo*-CODV above, RELION 3.0 -based processing of this dataset did not yield useful results. A newly released software named cryoSPARC2 (Punjani et al., 2017) was therefore considered as an alternative processing program. Here, CTF estimation on 7044 aligned movies was carried out using the program GCTF. After manual inspection to eliminate clearly unsuitable data, such as drifted, contaminated and broken images, these were curated into 6016 micrographs (**Figure 4.4A**) using the slider-based *curate exposures* job of the cryoSPARC pipeline. We initially discarded micrographs with higher than 500 Å astigmatism, lower than 5 Å CTF resolution fits and outlier defocus in order to change CTF estimation parameters and check for improvement. Images that improved within the established limits were re-added to the set. After manually picking 2038 particles, 2D classification was performed in cryoSPARC2. While the classes obtained were blurry, densities for the Fab regions could be very well discerned. These classes were then used as templates for particle picking in a two-stage process. In this protocol a subset of high-defocus 100 micrographs was used first used to generate better templates. Those templates with higher SNR were then used to pick particles in the entire dataset.

Picked particles were carefully inspected by varying the normalized cross correlation (NCC) and power score (PC) parameters in cryoSPARC2. NCC indicates the agreement of the particle with the template and PC indicates the presence of strong signal.

About 320000 particles were chosen and extracted as 2X binned particles with a box size of 200 pixels.

When performing averaging, the recentring of 2D classes was turned off in order to minimize the centre-of-mass (COM) bias caused by the Fab density. Conversely, maximization by poses and shifts was turned on as this yields better 2D results with noisy data. Maximizing means that, weighted by their probability, the algorithm directly considers the most probable orientation and shift of each particle for each class as a way to balance the alignment uncertainty. Using these settings, for the first time not only the different regions of CODV antibody were visible but also the alignment at the Fab level was optimal and as a result secondary structure features could be identified in the most populated classes. Further cleaning steps were performed to eliminate particles with domains missing, resulting in 250000 particles whose most representative classes are shown in **Figure 4.4B**.

Different conclusions could be drawn from these 2D averages. Firstly, Fc appears to be very flexible, leading to “ghost” or blurred density for this region. Secondly, there is a very high conformational heterogeneity within the same view across the dataset. Including more classes leads to multiple, almost identical, averages while using very few ends up blurring them and losing resolution. Thirdly, there seemed to be preferential orientation of the particles, as only three clearly different views could initially be discerned.

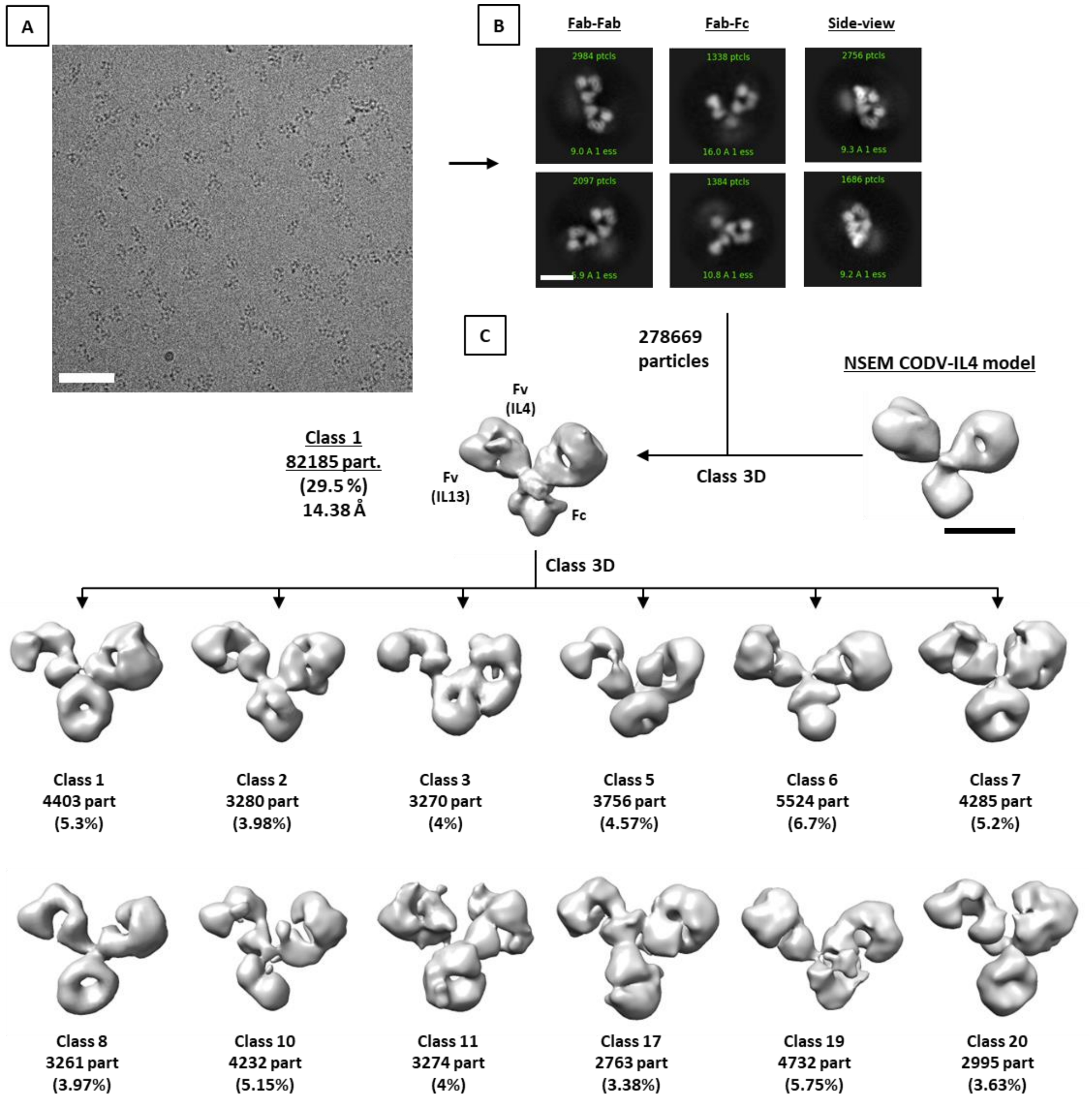

Figure 4.4: Cryo-EM analysis of CODV-IL4. (A) Representative micrograph of the CODV-IL4 dataset (scale bar = 500 Å. **(B)** 2D classes obtained for the untilted dataset could be divided into three views: A Fab-Fab view with blurred Fc, a Fab-Fc view with a blurred second Fab and one side-view of the Fab-Fab. **(C)** 3D classification process of whole-antibody CODV-IL4, with 4x binned tilted+untilted particles and the NS-EM map of CODV-IL4 as template. All classes were aligned keeping one Fab static. A large flexibility of Fc is very apparent, but population is low for each conformation. Unfortunately, no density corresponding to IL4 could be observed. Scale bar is 100 Å in both 2D and 3D images.

Ab-initio attempts to obtain a 3D initial model for the full antibody in RELION, cryoSPARC2 and cisTEM with different parameters were not successful. Owing to the high flexibility in Fc region reflected in the 2D class averages, at best only a 2-Fab reconstruction could be obtained, which seemed to have much more density than to accommodate a Fab moiety (**Figure 4.4B**). A plausible reason is the lack of accurate angular assignments mostly due to the inherent low SNR and the inherent flexibility of the molecule.

A common tactic (Rosenthal & Henderson, 2003) to observe different views is to collect a dataset with the microscope stage tilted to certain degrees (usually 20-40^o). Following this, a tilted dataset (**Table 4.5**) was collected at 165000x magnification (0.827 Å/pix) and a tilt angle of 30^o, from which 2408 micrographs were processed after individually curating each image.

Due to tilting, particles are at different defocus values in a single micrograph. To account for this, per-particle CTF estimation was attempted, with the *Multi Patch CTF* feature in cryoSPARC, yielding locally-variable CTF fits with resolutions averaging 4.5 to 5 Å. Unfortunately, the resolution of the resulting 2D classes (125000 particles picked) was very low and no secondary structure features could be discerned. In comparison to the 2D classes from untilted dataset, very few and rare classes with new views were identified. Nevertheless, the very prevalent Fab-Fab view from the untilted data was less predominant in the tilted dataset. In spite of these slight improvements in views, 3D *ab-initio* attempts for the tilted dataset also were not successful, probably due again to the flexibility of Fc. Due to the fact that the NS-EM CODV-IL4 dataset (section **3.5.1** of the **NS-EM chapter**) had yielded several very low-resolution three-domain volumes, we wanted to exploit the 3D volume from NS-EM as a starting model for cryo-3D classification steps. For this, cleaned 4x binned (3.3 Å/pixel) particles were exported from cryoSPARC 2.5 to RELION 3.0 and rescaled versions of a NS-EM volume that more clearly showed three densities at low resolution were used for 3D classification of the particles.

The successful 3D classifications required, most notably, a high number of classes (K = 25) and a high T (T = 10) value to yield several 3D maps showing density for all 3 CODV regions. (**Figure 4.4C**). The high number of classes was aimed at tackling large movements in the molecule and a high T value was used to cluster small conformational changes in particles corresponding to the same view into the same classes. The results from these classifications showed the three clear fragments for the first time in cryo-EM. As can be seen, Fc was observed in many different conformations, confirming the high degree of flexibility due to the hinge. However, the movements of this antibody region seem to be independent from the conformation of the Fabs. On the other hand, the movement of the Fabs seemed to be more restricted in comparison to Fc. Due to the flexible nature of CODV and small population of particles in each class (an average of 3000 particles) the resolutions of the classes obtained is between 15 and 20 Å. Besides, classes with densities for all three domains were obtained only with 4X binned data and unbinned data failed to produce a full Fc. It is to be noted that binned images have more SNR but low resolution compared to unbinned images.

To aim for higher resolutions of these classes, the number of particles required would probably need to be at least an order of magnitude higher than what was available. Even including the tilted dataset only allowed us to less than duplicate the number of particles and did not lead to resolution gains. This approach seemed to be too costly both time and budget wise to be worth pursuing.

Another conclusion drawn from the analysis described above is that, consistent with what was observed in NS-EM experiments (section **3.5** of the **NS-EM** chapter), IL4 did not seem to be present in the reconstructions obtained despite a plethora of biochemical evidence suggesting the sample analysed is CODV-IL4. As the cryo-EM visualisation of the antibody-antigen interface within the full-antibody context was one of the main goals of the project, we decided to pursue what we have called a *Fab-focused processing pipeline* in the hope that this would at least show evidence of IL4 in cryo-EM reconstructions.

In this strategy, we took advantage of the centre-of-mass bias in 2D alignment by the Fabs. A very tight mask of 120 Å, only slightly larger than the diameter of an individual CODV Fab domain, was applied to the particles during 2D classification. As expected, some of the classes showed the Fab density at the centre. These templates were then used to repick the entire dataset, effectively doubling the number of clean initial particles available (379000), as each antibody contain 2 Fabs. 2D classification showed new orientations of the fragments (**Figure 4.5A**), as their alignment was not limited by the rest of the antibody. 3D *ab-Initio* model generation by Stochastic Gradient Descent (SGD) and 3D classification also worked better and softer classification constraints (K = 10, T = 4) were required to generate a good set of classes (**Figure 4.5B**). However, even at the Fab level, intra-domain flexibility was very apparent. While glycine linkers connecting C1, Fv1 and Fv do constrain some movements, the fragments did seem to still move a large degree relative to each other 3D classes close in conformation were combined and refined until the estimated resolution improved. Following this procedure, 3D reconstructions with an estimated resolution between 10 and 12 Å were obtained, where each domain of the Fab was clearly identifiable (**Figure 4.5C**).

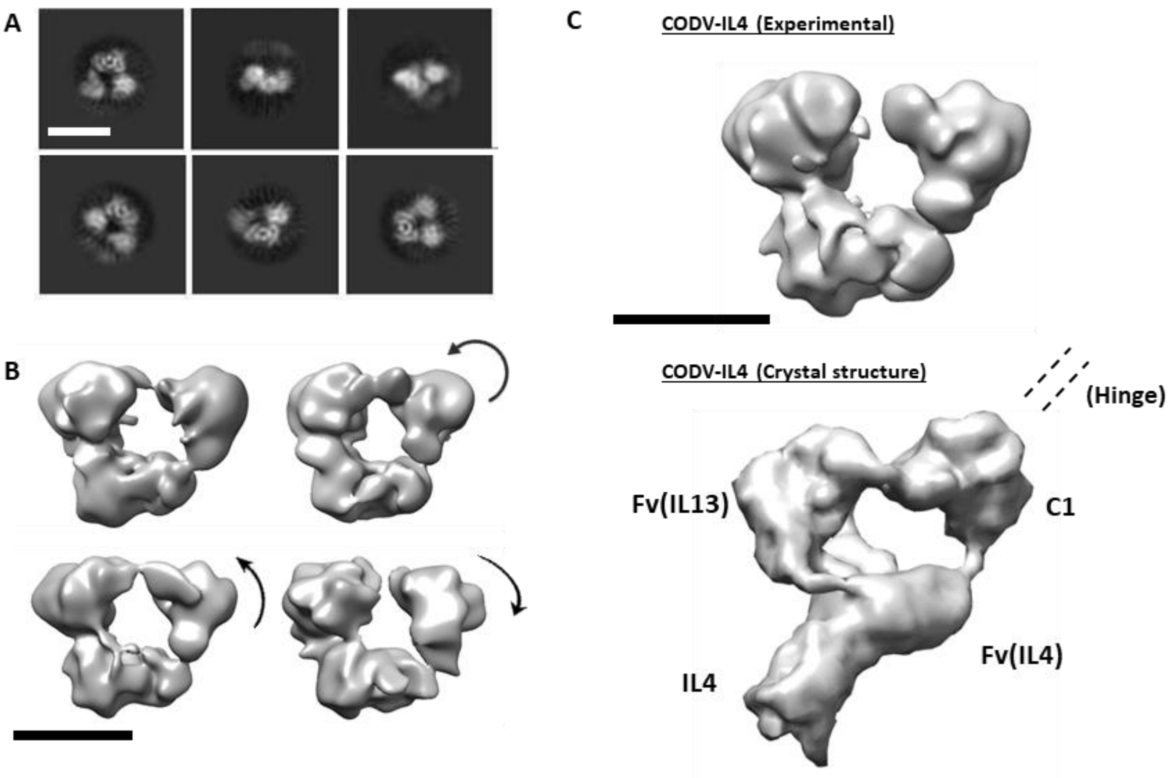

Figure 4.5: Fab-Focused processing of CODV-IL4. (A) Representative 2D classes obtained when using a tight mask and a small extraction box. At least three different views can be discerned. **(B)** 3D classification outputs of the Fab-IL4 particle set reveals flexibility within the Fab. The anti-IL4 Fv (bottom) is kept static so movements of the other domains are more easily identified. **(C)** Comparison between a Refine3D map from our data (top) and a 10 Å low-passed surface obtained from the crystal structure (5FHX) at the same volume threshold. There is no evidence for IL4 density in the cryo-EM reconstruction. Note that the Fab domain are rotated compared to the PDB. Scale bar in all images = 50 Å.

It is very noteworthy, though, that while this protocol improved alignment issues, in no step of the Fab-focused pipeline was it possible to identify any signal or density corresponding to IL4. With the number of Fab particles and orientations processed, even if the occupancy was not 100%, there should have been at least a partial signal of IL4 at Fv_1 (**Figure 4.5C**). This was however not the case.

4.4.2.2.2 CODV-IL4/IL13

CODV-IL4/IL13 behaved very well under DDM-based vitrification (**Table 4.4**) and 2919 movies were collected at a magnification of 130000x, used to increase the field of view to have more particles per micrograph (**Figure 4.6A**). From this dataset a total of 2731 valid micrographs were curated. After manual picking of 5000 particles in cryoSPARC2, micrographs were template picked, which resulted in 200000 particles (box size of 280 Å) after the first cleaning steps.

2D classifications of these particles with high number of classes showed similar results to those for CODV-IL4. However, and as was also the case for CODV-IL4, none of the 2D classes showed any clear evidence of density corresponding to IL4 or IL13 even though SDS-PAGE analysis clearly showed the presence of both in the sample (see **Figure 2.2** in the **purification and characterization** chapter). The 2D classes (**Figure 4.6B**) also seemed to show very strong preferential orientation, with only one view of the molecule, mainly a Fab-Fab view in multiple different conformations due to flexibility with a very faint signal in the parts corresponding to Fc.

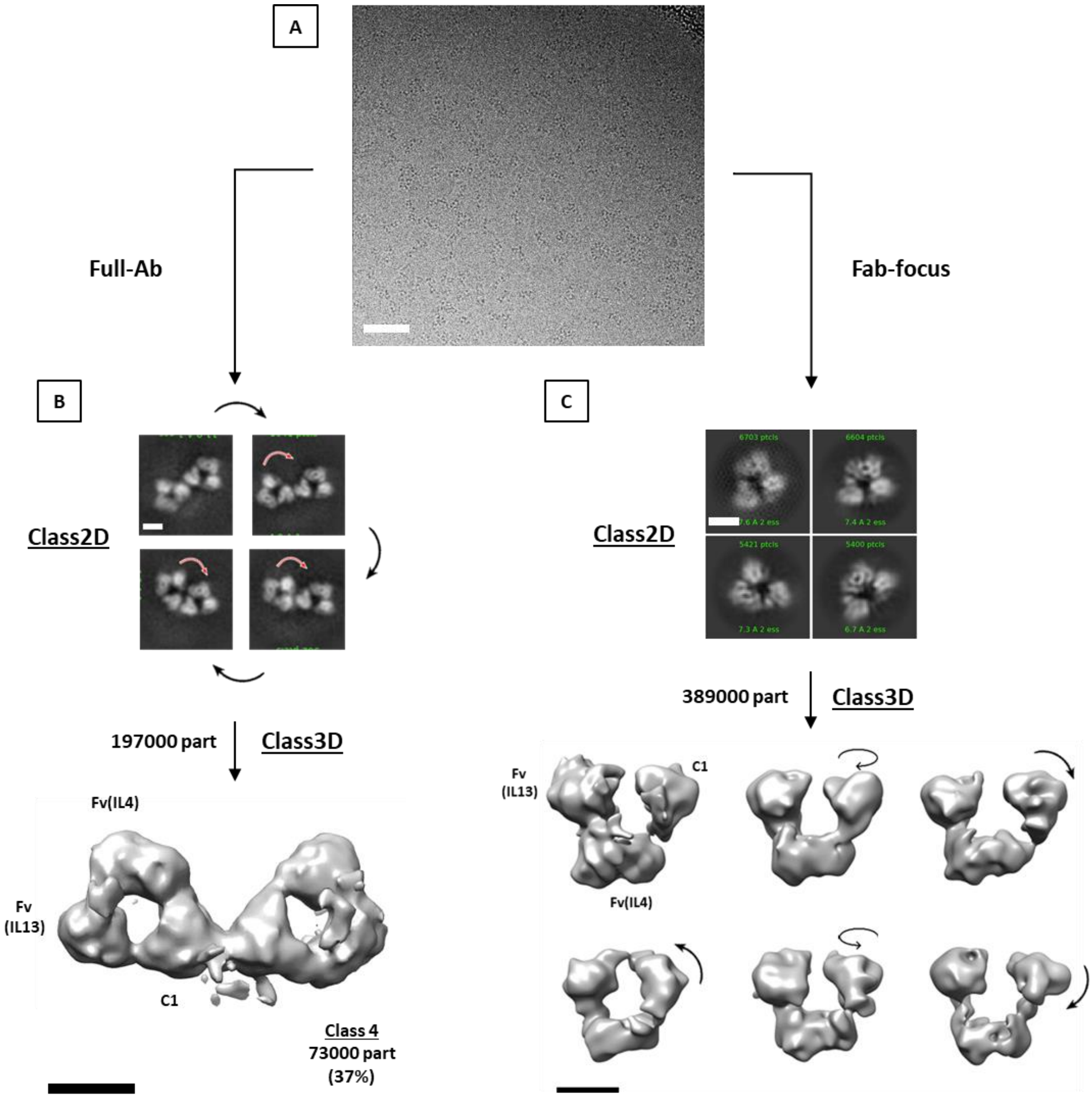

Figure 4.6: Image processing of the CODV-IL4/13 dataset and merging of data. (A) Representative micrograph of the CODV-IL4/13 dataset (scale bar = 500 Å). **(B)** 2D classes from the double complex dataset showed very strong preferential orientation and no density for Fc antigen density, which was also the case for 3D classifications**. (C)** Fab-focused 3D classifications from merged FabCODV-IL4 and FabCODV-IL4/IL13 also failed to show any antigen density. The resolution of these classes is similar to those obtained for CODV-IL4 (Figure 5A) as are indications of intra-Fab flexibility. Scale bar is 50 Å in both B and C.

The maps obtained from the particles followed an identical pattern to those obtained for CODV-IL4, resulting only in low-resolution Fab-Fab 3D reconstructions without clear density for Fc or ligands. As for CODV-IL4 a "Fab-focused" alignment was performed. Here, the CODV-IL4 and CODV-IL4/IL13 datasets were merged in the hope of boosting any signal for IL4. However, in none of the 3D steps of this process was any signal corresponding to the antigens observed (**Figure 4.5B**).

All the results and conclusions obtained from the free and complexed antibody datasets allowed us to build an image processing pipeline to follow, directed towards obtaining a high-resolution map of the antibody/antigen interface of the antibody within the full antibody context in close-to-native conditions, along with a way of observing large conformational changes of the whole antibody in 3D. We decided to apply everything we learned towards solving the structure of CODV-IL13, complexed with Tralokinumab (TC) by cryo-EM.

4.5 CODV-IL13 structure solution complexed with Tralokinumab

That the cryo-EM analysis of both the CODV-IL4 and CODV-IL4/IL13 failed to reveal any signal for antigen binding is perplexing and one can think of several possible explanations for this: 1) The antigens have dissociated from CODV during the EM sample preparation step 2) Preferred orientation of the CODV-antigen complexes on the cryo-EM grids precludes views of the bound antigen; 3) The flexibility of CODV results on the averaging out of density due to the antigens. In order to circumvent one, or all, of these possibilities a CODV-IL13-Tralokinumab triple complex (TC) was prepared. The hope here was that the presence of Tralokinumab would help stabilise the CODV-IL13 binding interface, reduce the inherent flexibility of CODV and reduce the propensity of CODV to adopt preferred orientations on cryo-EM grids. As described in section **3.6** on the **NS-EM** chapter, preliminary NS-EM studies of the triple complex indicated this to be a successful approach, therefore cryo-EM analysis of CODV-IL13- Tralokinumab was carried out.

After elucidating the correct conditions for vitrification and data collection of the TC (**Tables 4.3, 4.4, 4.5**) image processing was started using cryoSPARC 2.15. First, the 928-movie dataset collected using the IBS Glacios microscope and K2 camera at 130000x magnification was processed (**Figure 4.7A, left**). This was deliberately collected under high-contrast conditions (high dose, high defocus, objective aperture in) with the goal of being able to pick and identify TC particles in thicker ice. A 100-micrograph subset with high (>3.0 µm) defocus was subjected to an elliptical blob picking to take advantage of the elliptical shape of the TC as revealed in NS-EM experiments (section **3.6.2** of the **NS-EM** chapter) Based on this an ellipse with diameter values of 220 Å long and 150 Å wide was used. Iterative rounds of 2D classification of the picked particles and using the class averages as templates for re-picking. 10 good class averages from the Glacios dataset (**Figure 4.7B**) were then rescaled from 1.053 to 0.83 Å/pix and used to particle pick the Krios data, collected at 165000k.

After curation, a total of 14010 untilted K2-Krios movies from two separate datasets collected several weeks apart were preprocessed with MotionCor 2 and Multi Patch CTF, and a subset of 128 micrographs with the highest defocus values were selected for automatic particle picking (**Figure 4.7A, right**) using Glacios templates (see above) filtered at 50 Å. New templates were generated from this small subset of particles by 2D classification and used for automatic picking of the entire data set. Because of the time between the two data collections, each was processed separately until the 3D classification step, at which point the clean particles were merged into a single dataset and classified (**Figure 4.7C**). Class 3 of the final 3D classification was subjected to 3D refinement, and a 5.9 Å map was obtained (**Figure 4.7D; Figure 4.7F**) While several views of the triple complex were observed in 2D classification and 3D classification angular distribution plots, there was still some preferential orientation (**Figure 4.7E**), so a final tilted dataset (**Table 4.5**) of 1188 movies at 40^{o} tilt was collected and the particles were merged with those from the untilted set.

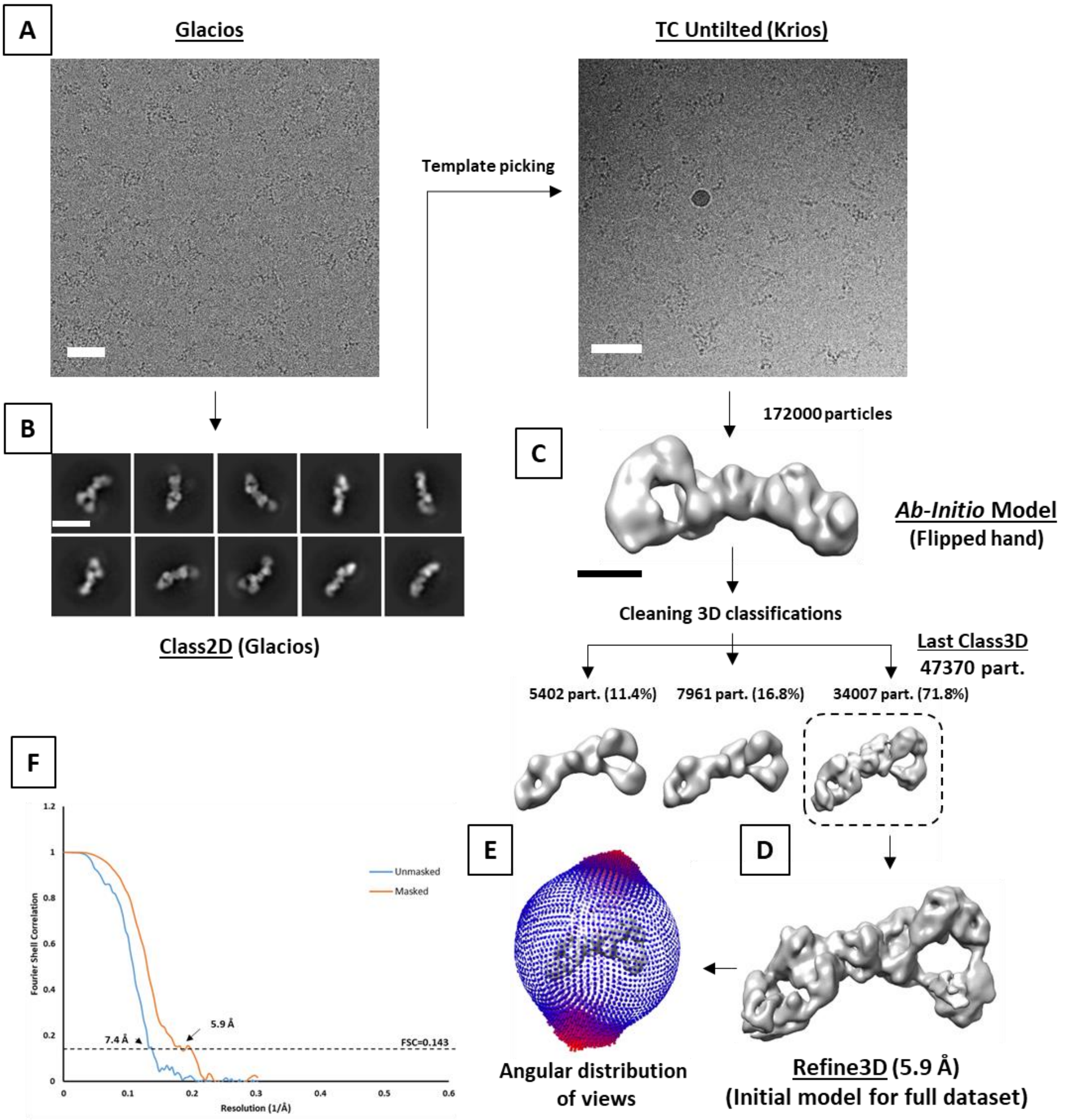

Figure 4.7: Part 1 of the TC image processing workflow. (A) Representative micrographs of the TC Glacios (left) and Krios datasets (scale bar = 500 Å in both). **(B)** 2D classes from Glacios, in different orientations, used to auto-pick the Krios data (scale bar = 150 Å). **(C)** Ab-initio model from Krios particles (scale bar = 50 Å), which was flipped on the Y axis before 3D classification steps that led to a well-defined TC density (circled) **(D)** This map was used for 3D refinement, which was used as the reference for the final dataset (Figure 8). **(E)** The histogram of angular distribution of particles showed 2 main orientations with almost few side views. **(F)** Fourier Shell Correlation with 0.143 cutoff of the Refine3D map, with unmasked and masked resolutions of 7.4 Å and 5.9 Å.

The best 2D classes from successive classification jobs corresponding to different views were then selected and unstacked with EMAN2's (Tang et al., 2007) *e2proc2d.py*. By using the BSOFT (Heymann, 2001) software, the pixel shifts of each 2D class was calculated assuming the centre of IL13 as the 0,0 point (or centre of the molecule). Images were then individually corrected with *relion_image_handler* and then restacked with the *relion_stack_create* command. Finally, the 2D templates (**Figure 4.8A, bottom**) were imported into cryoSPARC where the entire dataset of 15379 movies (**Figure 4.8A, top**) was repicked. We used this strategy with TC because in this case the centre of the molecule was a clear density (IL13), unlike the centres of the full antibodies (invisible hinge) and centres of the CODV-Fabs (empty space between domains).

After a few 2D classification steps in cryoSPARC 2.5, to only remove the obvious bad picks, the remaining 546717 2x binned total particles were exported directly to RELION 3.1, where they were subjected to 3D classification steps (**Figure 4.8B**) with a T value of 3 to avoid overfitting and a very loose circular mask with a high number of classes. Conformational clustering, during which clusters of similar conformations are grouped together to attempt to improve the estimated resolution, was attempted on class 5 (218717 particles). While the anti-IL4 Fv and C1 TC domains showed different conformations, resolution of the antigen binding interface dropped. This most populated 3D class with around 218000 particles showed electron density for IL13 with defined α-helical features. The class was subjected to 3D refinement, which resulted in a reconstruction with a gold-standard FSC resolution estimate of 4.51 Å.

At this point, the area around IL13 seemed well-resolved, with densities corresponding to its α-helices fitting well with the IL13 model from the Tralokinumab-IL13 crystal structure (PDB code: 5L6Y; Popovic et al., 2017). The models of the anti-IL13 Fv domains of both CODV (PDB code 5HCG; Steinmetz et al., 2016) and Tralokinumab (PDB code 5L6Y) also fitted well into the cryo-EM density, although here the lower resolution meant that no details could be discerned. Density for the C1 domain of Tralokinumab, connected to Fv by its linker region, was also present. However, compared to the Tralokinumab-IL13 crystal structure this domain is slightly rotated and not in-plane with Fv. Finally, density corresponding to the anti-IL4 Fv_1 and C1 domains of CODV were of low resolution and only partially complete, likely due to flexibility in this region in the CODV-IL13-Tralokinumab complex in solution. Subdividing the particle set into more 3D classes revealed different positions for both of the lower resolution CODV domains and for the Tralokinumab C1 (to a lesser degree), while the IL13 density flanked by both anti-IL13 Fv presented minimal movement. This observation can be better appreciated during the 3D variability analysis in **Figure 4.10C.**

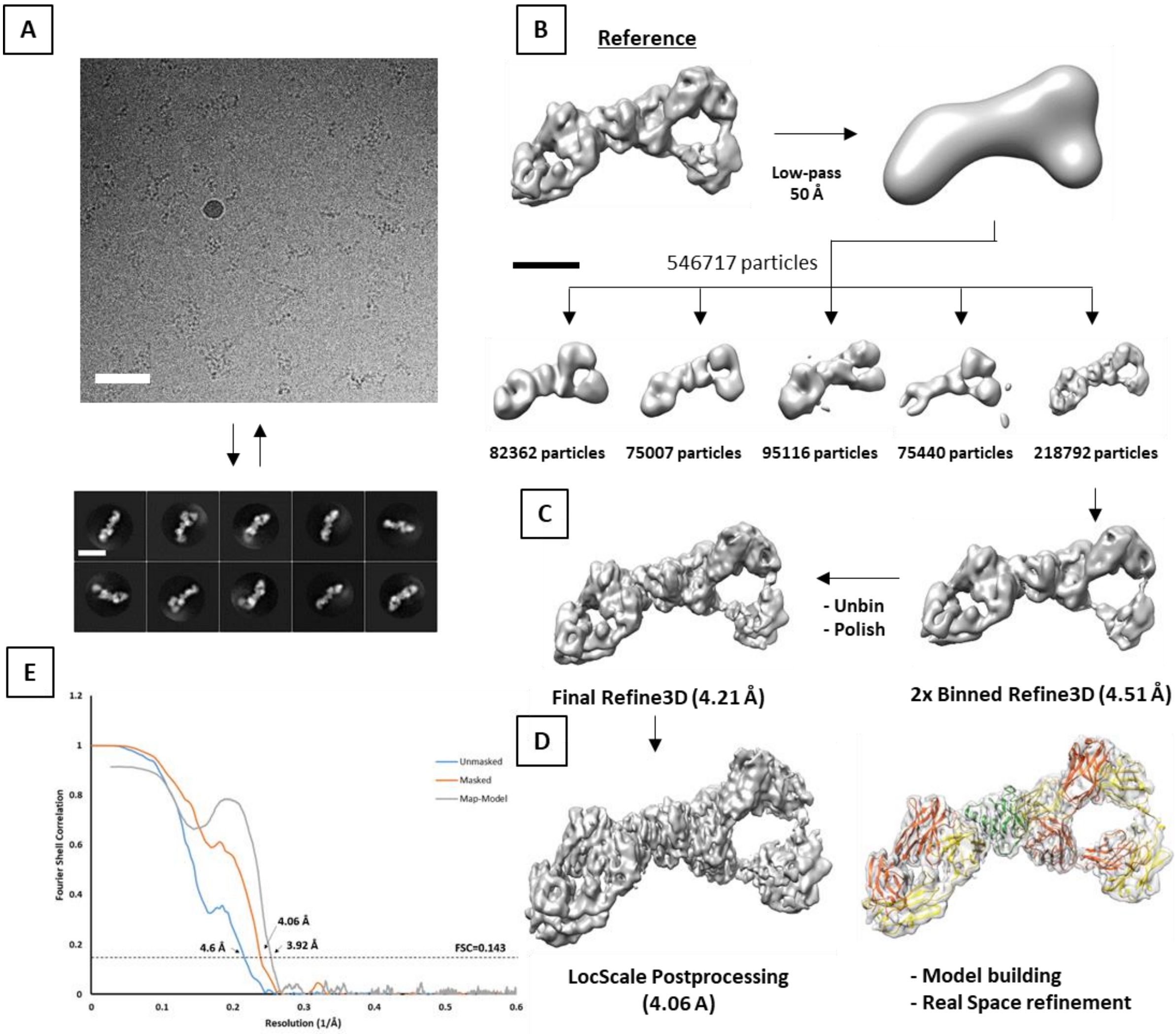

Figure 4.8: Workflow of the final steps of TC image processing. (A) Micrograph of TC Krios untilted data (top, scale bar= 500 Å) and recentered 2D classes of tilted+untilted data (bottom, scale bar = 150 Å) used in picking. **(B)** 3D classification process of the final picked particle set, with the low-passed model of Figure 7D as reference (scale bar = 50 Å). A medium resolution (4.51 Å) 2x binned refined map was obtained. **(C)** This map was further improved after unbinning and particle polishing (4.21 Å) **(D)** Postprocessed map obtained with rolling-window sharpening by LocScale, and fitted homology model of the complex, where heavy chains are orange, light chains yellow and IL13 is green. **(E)** Global map-model resolution estimation given by the FSC is 4.25 Å with a cutoff of 0.5 and 3.92 Å with the 0.143 criterion. For the map itself, unmasked and masked resolutions at 0.143 cutoff are 4.6 and 4.06 Å respectively.

As in other datasets, to perform the 3D refinement steps, RELION was preferred over cryoSPARC. In this process, the particle set from the intermediate resolution model in RELION was re-extracted as unbinned (0.827 Å/pix). CTF refinement of beam tilt, anisotropic magnification, per-particle defocus and astigmatism did not improve the resolution, rather they made it worse and were therefore ignored. Bayesian polishing was however successfully performed to estimate per-particle motions from the movie frames. A new model was refined (**Figure 4.8C**) with these unbinned, polished particles, and after postprocessing the estimated resolution of the reconstruction was 4.21 Å and with an estimated global B-factor of -190 Å^2.

The density obtained was more detailed than in previous steps (see above) with separation between β-sheets of the anti-IL13 Fv domains of both CODV and Tralokinumab being discernible.

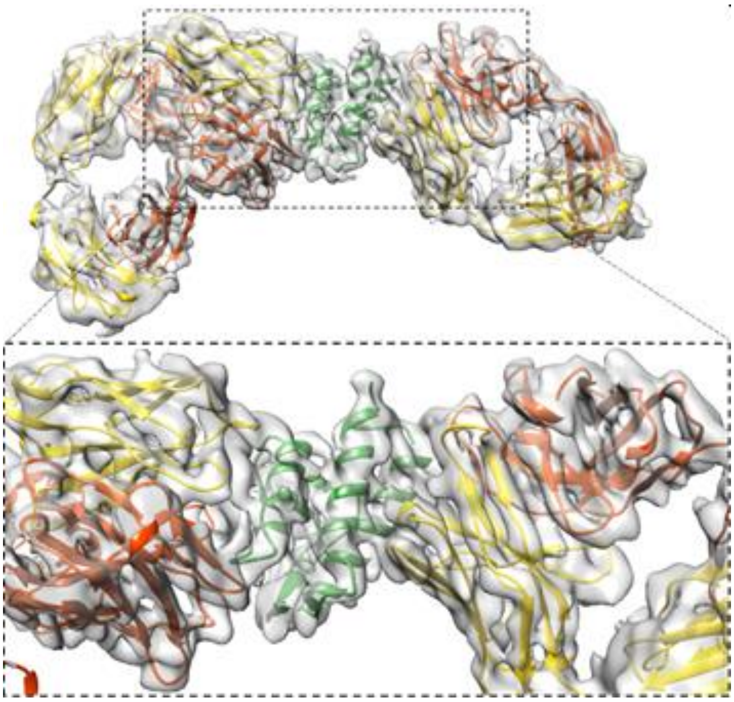

Figure 4.9: Closer inspection of the LocScale sharpening and real-space refinement of the CODV-IL13-Tralokinumab complex by cryo-EM. While all densities of the homology model (CODV-Fab on the left, Tralokinumab on the right, IL13 in the center) seem to fit the final TC map, it is at the IL13 interface where secondary structure densities are better-defined. Light chains are in yellow, heavy chains in orange and IL13 in green.

For model building, first a homology model was obtained using SWISS-MODEL (Waterhouse et al., 2018). To create the template model, existing crystal structures of CODV-Fab and IL13-Tralakinumab were fitted into the 3D map of TC and saved as a single model. The homology model thus obtained was very similar to the template, with a global RMSD of 32 Å, mainly differing at the linker regions and a loop at IL13 that was not built in the crystal structure.

Fitting of all domains of the CODV-IL13-Tralokinumab homology model generated above to the cryo-EM density was challenging as the orientations of all the domains not involved at the IL-13 binding interface (for both CODV and Tralokinumab) were different than what is seen in the crystal structures on which the homology model was built. The homology model was therefore divided into its individual domains and each was rigid-body fitted separately. The resulting model was then rebuilt in Coot in compliance with geometric restraints and then refined by real space refinement with rigid body morphing in Phenix (Afonine et al., 2018). Because of the apparent difference in resolution depending on the area of the map, the model obtained was used to sharpen the Refine3D map (**Figure 4.8D**) using the rolling window method implemented in LocScale program of the CCPEM package. The output map was well-sharpened (**Figure 4.9**), with the higher resolution regions having virtually no noise density and with the lower resolution regions not over-sharpened and more akin to their resolution. The final masked and unmasked 0.143 FSC resolutions were determined to be 4.6 and 4.06 Å respectively (**Figure 4.8E**). This map was used as an input for a last real space refinement step of the model in Phenix. The estimated map-model global resolution by Fourier Shell Correlation of this final masked map was 4.25 Å with the 0.5 FSC criterion and 3.92 Å with the 0.143 FSC criterion (**Figure 4.8E, gray**). Ramachandram outliers were 0.17%, which are accepted in the Phenix validation, but do not interfere with the binding site and will be fixed nonetheless during the final stages of refinement.

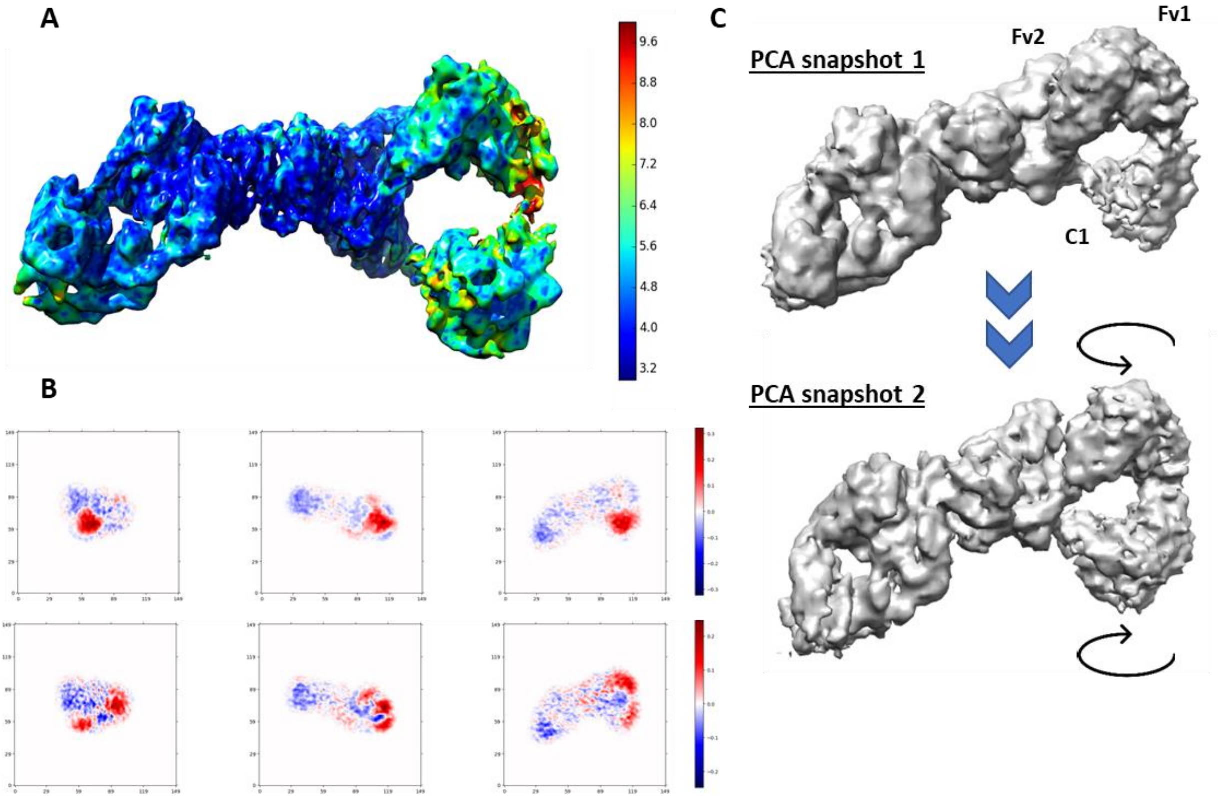

Figure 4.10: Local resolution and movement analysis of the refined TC map. (A) ResMap calculated a range of resolutions, closer to 3.5-4 Å towards the centre of the complex, and 6-9 A on the regions flanked by flexible linkers. **(B)** Principal component analysis (PCA) within cryoSPARC3 evidences great movement at the lower resolution regions. The colors are more intense the higher the eigenvector (and thus, movement) value within different sections of the molecule. **(C)** As an example of the movement, we show two snapshot of one of the movies obtained from one of the eigenvector movement analyses. The anti-IL4 Fv shows a counter-clockwise rotation relative to the anti-IL13 Fv. Similarly, C1 also shows a counter-clockwise rotation. Both right-side domains of C1 and Fv1 rotate to the same direction, which may be due to them being directly bound by a linker.

ResMap (Kucukelbir et al., 2014b) analysis of the half-maps (**Figure 4.10A**), showed a clear division in resolution estimates throughout the cryo-EM density obtained. Regions corresponding to α-helixes of IL13 and β-sheets of the CODV and Tralokinumab Fvs interacting with IL-13 are estimated to be at 3.5-4 Å resolution, while the domains located further away from the interface, particularly the C1 and the anti-IL4 Fv domains of CODV, are at progressively lower resolution.

Perhaps unsurprisingly, Principal component analysis (PCA) with multibody refinement in RELION and 3D Variability analysis in CryoSPARC 3 (**Figure 4.10B**), both with 3 eigenvectors as input (linear movements in 3D space of a variance cluster, in this case a part of the 3D structure), reveals large rotations and translations of these two domains coupled, with a slight up-and-down movement, perpendicular to the planar surface of the complex, of the Tralokinumab-C1 domain. Example snapshots of the movies corresponding to these dynamics can be consulted in the **Figure 4.10C**. Concerning the movement observed for the CODV C1 and anti-IL4 Fv domains, this is probably a consequence of the glycine-linker regions of the antibody. Indeed, the flexibility of CODV has been proven to play a key role in antigen recognition (Bongini et al., 2005; Sandin et al., 2004) . Unfortunately for high-resolution EM studies, these physiological advantages severely limit attempts at obtaining high resolution reconstructions unless, as is the case for CODV-IL13- Tralokinumab, one, or eventually, both of the CODV-antigen interfaces are locked in place.

To analyse the binding interfaces of IL13 to both the CODV and Tralokinumab Fvs, a sequence-based structure alignment was performed using UCSF Chimera, between the TC model and the crystal structures of Tralokinumab-IL13 (PDB code:5L6Y; Popovic et al., 2017) and BB13-IL3 (unpublished, private communication) where BB13 is an anti-IL13 IgG Fab sharing its Fv with Fv2 of our CODV construct. This way, the structures were matched with the highly conserved residues of IL13 as a common point. The results are shown in **Figure 4.11B**. As can be seen from **Figures 4.11C and 4.11D**, the structures of the CODV-IL13-Tralokinumab interface obtained by cryo-EM and X-ray crystallography do not differ greatly, especially at the CDR level, with significant discrepancies only affecting loops that do not directly take part in binding (red arrow in **Figure 4.11C**) and which might be expected to be more mobile in solution. The RMSD values for several parts of the structures are collected in **Table 4.6.**

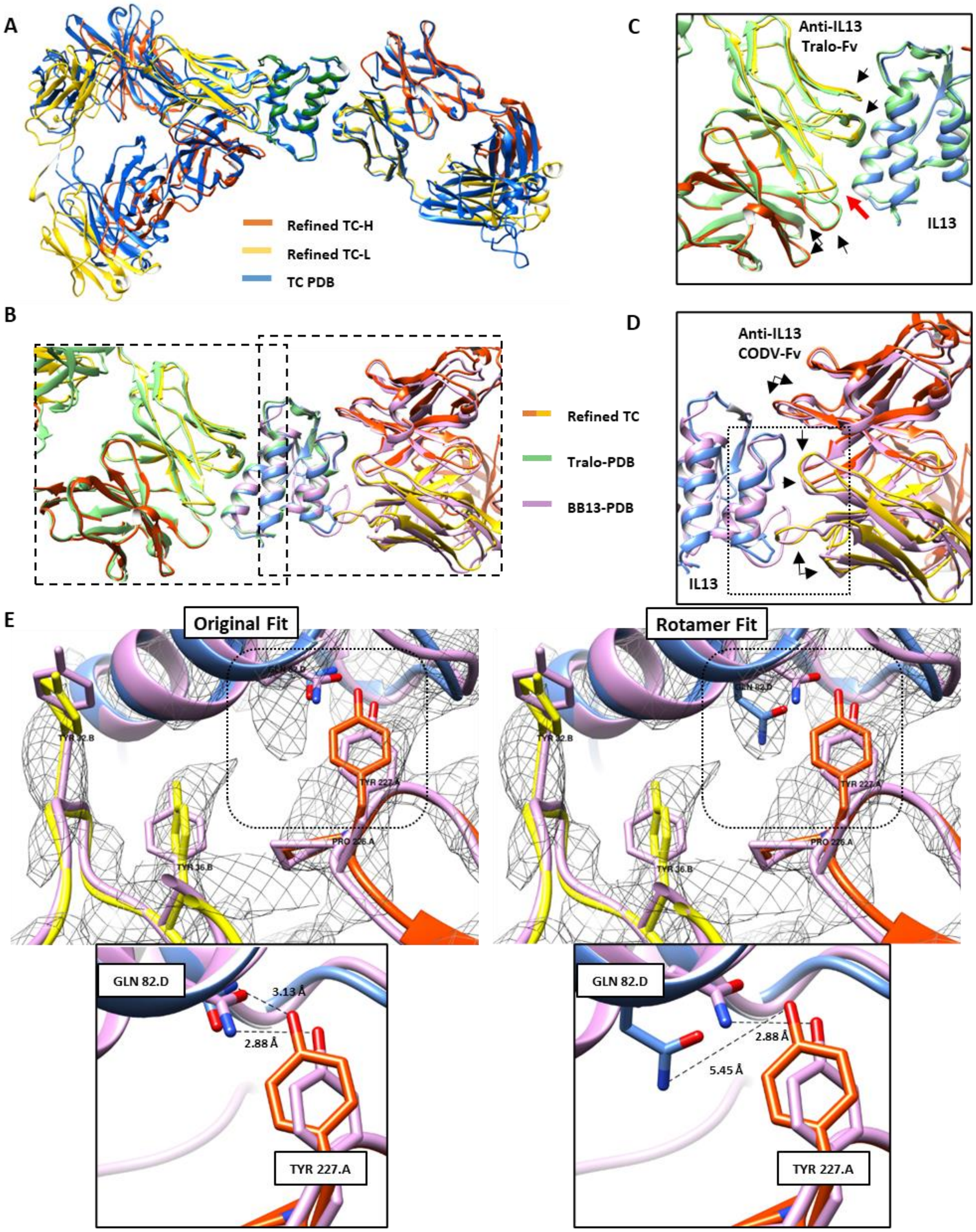

Figure 4.11: Comparative analysis of the cryo-EM model of CODV-IL13-Tralokinumab with available X-Ray crystallography data. (A) The cryo-EM TC model (light chains in yellow, heavy chains in orange) shows different positions for the CODV C1, Fv1 and Tralokinumab C1 regions compared to the those observed in crystal structures (blue). **(B)** The anti-IL13 Fv region of TC is well-conserved compared to the BB13 (pink) and Tralokinumab-IL13 (green) crystal structures, proving at main chain level that affinity loss is not a concern when using antibodies as markers and stabilizers. **(C)** The tralokinumab region has 5 conserved CDRs (black arrows) while one of them in the light chain seems to differ (red arrow) **(D)** For CODV-Fvs, the CDRs are well-conserved. **(E)** At the CODV-IL13 interface, where the resolution may be higher than the global 4.06 Å, some densities corresponding to aromatic side chains can start to be appreciated. The original fit given by Phenix respects bond constraints, however EM density information at this resolution may still allow other rotamers to incorrectly fit.

Additionally, the map seems to improve the global 4.06 Å resolution according to **Figure 4.10A** at the IL13 interface, and this allows, in some cases, to identify EM densities corresponding to large side chains such as aromatics (**Figure 4.11E**). The resolution of the map however is not yet sufficient for precise positioning of other side chains. As an example (**Figure 4.11E**), the Phenix output of the Gln-82 to Tyr-227 H-bond is close to the value observed in the BB13 PDB. However, were one to fit rotamers into densities when resolution is not sufficient, there could be a risk of removing bonds or salt bridges at the binding interface crucial for drug design. Fortunately, the resolution can still be improved by additional EM processing steps or by collecting more data.

That the conformations of the main chains of the CDRs are conserved in X-ray and EM, however, allows one to argue with confidence that, sample preparation and vitrification for cryo-EM experiments of CODV-IL13-Tralokinumab do not, at a structural level, affect the affinity of either antibody for IL13. This supports the idea of exploiting secondary labelling antibodies in the cryo-EM study of CODV-antigen complexes. Furthermore, the conformation of CODV observed in the cryo-EM structure of CODV-IL13- Tralokinumab should not affect its ability to bind, simultaneously, both IL13-Tralokinumab and IL4. Work on the preparation and structural characterisation of an IL4-CODV-IL13-Tralokinumab is ongoing, although the experiences described throughout this thesis manuscript suggest that the supplementary antibody labelling of IL4 may be required in order to obtain high resolution structural information.

Structure	**Anti-IL13 Fv**			**CDR**		**Full Model**	
1	BB13	FabCODV	Tralo.	FabCODV	Tralo.	SwissModel	PDB
2	TC	TC	TC	TC	TC	PDB	TC
RMSD (Å)	1.9575	1.3955	1.0825	1.013	0.7	32.48	34.9

Table 4.6: Root mean square deviation (RMSD) values for model-model comparisons in TC processing

Discussion

The CODV format has been shown to strongly and effectively bind antigens at both room and cold temperatures, and its circular self-supporting architecture restricts domain-level movements that may otherwise hinder antigen binding and stability, as seen in other bispecific antibody formats such as DVD-Ig. However, previous work (Steinmetz et al., 2016) has shown that having a crystal structure and SPR data relating to antigen binding is not always sufficient for a successful progression towards characterization of the full binding mode. In the work presented in this PhD thesis, electron microscopy has been presented as both an alternative and a complementary technique towards understanding the structural aspects of such molecules.

All antibodies studied in this thesis have proven to be very flexible. While small domain-level flexibilities have a better chance of resulting in high-resolution EM data, the multispecific antibodies which have been the focus of this work have shown fragment-to-fragment movements that correspond to large conformational heterogeneity, due to the structurally disorganized and inherently flexible nature of their hinge regions. Indeed, attempts have been made in both SAXS and cryo-electron tomography experiments to map and cluster the movements into groups (Tian et al., 2015; Zhang et al., 2015), and the results show a continuous movement of the fragments relative to each other. One can therefore argue that in solution, at any given time, a large number of these conformations exist simultaneously. This has been further proven in the NS-EM and cryo-EM results presented here, where, not only this flexibility is evident during 2D and 3D classification steps, but in many cases also hinders the visualisation of all the three antibody domains in an EM map, as particles with different conformations are averaged together.

It is shown here that it is indeed possible to separate discrete whole-antibody level conformations where the Fc is visible and especially flexible, but doing so dilutes the per-class particle count so much that each conformation contains 1% or less of the total particles from the dataset. The main way to solve this problem would be to limit the flexibility, for example by binding the antibody to a very large target. Some in-progress studies within Sanofi (data not shown) and antibody-virus work (Oyen et al., 2018) seem to point in this direction, where large ligands help in restricting the movement and allow for better alignment and classification. Other suggestions, based on observations of IgG isotypes in literature (Vidarsson et al., 2014), would include changing the amino acid composition of the hinge itself when designing the antibody heavy chains. Each IgG has a different type of hinge which confers unique properties to the antibodies. The IgG2 hinge, for example, has higher proline and cysteine content, which creates a complex network of disulphide bridges that confer rigidity to the region and by extension, the antibody (Vidarsson et al., 2014). While researchers working on designing bispecific antibodies may favor IgG1 or IgG4 hinges due to their aid in helping correct chain isomerization, it might be worth exploring alternatives to open the possibility of routinely using cryo-EM for whole-antibody structure determination.

The work presented here also showed that the multispecific antibodies tend to exhibit strong preferential orientation on EM grids. There are three ways to try and tackle this problem. One possibility would be to routinely work with tilted data collection, where resolution is sacrificed, and higher doses have to be applied. In our case, we did not observe a large increase in rare views. Nevertheless, this was sufficient to increase map resolution and obtain a successful reconstruction. The second would be to find an excipient (like a detergent) that induces random orientations on the sample as it is the case with other proteins. The third would be to collect more data (in the order of millions of particles). This would be very expensive both in human resources and microscope time, but is increasingly used in the literature (Dong et al., 2019; Stella et al., 2018) and allows to find rare views and help in differentiating conformational states.

This study confirms that NS-EM is an indispensable tool for a wide range of objectives, from sample quality checking to assessing labelling techniques. It has also shown that, under the right conditions, low resolution NS-EM reconstructions can be then used as a starting point for refinement during the cryo-EM part of a project and are especially useful when extreme flexibility does not allow visualisation of all regions of a molecule by *ab-initio* methods.

This study has also shown that for the air-water interface issue when when screening cryo-EM vitrification conditions (Bondos & Bicknell, 2003; D'Imprima et al., 2018), it is possible to make use of a detergent like DDM and use slightly thicker areas of the grid in order to get particles with an acceptable distribution and contrast. This issue has risen on many points of the project, where long purification steps, extensive exposure to the air-water interface and Quantifoil-like supports all appear to contribute to increased aggregation of the sample. The aggregation mechanisms involving antibodies are many (Glaeser, 2018). Even now, this process is still not completely understood, although there have been some efforts in predicting and solving different causes and mechanisms that may lead to these molecules aggregating and denaturing (Brych et al., 2010; Lee et al., 2013). Here, using a high-resolution single purification step, decreasing the grid hole size, addition of detergents to increase particle dispersion and protection from hydrophobic environments and using a pure-carbon support all contributed to obtaining full and well-dispersed CODV-Igs for cryo-EM imaging.

Concerning the processing of micrographs obtained from flexible multi-domain proteins such as antibodies are, this work has provided evidence that conventional approaches often do not work. While software like RELION does a good job in many samples as a complete pipeline, in the cases described here it has not proven very useful until the 3D classification stage. In contrast, cryoSPARC offers a very complete curation system that greatly helps to remove bad movies and bad particles alike and its different gray value normalization method, at least for the antibodies tested, gives improved 2D classes when compared to other software. However, it does appear to falter in early 3D work, with results not as good as those produced by RELION’s 3D classification. cisTEM, on the other hand, has also shown promise for the entire process in some test runs and it is a good alternative if the workstations are only CPU-based.

The studies presented here show that it is possible to image the structure of antibody-antigen interfaces within the full-antibody context, using a “Fab-focused EM approach”. Ignoring the other antibody fragments for picking and alignment allows to significant improvement in classification and to obtain 2D classes with a variety of views. This also helps during the *ab-initio* and 3D classification steps as shown in the CODV-IL4 dataset (refer to **4.4.2.2.1**), where Fabs have the correct number of domains and can be discerned from each other, unlike what was observed when working at whole-antibody level, in both NS-EM and cryo-EM.

One of the main issues of the PhD project was that during EM processing of antibodies bound to antigens, the latter could not be identified at any point of the image processing pipeline. This is puzzling and was the main reason many experiments described in the

Purification and Characterization chapter were carried out. Here, all experiments showed that the antigens were not only present in the sample tube, but also bound to the antibody with picomolar-level affinities. This prompted the exploration of methods which would allow the observation of small antigens in EM when they do not appear when following a conventional EM pipeline. Some interleukins have multiple binding sites (Barton et al., 1999; Evans et al., 1995; Ultsch et al., 2013). Where these do not overlap, as is the case for IL13, this allows to use labelling and locking antibody fragments. At the time of writing it is still not clear whether the reason IL13 could be identified in the CODV-IL13-Tralokinumab triple complex is ligand stabilization or improvement in particle alignment by providing an extra density. To shed light into this question the quadruple complex (IL4-CODV-IL13-Tralokinumab) has been prepared and will be the subject of EM studies outside of thesis work. If IL4 is observed in this complex, this will likely be a result of the improved particle alignment the presence of Tralokinumab provides. On the contrary though, failure to observe any density corresponding to IL4 would add weight to the hypothesis that IL4 must be locked in place by another molecule.

Nevertheless, TC was reconstructed at an estimated 4.06 Å resolution, and this allowed us to fit a model built by homology, where higher resolution was present at the IL13 binding interface. This interface was very well-conserved at the main chain level when compared to reference crystal structures, the structure only becoming more divergent (and the map less resolved) the further away from the binding sites (**Figure 4.10A**) due to the various conformations that these domains can adopt when only being supported by linkers (**Figures 4.10B,C**). While not helpful when attempting to reconstruct all the structure at high-resolution, flexibility plays a key role in antigen recognition by extending the range at which antibodies can interact and adopt a more suitable orientation for binding (Bongini et al., 2005; Sandin et al., 2004). At the binding site, some larger side chains such as aromatics could be fit, while resolution was still lacking for other smaller ones. Considering that the main chain was identical at the CDRs and IL13, and that some side chains that could be fit were essentially in the same orientation, we can argue that affinity is conserved in cryo-EM and that binding other Fabs does not change the affinity of CODV for IL13. K_D measurements on CODV constructs with different linker lengths have reported a considerable difference in affinity (Steinmetz et al., 2016), therefore while we are inclined to believe that the CDR structure would still be conserved, it would be an interesting avenue for research to discover, at a structural level, whether the loss of affinity is due to steric hindrance or a change in the binding site structure when a new linker is introduced.

Finally, considering the many datasets analyzed during the project, automation in cryo-EM should be mentioned. As samples become more and more complex and solutions for flexibility and rare views are more in-demand (Dong et al., 2019; Stella et al., 2018), there is an urgent need to design systems that can allow to collect and process, in as little time as possible, datasets that will result in particle numbers in the order of millions. Indeed there is currently much activity in the development of programs that offer an integrated system of automatic data collection and processing: Warp (Tegunov & Cramer, 2018), an integration of a neutral network picking system and on-the-fly image processing pipeline; Serial EM (Mastronarde, 2003), a data collection software that has higher throughput than EPU; Scipion (de la Rosa-Trevín et al., 2016), which allows streaming on-the-fly processing and is used at our CM01 beamline of the ESRF and cryoSPARC Live, which is designed to automatically carry out the entire EM pipeline, from micrograph collection to density map.

Chapter 5

Conclusion

5. Conclusion

6.1 Full antibodies in the future of cryo-EM

Electron microscopy has developed to a point in which details of antibody-antigen interfaces can be resolved at high-resolution. This is a leap forward in the structure-based drug design field, as researchers can now use EM as a complementary technique to NMR or X-ray crystallography to study antibody-antigen behaviour in near-native conditions. Additionally, it provides information about the dynamics of the molecule as multiple conformations and orientations may be present on an EM grid.

Being able to obtain a high-resolution map of the whole antibody, including Fc, may open the door to new therapeutic approaches such as those involving neonatal Fc receptors, as highlighted earlier in **Chapter 4**. This work has shown for the first time that it is indeed possible to obtain separate maps of different conformations of CODV antibodies showing the three domains. However, it is also showed that while possible, the particle proportion compared to the total in each class is so low that the number of particles needed must be at least one order of magnitude higher to aim for high resolution. It is true that as it currently stands, such a task would require too large amounts of funding and time. However, it may be possible to reduce this need by increasing the number of particles per micrograph.

As evidenced in the micrographs shown in **Chapter 4**, there is still great room for improvement of vitrification conditions of antibodies. Addition of DDM and modifying other conditions presented does help in preventing aggregation. However, the population of particles on the grid holes is very low compared to most datasets published nowadays. Detergents such as CHAPSO (Chen et al., 2019), or further exploring graphene-based grid treatment (Russo & Passmore, 2014) seem to be useful starting points towards achieving this feat. Furthermore, with the development of efficient deep-learning based particle pickers such as crYOLO (Wagner et al., 2018) and Topaz (Bepler et al., 2019) one could afford to allow antibodies closer together during grid preparation.

6.2 Small antigen labelling for EM

As shown in Chapter 4.5, adding an antibody fragment to a small antigen already bound to another antibody allowed the visualisation, at medium resolution, of both antibody-antigen binding interfaces Here, affinity seems to also be conserved, as suggested by the identical positions of the main chain at the CDRs when superposing the CODV-IL13-Tralokinumab triple complex EM model with those of the crystal structures of IL13-Tralokinumab and BB13. As discussed in the **Discussion** of **Chapter 4**, at the moment there is no strong evidence whether being able to see the IL13 density is due to the antigen interface stabilization or because of improved alignment due to the extra antibody density. It is planned to answer this question in the near future by adding a non-labelled IL4 into the triple complex and performing cryo-EM experiments, following on from the results presented for NS-EM studies of this IL4-CODV-IL13-Tralokinumab quadruple complex (QC) presented in **Chapter 3.6.2.** Moreover, even if this experiment is successful, one also can imagine adding an IL4 label (i.e. an antibody recognising its His6-tag) which might improve results.

Indeed, this technique could be extended to many other molecules, for example by designing nanobodies or other antibody fragments that bind to a region not involved in antibody-binding.

Such techniques could potentially expand the range of antibody-antigen complexes that researchers can work with and help develop new drug-design strategies.

6.3 An EM pipeline for antibodies

It is our hope that this work will serve as a starting point for future attempts at electron microscopy work with full antibodies, whether the goal is the structure of the entire antibody itself or a part of it within the whole-Ab context. While it has been very time consuming, there may be researchers that will save months or even years of trial and error by having a notion of what works and what does not.

The other goal during this project was to attempt this cryo-EM pipeline with other antibody formats (hence, why we initially included TBTI and TDT in the early chapters), to establish whether the conclusions derived from the cryo-EM work on CODV could be translated to other antibodies. While being initially optimistic that there would be sufficient time for this, the reality is that overcoming challenges in the EM analysis of CODV and its complexes with antigens has been too time-consuming. Nevertheless, it is hoped that the results and experiences described here will contribute to a common approach to whole-antibody studies.

6. References

Adams, P. D., Afonine, P. V., Bunkóczi, G., Chen, V. B., Davis, I. W., Echols, N., … Zwart, P. H. (2010). PHENIX: A comprehensive Python-based system for macromolecular structure solution. *Acta Crystallographica Section D: Biological Crystallography*, *66*, 213–221.

Adrian, M., Dubochet, J., Lepault, J., & McDowall, A. W. (1984). Cryo-electron microscopy of viruses. *Nature*, *308*, 32–36.

Aebi, U., & Pollard, T. D. (1987). A glow discharge unit to render electron microscope grids and other surfaces hydrophilic. *Journal of Electron Microscopy Technique*, *7*, 29–33.

Afonine, P. V., Poon, B. K., Read, R. J., Sobolev, O. V., Terwilliger, T. C., Urzhumtsev, A., & Adams, P. D. (2018). Real-space refinement in PHENIX for cryo-EM and crystallography. *Acta Crystallographica Section D: Structural Biology*, *74*, 531–544.

Asarnow, D., Palovcak, E., & Cheng, Y. (2019, December 16). *asarnow/pyem: UCSF pyem v0.5*. https://doi.org/10.5281/ZENODO.3576630

Barton, V. A., Hudson, K. R., & Heath, J. K. (1999). Identification of three distinct receptor binding sites of murine interleukin-11. *Journal of Biological Chemistry*, *274*, 5755–5761.

Bepler, T., Morin, A., Rapp, M., Brasch, J., Shapiro, L., Noble, A. J., & Berger, B. (2019). Positive-unlabeled convolutional neural networks for particle picking in cryo-electron micrographs. *Nature Methods*, *16*, 1153–1160.

Berne, B. J., & Pecora, R. (2000). *Dynamic Light Scattering: With Applications to Chemistry, Biology, and Physics*. Retrieved from https://books.google.com/books?hl=en&lr=&id=vBB54ABhmuEC&oi=fnd&pg=PA1&dq=dynamic+light+scattering&ots=L7jCF1ofoi&sig=oLhNnS9Y3cGflS724B29r8PHJM8#v=onepage&q=dynamic light scattering&f=false

Bondos, S. E., & Bicknell, A. (2003). Detection and prevention of protein aggregation before, during, and after purification. *Analytical Biochemistry*, *316*, 223–231.

Bongini, L., Fanelli, D., Piazza, F., De Los Rios, P., Sandin, S., & Skoglund, U. (2005). Dynamics of antibodies from cryo-electron tomography. *Biophysical Chemistry*, *115*, 235–240. Elsevier.

Booth, D. S., Avila-Sakar, A., & Cheng, Y. (2011). Visualizing proteins and macromolecular complexes by negative stain EM: from grid preparation to image acquisition. *Journal of Visualized Experiments : JoVE*, 3227.

Bottou, L. (2010). Large-scale machine learning with stochastic gradient descent. *Proceedings of COMPSTAT 2010 - 19th International Conference on Computational Statistics, Keynote, Invited and Contributed Papers*, 177–186. Springer Science and Business Media Deutschland GmbH.

Brillault, L., & Landsberg, M. J. (2020). Preparation of Proteins and Macromolecular Assemblies for Cryo-electron Microscopy. In *Methods in Molecular Biology* (Vol. 2073, pp. 221–246). Humana Press Inc.

Brinkmann, U., & Kontermann, R. E. (2017). The making of bispecific antibodies. *MAbs*, *9*, 182–212.

Brosey, C. A., & Tainer, J. A. (2019, October 1). Evolving SAXS versatility: solution X-ray scattering for macromolecular architecture, functional landscapes, and integrative structural biology. *Current Opinion in Structural Biology*, Vol. 58, pp. 197–213. Elsevier Ltd.

Brüggeller, P., & Mayer, E. (1980). Complete vitrification in pure liquid water and dilute aqueous solutions. *Nature*, *288*, 569–571.

Brych, S. R., Gokarn, Y. R., Hultgen, H., Stevenson, R. J., Rajan, R., & Matsumura, M. (2010). Characterization of antibody aggregation: Role of buried, unpaired cysteines in particle formation. *Journal of Pharmaceutical Sciences*, *99*, 764–781.

Carroni, M., & Saibil, H. R. (2016, February 15). Cryo electron microscopy to determine the structure of macromolecular complexes. *Methods*, Vol. 95, pp. 78–85. Academic Press Inc.

Chen, J., Noble, A. J., Kang, J. Y., & Darst, S. A. (2019). Eliminating effects of particle adsorption to the air/water interface in single-particle cryo-electron microscopy: Bacterial RNA polymerase and CHAPSO. *Journal of Structural Biology: X*, *1*, 100005.

Chennamsetty, N., Helk, B., Voynov, V., Kayser, V., & Trout, B. L. (2009). Aggregation-Prone

Motifs in Human Immunoglobulin G. *Journal of Molecular Biology*, *391*, 404–413.

Cleland, W. W. (1964). Dithiothreitol, a New Protective Reagent for SH Groups. *Biochemistry*, *3*, 480–482.

Crewe, A. V., Eggenberger, D. N., Wall, J., & Welter, L. M. (1968). Electron Gun Using a Field Emission Source. *Review of Scientific Instruments*, *39*, 576–583.

D'Imprima, E., Floris, D., Joppe, M., Sánchez, R., Grininger, M., & Kühlbrandt, W. (2018). The deadly touch: protein denaturation at the water-air interface and how to prevent it. *BioRxiv*, 400432.

D'Imprima, E., Floris, D., Joppe, M., Sánchez, R., Grininger, M., & Kühlbrandt, W. (2019). Protein denaturation at the air-water interface and how to prevent it. *ELife*, *8*. https://doi.org/10.7554/eLife.42747

Danev, R., & Baumeister, W. (2016). Cryo-EM single particle analysis with the Volta phase plate. *ELife*, *5*. https://doi.org/10.7554/eLife.13046

De Carlo, D., Adrian, Kälin, Mayer, & Dubochet. (1999). Unexpected property of trehalose as observed by cryo-electron microscopy. *Journal of Microscopy*, *196*, 40–45.

de la Rosa-Trevín, J. M., Otón, J., Marabini, R., Zaldívar, A., Vargas, J., Carazo, J. M., & Sorzano, C. O. S. (2013). Xmipp 3.0: An improved software suite for image processing in electron microscopy. *Journal of Structural Biology*, *184*, 321–328.

de la Rosa-Trevín, J. M., Quintana, A., del Cano, L., Zaldívar, A., Foche, I., Gutiérrez, J., … Carazo, J. M. (2016). Scipion: A software framework toward integration, reproducibility and validation in 3D electron microscopy. *Journal of Structural Biology*, *195*, 93–99.

Doane, F. W., & Anderson, N. (1987). ELECTRON MICROSCOPY IN DIAGNOSTIC VIROLOGY. A PRACTICAL GUIDE AND ATLAS. In *CUP Archive* (Vol. 52). Retrieved from https://books.google.fr/books?hl=en&lr=&id=6vw8AAAAIAAJ&oi=fnd&pg=PR13&dq=FW+Doane,+N+Anderson&ots=cQrsy9Hai0&sig=D4cRKdDN1SfvmcYhOxSKZHikX-s&redir_esc=y#v=onepage&q=FW Doane%2C N Anderson&f=false

Dong, Y., Zhang, S., Wu, Z., Li, X., Wang, W., Zhu, Y., … Mao, Y. (2019). Cryo-EM structures and dynamics of substrate-engaged human 26S proteasome. *Nature*, *565*, 49–55.

Dubochet, J., & McDowall, A. W. (1981). VITRIFICATION OF PURE WATER FOR ELECTRON MICROSCOPY. *Journal of Microscopy*, *124*, 3–4.

Elliott, J. M., Ultsch, M., Lee, J., Tong, R., Takeda, K., Spiess, C., … Scheer, J. M. (2014). Antiparallel Conformation of Knob and Hole Aglycosylated Half-Antibody Homodimers Is Mediated by a CH2–CH3 Hydrophobic Interaction. *Journal of Molecular Biology*, *426*, 1947–1957.

Emsley, P., & Cowtan, K. (2004). Coot: Model-building tools for molecular graphics. *Acta Crystallographica Section D: Biological Crystallography*, *60*, 2126–2132.

Evans, R. J., Bray, J., Childs, J. D., Vigers, G. P. A., Brandhuber, B. J., Skalicky, J. J., … Eisenberg, S. P. (1995). Mapping receptor binding sites in interleukin (IL)-1 receptor antagonist and IL-1β by site-directed mutagenesis. Identification of a single site in IL-1ra and two sites in IL-1β. *Journal of Biological Chemistry*, *270*, 11477–11483.

Förster, S., Apostol, L., & Bras, W. (2010). Scatter : software for the analysis of nano- and mesoscale small-angle scattering. *Journal of Applied Crystallography*, *43*, 639–646.

Franke, D., Petoukhov, M. V., Konarev, P. V., Panjkovich, A., Tuukkanen, A., Mertens, H. D. T., … Svergun, D. I. (2017). ATSAS 2.8: A comprehensive data analysis suite for small-angle scattering from macromolecular solutions. *Journal of Applied Crystallography*, *50*, 1212–1225.

Franke, Daniel, & Svergun, D. I. (2009). DAMMIF, a program for rapid ab-initio shape determination in small-angle scattering. *Journal of Applied Crystallography*, *42*, 342–346.

Gadani, S. P., Cronk, J. C., Norris, G. T., & Kipnis, J. (2012). IL-4 in the Brain: A Cytokine To Remember. *The Journal of Immunology*, *189*, 4213–4219.

Gasteiger, E., Hoogland, C., Gattiker, A., Duvaud, S., Wilkins, M. R., Appel, R. D., & Bairoch, A. (2005). Protein Identification and Analysis Tools on the ExPASy Server. In *The Proteomics Protocols Handbook* (pp. 571–607). Humana Press.

Getzoff, E., Geysen, H., Rodda, S., Alexander, H., Tainer, J., & Lerner, R. (1987). Mechanisms of antibody binding to a protein. *Science*, *235*, 1191–1196.

Ghosh, S., & Campbell, A. M. (1986). Multispecific monoclonal antibodies. *Immunology Today*, *7*, 217–222.

Glaeser, R. M. (2016). Specimen Behavior in the Electron Beam. In *Methods in Enzymology* (Vol. 579, pp. 19–50). Academic Press Inc.

Glaeser, R. M. (2018). Proteins, interfaces, and cryo-EM grids. *Current Opinion in Colloid & Interface Science*, *34*, 1–8.

Godar, M., de Haard, H., Blanchetot, C., & Rasser, J. (2018). Therapeutic bispecific antibody formats: a patent applications review (1994-2017). *Expert Opinion on Therapeutic Patents*, *28*, 251–276.

Grant, T., & Grigorieff, N. (2015). Measuring the optimal exposure for single particle cryo-EM using a 2.6 ˚ A reconstruction of rotavirus VP6. *ELife*. https://doi.org/10.7554/eLife.06980.001

Grant, T., Rohou, A., & Grigorieff, N. (2018). cisTEM, user-friendly software for single-particle image processing. *ELife*. https://doi.org/10.7554/eLife.35383.001

Grimm, R., Koster, A. J., Ziese, U., Typke, D., & Baumeister, W. (1996). Zero-loss energy filtering under low-dose conditions using a post-column energy filter. *Journal of Microscopy*, *183*, 60–68.

Hao, Y., Yu, X., Bai, Y., McBride, H. J., & Huang, X. (2019). Cryo-EM Structure of HER2-trastuzumab-pertuzumab complex. *PLOS ONE*, *14*, e0216095.

Harauz, G., & Van Heel, M. (1986). Exact filters for general geometry three dimensional reconstruction. *Optik*, *73*, 146–156.

Heymann, J. B. (2001). Bsoft: Image and molecular processing in electron microscopy. *Journal of Structural Biology*, *133*, 156–169. Academic Press Inc.

Houde, D., Arndt, J., Domeier, W., Berkowitz, S., & Engen, J. R. (2009). Characterization of IgG1 Conformation and conformational dynamics by hydrogen/deuterium exchange mass spectrometry. *Analytical Chemistry*, *81*, 2644–2651.

Hura, G. L., Menon, A. L., Hammel, M., Rambo, R. P., Poole II, F. L., Tsutakawa, S. E., … Tainer, J. A. (2009). Robust, high-throughput solution structural analyses by small angle X-ray scattering (SAXS). *Nature Methods*, *6*, 606–612.

Jain, T., Sheehan, P., Crum, J., Carragher, B., & Potter, C. S. (2012). Spotiton: A prototype for an integrated inkjet dispense and vitrification system for cryo-TEM. *Journal of Structural Biology*, *179*, 68–75.

Jakob, C. G., Edalji, R., Judge, R. A., DiGiammarino, E., Li, Y., Gu, J., & Ghayur, T. (2013). Structure reveals function of the dual variable domain immunoglobulin (DVD-Ig^{TM}) molecule. *MAbs*, *5*, 358–363.

Jakobi, A. J., Wilmanns, M., & Sachse, C. (2017a). Model-based local density sharpening of cryo-EM maps. *ELife*, *6*. https://doi.org/10.7554/eLife.27131

Jakobi, A. J., Wilmanns, M., & Sachse, C. (2017b). Model-based local density sharpening of cryo-EM maps. *ELife*, *6*. https://doi.org/10.7554/eLife.27131

Jarmoskaite, I., Alsadhan, I., Vaidyanathan, P. P., & Herschlag, D. (2020). How to measure and evaluate binding affinities. *ELife*, *9*, 1–34.

Jeffries, C. M., Graewert, M. A., Svergun, D. I., & Blanchet, C. E. (2015). Limiting radiation damage for high-brilliance biological solution scattering: Practical experience at the EMBL P12 beamline PETRAIII. *Journal of Synchrotron Radiation*, *22*, 273–279. International Union of Crystallography.

Johnson, M., Zaretskaya, I., Raytselis, Y., Merezhuk, Y., McGinnis, S., & Madden, T. L. (2008). NCBI BLAST: a better web interface. *Nucleic Acids Research*, *36*, 5–9.

Joseph, A. P., Malhotra, S., Burnley, T., Wood, C., Clare, D. K., Winn, M., & Topf, M. (2016). Refinement of atomic models in high resolution EM reconstructions using Flex-EM and local assessment. *Methods*, *100*, 42–49.

Kandiah, E., Giraud, T., Antolinos, A. de M., Dobias, F., Effantin, G., Flot, D., … Mueller-Dieckmann, C. (2019). CM01: A facility for cryo-electron microscopy at the European synchrotron. *Acta Crystallographica Section D: Structural Biology*, *75*, 528–535.

Kaplon, H., & Reichert, J. M. (2018). Antibodies to watch in 2018. *MAbs*, *10*, 183–203.

Kimanius, D., Forsberg, B. O., Scheres, S. H. W., & Lindahl, E. (2016). Accelerated cryo-EM structure determination with parallelisation using GPUS in RELION-2. *ELife*, *5*. https://doi.org/10.7554/eLife.18722

Klein, C., Schaefer, W., & Regula, J. T. (2016). The use of CrossMAb technology for the generation of bi- and multispecific antibodies. *MAbs*, *8*, 1010–1020.

Koch, M. H. J., Vachette, P., & Svergun, D. I. (2003, May). Small-angle scattering: A view on the properties, structures and structural changes of biological macromolecules in solution. *Quarterly Reviews of Biophysics*, Vol. 36, pp. 147–227. Q Rev Biophys.

Kontermann, R. E., & Brinkmann, U. (2015). Bispecific antibodies. *Drug Discovery Today*, *20*, 838–847.

Kucukelbir, A., Sigworth, F. J., & Tagare, H. D. (2014a). Quantifying the local resolution of cryo-EM density maps. *Nature Methods*, *11*, 63–65.

Kucukelbir, A., Sigworth, F. J., & Tagare, H. D. (2014b). Quantifying the local resolution of cryo-EM density maps. *Nature Methods*, *11*, 63–65.

Kühlbrandt, W. (2014, March 28). The resolution revolution. *Science*, Vol. 343, pp. 1443–1444. American Association for the Advancement of Science.

Lee, C. C., Perchiacca, J. M., & Tessier, P. M. (2013, November). Toward aggregation-resistant antibodies by design. *Trends in Biotechnology*, Vol. 31, pp. 612–620.

Leong, A. S.-Y., & Cooper, K. (2003). *Manual of Diagnostic Antibodies for Immunohistology* (2nd ed.). Greenwich Medical Media, Ltd.

Li, W., Prabakaran, P., Chen, W., Zhu, Z., Feng, Y., & Dimitrov, D. (2016). Antibody Aggregation: Insights from Sequence and Structure. *Antibodies*, *5*, 19.

Li, X., Mooney, P., Zheng, S. Q., Booth, C. R., Braunfeld, M. B., Gubbens, S., … Cheng, Y. (2013). Electron counting and beam-induced motion correction enable near-atomic-resolution single-particle cryo-EM. *Nature Methods*, *10*, 584–590.

Ma, C., Bendory, T., Boumal, N., Sigworth, F., & Singer, A. (2019). *Heterogeneous multireference alignment for images with application to 2-D classification in single particle reconstruction*.

Market, E., & Papavasiliou, F. N. (2003). V(D)J recombination and the evolution of the adaptive immune system. *PLoS Biology*, *1*, E16.

Martin, T. G., Boland, A., Fitzpatrick, A. W. P., & Scheres, S. H. W. (2016). Graphene Oxide Grid Preparation.

Mastronarde, D. N. (2003). SerialEM: A Program for Automated Tilt Series Acquisition on Tecnai Microscopes Using Prediction of Specimen Position. *Microscopy and Microanalysis*, *9*, 1182–1183.

Mastronarde, D. N. (2018). Advanced Data Acquisition From Electron Microscopes With SerialEM. *Microscopy and Microanalysis*, *24*, 864–865.

Maverakis, E., Kim, K., Shimoda, M., Gershwin, M. E., Patel, F., Wilken, R., … Lebrilla, C. B. (2015). Glycans in the immune system and The Altered Glycan Theory of Autoimmunity: a critical review. *Journal of Autoimmunity*, *57*, 1–13.

Merk, A., Bartesaghi, A., Banerjee, S., Falconieri, V., Rao, P., Davis, M. I., … Subramaniam, S. (2016). Breaking Cryo-EM Resolution Barriers to Facilitate Drug Discovery. *Cell*, *165*, 1698–1707.

Milazzo, A.-C., Cheng, A., Moeller, A., Lyumkis, D., Jacovetty, E., Polukas, J., … Potter, C. S. (2011). Initial evaluation of a direct detection device detector for single particle cryo-electron microscopy. *Journal of Structural Biology*, *176*, 404–408.

Milstein, C., & Cuello, A. C. (1983). Hybrid hybridomas and their use in immunohistochemistry. *Nature*, *305*, 537–540.

Mindell, J. A., & Grigorieff, N. (2003). Accurate determination of local defocus and specimen tilt in electron microscopy. *Journal of Structural Biology*, *142*, 334–347.

Mueller, T. D., Zhang, J. L., Sebald, W., & Duschl, A. (2002, November 11). Structure, binding, and antagonists in the IL-4/IL-13 receptor system. *Biochimica et Biophysica Acta - Molecular Cell Research*, Vol. 1592, pp. 237–250. Elsevier.

Nagayama, K., & Danev, R. (2009). Phase-plate electron microscopy: a novel imaging tool to reveal close-to-life nano-structures. *Biophysical Reviews*, *1*, 37–42.

Oh, C. K., Geba, G. P., & Molfino, N. (2010, March 1). Investigational therapeutics targeting the IL-4/IL-13/STAT-6 pathway for the treatment of asthma. *European Respiratory Review*, Vol. 19, pp. 46–54. European Respiratory Society.

Owen, J., Punt, J., & Stranford, S. (2013). *Kuby Immunology. 7th Edition* (7th ed.). New York: W.H. Freeman and Company.

Oyen, D., Torres, J. L., Cottrell, C. A., Richter King, C., Wilson, I. A., & Ward, A. B. (2018). Cryo-EM structure of P. falciparum circumsporozoite protein with a vaccine-elicited antibody is stabilized by somatically mutated inter-Fab contacts. In *Sci. Adv* (Vol. 4). Retrieved from http://advances.sciencemag.org/

Palovcak, E., Wang, F., Zheng, S. Q., Yu, Z., Li, S., Bulkley, D., … Cheng, Y. (2018). A simple and robust procedure for preparing graphene-oxide cryo-EM grids. *BioRxiv*. https://doi.org/10.1101/290197

Pancer, Z., & Cooper, M. D. (2006). THE EVOLUTION OF ADAPTIVE IMMUNITY. *Annual Review of Immunology*, *24*, 497–518.

Pernot, P., Round, A., Barrett, R., De Maria Antolinos, A., Gobbo, A., Gordon, E., … McSweeney, S. (2013). Upgraded ESRF BM29 beamline for SAXS on macromolecules in solution. *Journal of Synchrotron Radiation*, *20*, 660–664.

Pettersen, E. F., Goddard, T. D., Huang, C. C., Couch, G. S., Greenblatt, D. M., Meng, E. C., & Ferrin, T. E. (2004). UCSF Chimera - A visualization system for exploratory research and analysis. *Journal of Computational Chemistry*, *25*, 1605–1612.

Popovic, B., Breed, J., Rees, D. G., Gardener, M. J., Vinall, L. M. K., Kemp, B., … May, R. D. (2017). Structural Characterisation Reveals Mechanism of IL-13-Neutralising Monoclonal Antibody Tralokinumab as Inhibition of Binding to IL-13Rα1 and IL-13Rα2. *Journal of Molecular Biology*, *429*, 208–219.

Punjani, A., Rubinstein, J. L., Fleet, D. J., & Brubaker, M. A. (2017). cryoSPARC: algorithms for rapid unsupervised cryo-EM structure determination. *Nature Methods*, *14*, 290–296.

Rambo, R. P., & Tainer, J. A. (2011). Characterizing flexible and intrinsically unstructured biological macromolecules by SAS using the Porod-Debye law. *Biopolymers*, *95*, 559–571.

Ridgway, J. B. B., Presta, L. G., & Carter, P. (1996). ‘Knobs-into-holes’ engineering of antibody C $_H$ 3 domains for heavy chain heterodimerization. *“Protein Engineering, Design and Selection,”* *9*, 617–621.

Riechmann, L., Clark, M., Waldmann, H., & Winter, G. (1988). Reshaping human antibodies for therapy. *Nature*, *332*, 323–327.

Rohou, A., & Grigorieff, N. (2015). CTFFIND4: Fast and accurate defocus estimation from electron micrographs. *Journal of Structural Biology*, *192*, 216–221.

Rosenthal, P. B., & Henderson, R. (2003). Optimal determination of particle orientation, absolute hand, and contrast loss in single-particle electron cryomicroscopy. *Journal of Molecular Biology*, *333*, 721–745.

Russo, C. J., & Passmore, L. A. (2014). Controlling protein adsorption on graphene for cryo-EM using low-energy hydrogen plasmas. *Nature Methods*, *11*, 649–652.

Sandin, S., Öfverstedt, L. G., Wikström, A. C., Wrange, Ö., & Skoglund, U. (2004). Structure and flexibility of individual immunoglobulin G molecules in solution. *Structure*, *12*, 409–415.

Scheres, S. H. W. (2012). RELION: Implementation of a Bayesian approach to cryo-EM structure determination. *Journal of Structural Biology*, *180*, 519–530.

Scheres, S. H. W. (2016). Processing of Structurally Heterogeneous Cryo-EM Data in RELION. In *Methods in Enzymology* (1st ed., Vol. 579). Elsevier Inc.

Scheres, S. H. W., & Chen, S. (2012). Prevention of overfitting in cryo-EM structure determination. *Nature Methods*, *9*, 853–854.

Sigworth, F. J. (2016). Principles of cryo-EM single-particle image processing. *Microscopy*, *65*, 57–67.

Simonetti, A., Marzi, S., Myasnikov, A. G., Fabbretti, A., Yusupov, M., Gualerzi, C. O., & Klaholz, B. P. (2008). Structure of the 30S translation initiation complex. *Nature*, *455*, 416–420.

Smyth, M. S., & Martin, J. H. J. (2000). x Ray crystallography. *Journal of Clinical Pathology - Molecular Pathology*, Vol. 53, pp. 8–14. BMJ Publishing Group.

Sonn-Segev, A., Belacic, K., Bodrug, T., Young, G., VanderLinden, R. T., Schulman, B. A., … Kukura, P. (2020). Quantifying the heterogeneity of macromolecular machines by mass photometry. *Nature Communications*, *11*, 1–10.

Steinmetz, A., Vallée, F., Beil, C., Lange, C., Baurin, N., Beninga, J., … Rao, E. (2016). CODV-Ig, a universal bispecific tetravalent and multifunctional immunoglobulin format for medical applications. *MAbs*, *8*, 867–878.

Stella, S., Mesa, P., Thomsen, J., Paul, B., Alcón, P., Jensen, S. B., … Montoya, G. (2018). Conformational Activation Promotes CRISPR-Cas12a Catalysis and Resetting of the Endonuclease Activity. *Cell*, *175*, 1856-1871.e21.

Suzuki, A., Leland, P., Joshi, B. H., & Puri, R. K. (2015). Targeting of IL-4 and IL-13 receptors for cancer therapy. *Cytokine*, *75*, 79–88.

Tang, G., Peng, L., Baldwin, P. R., Mann, D. S., Jiang, W., Rees, I., & Ludtke, S. J. (2007). EMAN2: An extensible image processing suite for electron microscopy. *Journal of Structural Biology*, *157*, 38–46.

Tegunov, D., & Cramer, P. (2018). Real-time cryo-EM data pre-processing with Warp. *BioRxiv*, 338558.

Thompson, R. F., Walker, M., Siebert, C. A., Muench, S. P., & Ranson, N. A. (2016). An introduction to sample preparation and imaging by cryo-electron microscopy for structural biology. *Methods*, *100*, 3–15.

Tian, X., Vestergaard, B., Thorolfsson, M., Yang, Z., Rasmussen, H. B., & Langkilde, A. E. (2015). In-depth analysis of subclass-specific conformational preferences of IgG antibodies. *IUCrJ*, *2*, 9–18.

Ultsch, M., Bevers, J., Nakamura, G., Vandlen, R., Kelley, R. F., Wu, L. C., & Eigenbrot, C. (2013). Structural basis of signaling blockade by anti-IL-13 antibody Lebrikizumab. *Journal of Molecular Biology*, *425*, 1330–1339.

Van Heel, M., & Schatz, M. (2005). Fourier shell correlation threshold criteria. *Journal of Structural Biology*, *151*, 250–262.

Verhoeyen, M., Milstein, C., & Winter, G. (1988). Reshaping human antibodies: grafting an antilysozyme activity. *Science*, *239*, 1534–1536.

Vidarsson, G., Dekkers, G., & Rispens, T. (2014). IgG subclasses and allotypes: From structure to effector functions. *Frontiers in Immunology*, *5*, 520.

Viganò, E., Gunawardana, J., Mottok, A., Van Tol, T., Mak, K., Chan, F. C., … Steidl, C. (2018). Somatic IL4R mutations in primary mediastinal large B-cell lymphoma lead to constitutive JAK-STAT signaling activation. *Blood*, *131*, 2036–2046.

Voss, N. R., Yoshioka, C. K., Radermacher, M., Potter, C. S., & Carragher, B. (2009). DoG Picker and TiltPicker: Software tools to facilitate particle selection in single particle electron microscopy. *Journal of Structural Biology*, *166*, 205–213.

Wagner, T., Merino, F., Stabrin, M., Moriya, T., Gatsogiannis, C., & Raunser, S. (2018). SPHIRE-crYOLO: A fast and well-centering automated particle picker for cryo-EM. *BioRxiv*, 356584.

Walford, H. H., & Doherty, T. A. (2013). STAT6 and lung inflammation. *JAK-STAT*, *2*, e25301.

Walter, M. R., Cook, W. J., Zhao, B. G., Cameron, R. P., Ealick, S. E., Walter, R. L., … Bugg, C. E. (1992). Crystal structure of recombinant human interleukin-4. *The Journal of Biological Chemistry*, *267*, 20371–20376.

Watanabe, Y., & Inoko, Y. (2009). Size-exclusion chromatography combined with small-angle X-ray scattering optics. *Journal of Chromatography A*, *1216*, 7461–7465.

Waterhouse, A., Bertoni, M., Bienert, S., Studer, G., Tauriello, G., Gumienny, R., … Schwede, T. (2018). SWISS-MODEL: Homology modelling of protein structures and complexes. *Nucleic Acids Research*, *46*, W296–W303.

Weiner, G. J. (2015). Building better monoclonal antibody-based therapeutics. *Nature Reviews Cancer*, *15*, 361–370.

Weir, A. N. C., Nesbitt, A., Chapman, A. P., Popplewell, A. G., Antoniw, P., & Lawson, A. D. G. (2002). Formatting antibody fragments to mediate specific therapeutic functions. *Biochemical Society Transactions*, *30*, 512–516.

Williams, C. J., Headd, J. J., Moriarty, N. W., Prisant, M. G., Videau, L. L., Deis, L. N., … Richardson, D. C. (2018). MolProbity: More and better reference data for improved all-atom structure validation. *Protein Science*, *27*, 293–315.

Williams, D. B., & Carter, C. B. (1996). The Transmission Electron Microscope. In *Transmission Electron Microscopy* (pp. 3–17). Boston, MA: Springer US.

Williams, R. C. (1977). Use of polylysine for adsorption of nucleic acids and enzymes to electron microscope specimen films. *Proceedings of the National Academy of Sciences of the United States of America*, *74*, 2311–2315.

Winn, M. D., Murshudov, G. N., & Papiz, M. Z. (2003). Macromolecular TLS Refinement in REFMAC at Moderate Resolutions. *Methods in Enzymology*, *374*, 300–321.

Wittel, U. A., Goel, A., Varshney, G. C., & Batra, S. K. (2001). Mucin antibodies - New tools in diagnosis and therapy of cancer. *Frontiers in Bioscience*, *6*, 1296–1310.

Wood, C., Burnley, T., Patwardhan, A., Scheres, S. H. W., Topf, M., Roseman, A., & Winn, M. (2015). Collaborative computational project for electron cryo-microscopy. *Acta Crystallographica Section D: Biological Crystallography*, *71*, 123–126.

Wu, C., Ying, H., Grinnell, C., Bryant, S., Miller, R., Clabbers, A., … Ghayur, T. (2007). Simultaneous targeting of multiple disease mediators by a dual-variable-domain immunoglobulin. *Nature Biotechnology*, *25*, 1290–1297.

Young, G., Hundt, N., Cole, D., Fineberg, A., Andrecka, J., Tyler, A., … Kukura, P. (2018). Quantitative mass imaging of single biological macromolecules. *Science*, *360*, 423–427.

Zhang, K. (2016). Gctf: Real-time CTF determination and correction. *Journal of Structural Biology*, *193*, 1–12.

Zhang, K. (2018). *Brief Manual of Gautomatch Features*.

Zhang, X., Zhang, L., Tong, H., Peng, B., Rames, M. J., Zhang, S., & Ren, G. (2015). 3D Structural Fluctuation of IgG1 Antibody Revealed by Individual Particle Electron Tomography. *Scientific Reports*, *5*, 1–14.

Zheng, S. Q., Palovcak, E., Armache, J.-P., Verba, K. A., Cheng, Y., & Agard, D. A. (2017). MotionCor2: anisotropic correction of beam-induced motion for improved cryo-electron microscopy. *Nature Methods*, *14*, 331–332.

Zivanov, J., Nakane, T., Forsberg, B., Kimanius, D., Hagen, W. J. H., Lindahl, E., & Scheres, S. H. W. (2018). RELION-3: new tools for automated high-resolution cryo-EM structure determination. *BioRxiv*, 421123.

7. Annex

7.1 Affinity chromatography of TBTI-IL4

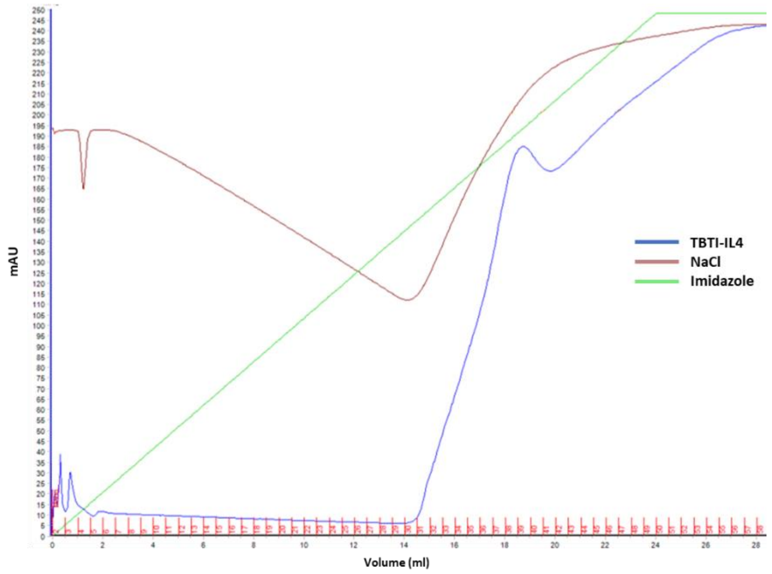

Figure 7.1: Ni-NTA affinity chromatography of TBTI-IL4. TBTI-IL4 (in blue) elutes at around the 375 mM imidazole (green) concentration mark, or 75% of the total gradient.

7.2 SPR over-time antigen dissociation curves

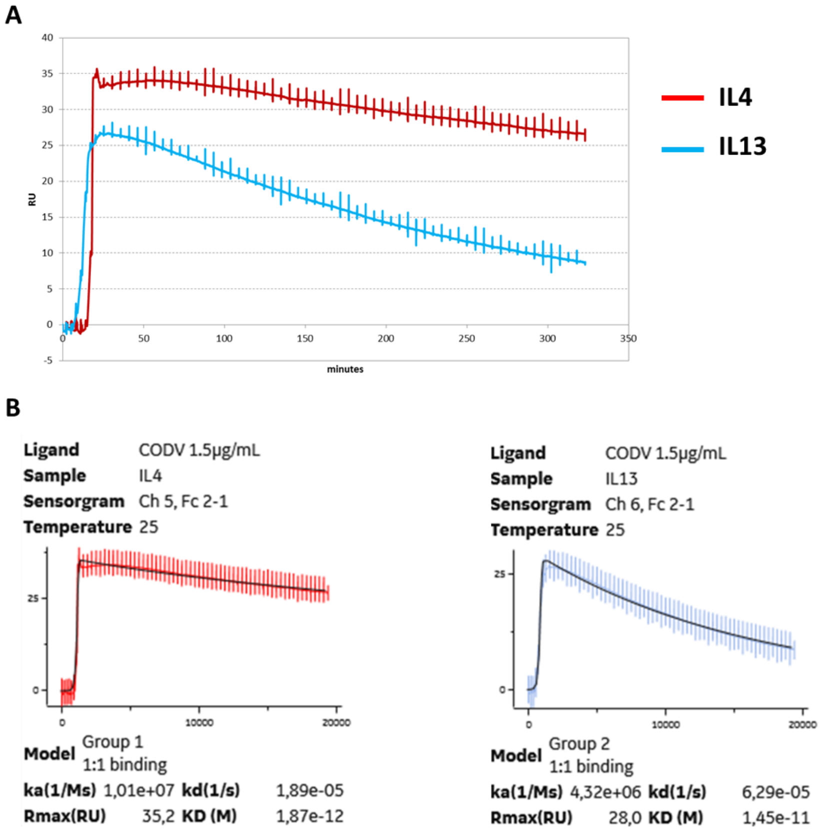

Ligand CODV 1.5µg/mL
Sample IL4
Sensorgram Ch 5, Fc 2-1
Temperature 25

Model Group 1 1:1 binding
ka(1/Ms) 1,01e+07 **kd(1/s)** 1,89e-05
Rmax(RU) 35,2 **KD (M)** 1,87e-12

Ligand CODV 1.5µg/mL
Sample IL13
Sensorgram Ch 6, Fc 2-1
Temperature 25

Model Group 2 1:1 binding
ka(1/Ms) 4,32e+06 **kd(1/s)** 6,29e-05
Rmax(RU) 28,0 **KD (M)** 1,45e-11

Figure 7.2: Alternative method for determining binding parameters of IL4 and IL13 to CODV by SPR. (A) Ligands were flowed into individual flow cells with CODV, until saturation was reached. After that, flow of ligands was stopped, and response was measured over 5 hours. **(B)** Using the antigen dissociation rates over time, binding parameters could be measured, 1.87 pM for IL4 (red) and 14.5 pM for IL13 (blue).

7.3 Tables of all the vitrification conditions tested

Apo-CODV

CODV	Grid type		Glow Discharge		Vitrobot			Sample		
Try nº	**Grid**	**Support**	**Time (s) + Polarity**	**Voltage (mA)**	**Blot Force**	**Blot Time (s)**	**Wait Time (s)**	**Concentration (µg/ml)**	**Volume (µl)**	**Other**
1	Cu 400	QF 1.2/1.3	30 NEG	25	-14	1.5	20	150	3.5	PBS pH 7.2 (Default), 4C (Default)
2	Cu 400	QF 1.2/1.3	30 NEG	25	-14	1.5	20	300	3.5	PBS
3	Cu 300	QF 2/1	30 NEG	25	-14	1.5	20	150	3.5	PBS
4	Cu 300	QF 2/1	30 NEG	25	-14	1.5	20	300	3.5	PBS
5	Cu 300	QF 2/2	30 NEG	25	-14	2.5	20	150	3.5	PBS
6	Cu 300	QF 2/2	30 NEG	25	-14	2.5	20	300	3.5	PBS
7	Cu 400	QF 1.2/1.3	30 POS	25	-14	2.5	20	500	3.5	PBS
8	Cu 300	QF 2/1	30 POS	25	-14	2.5	20	500	3.5	PBS
9	Cu 400	QF 1.2/1.3	40 POS	25	-14	2.5	20	1290	3.5	PBS
10	Cu 300	QF 2/1	40 POS	25	-14	2.5	20	1290	3.5	PBS
11	Cu 300	QF 2/1	90 NEG	25	-8	2	10	1290	4.1	PBS, 22C
12	Cu 300	QF 2/1	90 NEG	25	-8	2	10	1290	3.5	PBS, 22C
13	Cu 300	QF 2/1	90 NEG	25	-8	2	10	1290	3.5	PBS 22C
14	Cu 300	QF 2/1	90 NEG	25	-14	2.5	10	1290	3.5	PBS 22C
15	Cu 400	QF 1.2/1.3	60 POS	25	0	2	10	300	3.5	PBS
16	Cu 400	QF 1.2/1.3	60 POS	25	0	2	10	600	3.5	PBS
17	Cu 400	QF 1.2/1.3	40 NEG	25	0	2	30	1290	3.5	PBS
18	Cu 400	QF 1.2/1.3	40 NEG	25	0	2	30	600	3.5	PBS
19	Cu 400	QF 1.2/1.3	40 NEG	25	0	3	30	1290	3.5	PBS
20	Cu 400	QF 1.2/1.3	40 NEG	25	4	1.5	30	600	3.5	PBS
21	Cu 400	QF 1.2/1.3	40 NEG	25	4	1.5	30	1290	3.5	PBS
22	Cu 400	QF 1.2/1.3	40 NEG	25	4	1.5	20	500	3.5	HEPES
23	Cu 400	QF 1.2/1.3	40 NEG	25	4	1.5	20	910	3.5	HEPES
24	Cu 300	2nm C 1.2/1.3	40 NEG	25	4	1.5	30	910	3.5	HEPES
25	Cu 300	SiO2 1.2/1.3	40 NEG	25	-8	2	10	910	2.5	HEPES
26	Cu 300	2nm C 1.2/1.4	40 NEG	25	4	1.5	30	910	3.5	HEPES
27	Cu 300	SiO2 1.2/1.4	40 NEG	25	-8	2	10	910	2.5	HEPES
28	Cu 400	QF 1.2/1.3	40 NEG	25	4	2	0	500	3.5	HEPES
29	Cu 400	QF 1.2/1.3	40 NEG	25	4	2	0	500	3.5	HEPES 1 mM DTT
30	Cu 400	QF 1.2/1.3	40 NEG	25	4	2	0	200	3.5	HEPES
31	Cu 300	Lacey Carbon	40 NEG	25	4	2	0	500	3.5	HEPES
32	Cu 400	QF 1.2/1.3	40 NEG	25	4	2	0	400	3.5	HEPES 1.5 mM DTT
33	Cu 400	QF 1.2/1.3	40 NEG	25	4	2	0	400	3.5	HEPES 2 mM DTT
34	Au 300	C-Flat 2/1	40 NEG	25	4	2	0	400	3.5	HEPES 1 mM DTT
35	Cu 300	Lacey Carbon	40 NEG	25	4	2	0	400	3.5	HEPES 1 mM DTT
36	Au 200	QF 2/1	40 NEG	25	-2	3	0	300	3.5	HEPES 1 mM DTT
37	Au 300	C-Flat 2/1	40 NEG	25	-2	3	0	300	3.5	HEPES 1 mM DTT
38	Cu 400	QF 1.2/1.3	60 NEG	25	-2	3	0	300	3.5	HEPES 1 mM DTT
39	Cu 300	Lacey Carbon	40 NEG	25	-2	3	0	300	3.5	HEPES 1 mM DTT
40	Au 300	C-Flat 2/1	90 PLASMA	25	-2	3	0	200	3.5	HEPES 1 mM DTT
41	Au 300	C-Flat 2/1	90 PLASMA	25	-10	2.5	0	200	3.5	HEPES 1 mM DTT
42	Au 300	C-Flat 2/1	90 PLASMA	25	-2	3	0	250	3.5	HEPES 1 mM DTT
43	Au 300	C-Flat 2/1	90 PLASMA	25	-10	2.5	0	250	3.5	HEPES 1 mM DTT
44	Au 300	C-Flat 2/1	40 NEG X2	25	-2	3	0	250	3.5	HEPES 1 mM DTT
45	Au 300	C-Flat 2/1	40 NEG X2	25	-2	3	0	250	3.5	HEPES 0.67 mM DTT
46	Au 300	C-Flat 2/1	40 NEG X2	25	-2	3	0	200	3.5	HEPES 1 mM DTT
47	Au 300	C-Flat 2/1	40 NEG X2	25	-2	3	0	200	3.5	HEPES 0.67 mM DTT
48	Au 300	C-Flat 2/1	40 NEG X2	25	-2	3	0	250	3.5	N/A (Control)
49	Au 300	C-Flat 2/1	40 NEG X2	25	-2	3	0	200	3.5	N/A (Control)
50	Au 200	UltrAuFoil 2/2	40 NEG	25	-2	3	0	250	3.5	HEPES 1 mM DTT
51	Au 300	UltrAuFoil 1.2/1.3	40 NEG	25	-2	3	0	250	3.5	HEPES 1 mM DTT
52	Au 300	C-Flat 2/1	40 NEG	25	-2	3	0	300	3.5	HEPES 1 mM DTT
53	Au 300	C-Flat 2/1	40 NEG	25	-2	3	0	250	3.5	HEPES 0.02% DDM
54	Au 300	UltrAuFoil 1.2/1.3	30 NEG	28	-10	2	0	250	3.5	HEPES 0.003% DDM
55	Au 300	UltrAuFoil 1.2/1.3	30 NEG	28	-10	2	0	250	3.5	HEPES 0.02% DDM
56	Au 300	UltrAuFoil 1.2/1.3	30 NEG	28	-10	2	0	250	3.5	HEPES 1 mM DTT
57	Au 300	UltrAuFoil 1.2/1.3	30 NEG	28	-20	4	0	250	3.5	HEPES
58	Cu 400	C-Flat 2/1	30 NEG	28	-2	3	0	200	3.5	HEPES 0.54 mM DTT
59	Cu 400	C-Flat 2/1	30 NEG	28	-2	3	0	200	3.5	HEPES 0.54 mM DTT
60	Cu 400	C-Flat 2/1	30 NEG	28	-2	3	0	200	3.5	HEPES 1 mM DTT
61	Cu 400	C-Flat 2/1	30 NEG	28	-2	3	0	200	3.5	HEPES 1 mM DTT
62	Au 300	QF 2/1	40 NEG	28	-2	3	0	200	3.5	HEPES 0.54 mM DTT
63	Au 300	C-Flat 2/1	30 NEG	7	-2	2.5	0	150	3	TBS
64	Au 300	C-Flat 2/1	30 NEG	7	-2	3	0	150	3	TBS
65	Au 300	C-Flat 2/1	30 NEG	7	-2	3.5	0	150	3	TBS
66	Au 300	C-Flat 2/1	30 NEG	7	-2	4	0	150	3	TBS
67	Au 300	C-Flat 2/1	30 NEG	7	-2	3	0	150	2	TBS
68	Au 300	C-Flat 2/1	30 NEG	7	-2	3	0	150	4	TBS
69	Au 300	QF 2/1	30 NEG	28	0	4.5	0	175	3	TBS + 0.06 mM DDM
70	Au 300	QF 2/1	30 NEG	28	0	4.5	0	175	3	TBS + 0.03 mM DDM
71	Au 300	C-Flat 2/1	30 NEG	7	0	4.5	0	150	4	TBS + 0.06 mM DDM
72	Au 300	C-Flat 2/1	30 NEG	7	0	4.5	0	150	4	TBS + 0.03 mM DDM
73	Au 300	C-Flat 2/1	30 NEG	7	0	4.5	0	175	4	TBS + 0.06 mM DDM
74	Au 300	C-Flat 2/1	30 NEG	7	0	4.5	0	175	4	TBS + 0.03 mM DDM
75	Au 300	C-Flat 2/1	30 NEG	7	0	4.5	0	175	4	TBS + 0.06 mM DDM + 1 mM DTT
76	Au 300	C-Flat 2/1	60 NEG	7	0	4.5	0	175	4	TBS + 0.06 mM DDM
77	Au 300	C-Flat 2/1	45 NEG	7	0	4.5	0	175	4	TBS + 0.06 mM DDM
78	Au 300	C-Flat 2/1	30 NEG	7	4	4.5	0	175	4	TBS + 0.06 mM DDM
79	Au 300	C-Flat 2/1	30 NEG	7	-10	4.5	0	175	4	TBS + 0.06 mM DDM
80	Au 300	C-Flat 2/1	30 NEG	7	0	4	0	175	4	TBS + 0.06 mM DDM

81	Au 300	C-Flat 2/1	30 NEG	7	0	4.5	0	175	8 (Both sides)	TBS + 0.06 mM DDM
82	Au 300	C-Flat 2/1	30 NEG	7	0	4.5	0	175	4	TBS + 0.045 mM DDM
83	Au 300	C-Flat 2/1	30 NEG	7	0	4.5	0	150	4	TBS + 0.045 mM DDM
84	Au 300	C-Flat 2/1	30 NEG	7	0	4.5	0	175	4	Citrate pH 6 dialysis
85	Au 300	C-Flat 2/1	30 NEG	7	0	4.5	0	175	4	Citrate pH 6 concentration
86	Au 300	C-Flat 2/1	30 NEG	7	0	4.5	0	175	4	NaAc pH 5.2 dialysis
87	Au 300	C-Flat 2/1	30 NEG	7	0	4.5	0	175	4	NaAc pH 5.2 concentration
88	Au 300	C-Flat 2/1	30 NEG	7	0	4.5	0	175	4	Citrate ph6 concentration + 0.03 mM DDM
89	Au 300	C-Flat 2/1	30 NEG	7	0	4.5	0	175	4	NaAc pH 5.2 concentration + 0.03 mM DDM
90	Au 300	C-Flat 2/1 + GO	30 NEG	7	0	4.5	0	175	4	TBS + 0.06 mM DDM
91	Au 300	C-Flat 2/1 + GO	30 NEG	7	0	4.5	0	175	4	PBS + 0.03 mM DDM
92	Au 300	C-Flat 2/1 + GO	30 NEG	7	0	4.5	0	175	4	TBS + 0.03 mM DDM
93	Au 300	C-Flat 2/1 + GO	30 NEG	7	0	4.5	0	175	4	Citrate ph6 concentration + 0.03 mM DDM
94	Au 300	C-Flat 2/1	30 NEG	7	0	5	0	175	3	PBS + 0.03 mM DDM
95	Au 300	C-Flat 2/1	30 NEG	7	0	5	0	175	3	TBS + 0.03 mM DDM
96	Au 300	C-Flat 2/1 + GO	30 NEG	7	0	4.5	0	15	4	DPBS + 0.03 mM DDM
97	Au 300	C-Flat 2/1 + GO	30 NEG	7	0	4.5	0	30	4	DPBS + 0.03 mM DDM
98	Au 300	C-Flat 2/1 + GO	30 NEG	7	0	4.5	0	60	4	DPBS + 0.03 mM DDM
99	Au 300	C-Flat 2/1	30 NEG	7	0	4.5	0	200	4	Malic Acid 5.3 + 0.03 mM DDM
100	Au 300	C-Flat 2/1	30 NEG	7	0	4.5	0	200	4	Succinic Acid 5.4 + 0.03 mM DDM
101	Au 400	C-Flat 2/1 + GO	30 NEG	7	0	4.5	0	10	4	DPBS + 0.03 mM DDM
102	Au 400	C-Flat 2/1 + GO	30 NEG	7	0	4.5	0	10	4	DPBS
103	Au 400	C-Flat 2/1	30 NEG	7	0	4.5	0	150	4	Histidine pH 6
104	Au 400	C-Flat 2/1	30 NEG	7	0	4.5	0	150	4	DPBS + 1% Sucrose
105	Cu 300	QF 2/1 + GO	45 NEG	7	0	4.5	0	15	4	DPBS pH 7.2 + 0.03 mM DDM
106	Au 400	C-Flat 2/1	30 NEG	7	0	4.5	0	175	4	Histidine pH 6
107	Au 400	C-Flat 2/1	30 NEG	7	0	4.5	0	175	4	Histidine pH 6 + Trehalose 1%
108	Au 400	C-Flat 2/1	30 NEG	7	0	4.5	0	175	4	Histidine pH 6 + Trehalose 1% + 0.03 mM DDM
109	Au 400	C-Flat 2/1	30 NEG	7	0	4.5	0	175	4	Histidine pH 6 + 0.01 % NP-40
110	Au 300	C-Flat 2/1	30 NEG	7	0	4	0	125	4	Histidine pH 6 + Trehalose 1% + 0.03 mM DDM

Figure 7.4: List of all vitrification conditions tested on Apo-CODV.

CODV-IL4

IL4	**Grid type**		**Glow Discharge**		**Vitrobot**			**Sample**		
Try nº	**Grid**	**Support**	**Time (s) + Polarity**	**Voltage (mA)**	**Blot Force**	**Blot Time (s)**	**Wait Time (s)**	**Concentration (μg/ml)**	**Volume (μl)**	**Other**
1	Au 300	C-Flat 2/1	40 NEG	25	-2	3	0	240	3.5	TBS pH 7.4
2	Au 300	C-Flat 2/1	40 NEG	25	-2	3	0	220	3.5	TBS pH 7.4, 1 mM DTT
3	Au 300	C-Flat 2/1	30 NEG	7	0	4.5	0	175	4	TBS pH 8 (default) + 0.03 mM DDM
4	Au 300	C-Flat 2/1	30 NEG	7	0	4.5	0	150	4	TBS + 0.03 mM DDM
5	Au 400	C-Flat 2/1	30 NEG	7	0	4.5	0	150	4	TBS + 0.03 mM DDM
6	Au 400	C-Flat 2/1	30 NEG	7	0	4.5	0	150	4	TBS + 0.03 mM DDM + Trehalose 1%
8	Au 300	C-Flat 2/1	30 NEG	7	0	4	0	150	4	TBS + 0.03 mM DDM
10	Au 400	QF 2/1 + GO	45 NEG	25	0	4.5	0	50	4	TBS + 0.03 mM DDM
11	Au 400	QF 2/1 + GO	45 NEG	25	0	4.5	0	25	4	TBS + 0.03 mM DDM
12	Au 300	C-Flat 2/1	10 NEG	7	0	6	0	150	4	TBS + 0.06 mM DDM
13	Au 300	C-Flat 2/1	10 NEG	7	0	6	0	150	3	TBS + 0.06 mM DDM
14	Au 300	C-Flat 2/1	10 NEG	7	0	4.5	0	125	4	TBS + 0.06 mM DDM
15	Au 300	C-Flat 2/1	10 NEG	7	0	4.5	0	125	3	TBS + 0.06 mM DDM
16	Au 300	C-Flat 2/1	10 NEG	7	0	4.5	0	175	4	TBS + 0.03 mM DDM (TILTED)
17	Au 300	C-Flat 2/1	10 NEG	7	0	4.5	0	150	4	TBS + 0.03 mM DDM (TILTED)
18	Au 300	C-Flat 2/1	10 NEG	7	0	4.5	0	175	4	TBS + 0.03 mM DDM
19	Au 300	C-Flat 2/1	10 NEG	7	0	6	0	300	4	TBS + 0.03 mM DDM
20	Au 300	C-Flat 1.2/1.3	10 NEG	7	0	4.5	0	175	4	TBS + 0.03 mM DDM
21	Au 300	C-Flat 1.2/1.3	10 NEG	7	0	5	10	300	4	TBS + 0.03 mM DDM
22	Au 300	UltrAuFoil 1.2/1.3	40 NEG	25	0	4.5	0	175	4	TBS + 0.03 mM DDM
23	Au 300	UltrAuFoil 1.2/1.3	40 NEG	25	0	6	0	300	4	TBS + 0.03 mM DDM
24	Au 300	C-Flat 2/1	10 NEG	7	0	2x 4.5	0	175	2x 4	TBS + 0.03 mM DDM
25	Au 300	C-Flat 2/1	10 NEG	7	0	4.5	0	175	4	TBS + 0.02 % CHAPS

Figure 7.3: List of vitrification conditions tested on CODV-IL4.

CODV-IL4/IL13

IL4/13	**Grid type**		**Glow Discharge**		**Vitrobot**			**Sample**		
Try nº	**Grid**	**Support**	**Time (s) + Polarity**	**Voltage (mA)**	**Blot Force**	**Blot Time (s)**	**Wait Time (s)**	**Concentration (μg/ml)**	**Volume (μl)**	**Other**
1	Au 400	C-Flat 2/1	30 NEG	7	0	4.5	0	150	4	TBS pH 8 (default) + 0.06 mM DDM
2	Au 400	C-Flat 2/1	30 NEG	7	0	4	0	150	4	TBS + 0.06 mM DDM
3	Au 400	C-Flat 2/1	30 NEG	7	0	4.5	0	150	4	TBS pH 8 (default) + 0.03 mM DDM
4	Au 400	C-Flat 2/1	30 NEG	7	0	4	0	150	4	TBS + 0.03 mM DDM

Figure 7.5: List of vitrification conditions tested on CODV-IL4/IL13.

CODV-IL13-Tralokinumab (TC)

TC	Grid type		Glow Discharge		Vitrobot			Sample		
Try nº	Grid	Support	Time (s)TBS + Polarity	Voltage (mA)	Blot Force	Blot Time (s)	Wait Time (s)	Concentration (µg/ml)	Volume (µl)	Other
1	Au 300	C-Flat 2/1	10 NEG	7	0	6	0	300	4	TBS pH 8 (default) + 0.03 mM DDM
2	Au 300	C-Flat 2/1	10 NEG	7	0	6	0	250	4	TBS + 0.03 mM DDM
3	Au 300	C-Flat 2/1	10 NEG	7	0	6	0	300	4	TBS + 0.06 mM DDM
4	Au 300	UltrAuFoil 1.2/1.3	40 NEG	25	0	6	0	300	4	TBS + 0.06 mM DDM
5	Au 300	C-Flat 2/1	10 NEG	7	0	6	0	200	4	TBS + 0.03 mM DDM
6	Au 300	C-Flat 2/1	10 NEG	7	0	6	0	175	4	TBS + 0.03 mM DDM
7	Au 300	C-Flat 2/1	10 NEG	7	0	6	0	250	4	TBS + 0.03 mM DDM
8	Au 300	C-Flat 2/1	10 NEG	7	0	6	0	250	4	TBS + 0.03 mM DDM
9	Au 300	C-Flat 2/1	10 NEG	7	0	6	0	300	3	TBS + 0.06 mM DDM
10	Au 300	C-Flat 2/1	10 NEG	7	0	6	0	300	3	TBS + 0.06 mM DDM
11	Au 300	UltrAuFoil 1.2/1.3	10 NEG	25	0	6	0	300	2x 4	TBS + 0.06 mM DDM
12	Au 300	UltrAuFoil 1.2/1.3	10 NEG	25	0	6	0	300	2x 4	TBS + 0.06 mM DDM
13	Au 300	C-Flat 1.2/1.3	20 NEG	7	2	7	0	300	3	TBS + 0.03 mM DDM
14	Au 300	C-Flat 1.2/1.3	20 NEG	7	-10	7	0	300	3	TBS + 0.03 mM DDM
15	Au 300	C-Flat 1.2/1.3	20 NEG	7	-4	7	0	275	3	TBS + 0.03 mM DDM
16	Au 300	C-Flat 1.2/1.3	20 NEG	7	2	7	0	300	3	TBS + 0.01 mM LMNG
17	Au 300	C-Flat 1.2/1.3	20 NEG	7	2	7	0	300	3	TBS + 0.02 mM LMNG
18	Au 300	C-Flat 1.2/1.3	20 NEG	7	2	7	0	250	3	TBS + 0.01 mM LMNG
19	Au 300	C-Flat 1.2/1.3	20 NEG	7	2	7	0	250	3	TBS + 0.02 mM LMNG

Figure 7.6: List of vitrification conditions tested on TC.

7.4 Refinement statistics for the CODV-IL13-Tralokinumab (TC) cryo-EM dataset

EM data collection and reconstruction statistics

Microscope	Titan Krios G3
Voltage (kV)	300
Detector	K2 Summit
Magnification	165,000
Pixel size (Å/pix)	0.83
Frames per exposure	40
Exposure (e^-/Å^2)	46
Defocus range (µm)	-1.20 to -3.0
Micrographs collected	15198
Particles extracted/used	546717/218792
Map sharpening B-factor	-97.066
Unmasked resolution at 0.5/0.143 FSC (Å)	6.87/4.6
Masked resolution at 0.5/0.143 FSC (Å)	4.75/4.06

Model refinement and validation statistics

Composition	
Amino acids	1220
Atoms	9210
RMSD bonds (Å) (# > 4σ)	0.007 (2)
RMSD angles (°) (# > 4σ)	0.893 (1)
Mean B-factors	160.62
Ramachandram	
Outliers (%)	0.17
Allowed (%)	16.69
Favoured (%)	83.14
Rotamer outliers	0.10
Cβ outliers (%)	0.00
CaBLAM outliers (%)	6.33
MolProbity score	2.80
Clash score	42.31
CC (mask)	0.82

Table 7.1: Refinement statistics for the CODV-IL13-Tralokinumab (TC) cryo-EM dataset

Cryo-electron microscopy (cryo-EM) has experienced a surge in capability and popularity in recent years. In particular, advances in hardware and software have allowed the imaging of the structures at progressively higher resolutions (<4 Å). This has enabled the exploration of cryo-EM as a tool for elucidating antibody-antigen binding interactions in near-native conditions. This would be an invaluable step forward in drug discovery. In the field of antibody therapeutics, multispecific antibodies, which are engineered to bind to two or more targets, are currently of the highest interest. Unfortunately, there are currently no reports of high resolution cryo-EM studies of whole antibodies, or of antibody-antigen interfaces, within the full-antibody context. Thus, the main goals of this thesis were two-fold: 1) The establishment of a pipeline, from sample preparation to structure, for whole antibody cryo-EM studies, that will serve as a starting point for future projects in the field; 2) The use of cryo-EM to elucidate, at close to atomic level, details of multispecific antibody-antigen interfaces within the full-antibody context. This work targeted three antibodies: CODV (bispecific), TBTI (bispecific) and TDT (trispecific), with a strong focus on CODV and its complexes with the small antigen ligands IL4 and IL13. Initial work (**Chapter 1**) concentrated on the preparation, purification and biophysical characterization of individual antibodies and of CODV-antigen complexes. Here, SPR studies showed that CODV binds to both of its IL4 and IL13 antigens with picomolar affinity and that this affinity is independent of binding order or positional effects. Preliminary negative-stain electron microscopy (NS-EM) experiments (**Chapter 2**) provided information concerning sample quality and dispersion and allowed the production of low-resolution reconstructions for potential use in cryo-EM analysis. The NS-EM experiments suggested a high level of flexibility and conformational heterogeneity of the antibodies, especially at the Fc level. Intriguingly, the reconstructions obtained for CODV-antigen complexes did not show any density corresponding to the antigens. Due to the therapeutic advantages of the format and its priority within the antibody development efforts of Sanofi, the CODV system was then used for cryo-EM pipeline development (**Chapter 3**). Grid preparation strategies were first explored in order to ameliorate on-grid aggregation of CODV antibodies and their aversion for conventional supports. Cryo-EM datasets for *apo*-CODV, CODV-IL4 and CODV-IL4/IL13 were then collected at the Titan Krios 300 keV microscope at the ESRF CM01 beamline. Processing of these datasets confirmed both the apparent absence of antigens bound to CODV and the high conformational heterogeneity of the antibody observed in NS-EM experiments. The latter meant that only very low resolution, and sometimes incomplete, reconstructions of CODV and its antigen complexes could be obtained. A strategy to reduce the conformational flexibility was therefore proposed. This comprised labelling the IL13 antigen with Tralokinumab, an anti-IL13 antibody (**Chapter 3**). A ternary CODV-IL13-Tralokinumab complex was therefore prepared and purified. NS-EM experiments revealed density for IL13 and cryo-EM experiments based on the pipeline developed was therefore carried out. These resulted in a medium-resolution reconstruction (3.93 Å) of the CODV-IL13-Tralokinumab interface, suggesting that this labelling strategy can be used in other studies. This work therefore paves the way for future cryo-EM studies of antibody-antigen complexes, especially in those where the presence of Fc is key for the correct biological context, such as opsonization or cell degranulation.

La microscopie cryoélectronique (cryo-EM) a connu une montée en puissance et en popularité ces dernières années. En effet, les progrès du matériel et des logiciels ont permis la détermination de structures à des résolutions élevées (<4 Å). Cela a permis l'exploration de la cryo-EM comme outil pour élucider les interactions anticorps-antigène dans des conditions quasi-natives, une avancée importante pour la recherche pharmaceutique. Dans le domaine des anticorps thérapeutiques, les anticorps multispécifiques, qui sont conçus pour se lier à deux ou plusieurs cibles, sont actuellement du plus grand intérêt. Malheureusement, il n'y a actuellement aucune publication d'étude cryo-EM à haute résolution d'anticorps entiers, ou d'interfaces anticorps-antigène dans le contexte de l'anticorps complet. Ainsi, les principaux objectifs de cette thèse étaient doubles : 1) La mise en place d'un protocole, de la préparation des échantillons à la structure, pour les études cryo-EM d'anticorps entiers, qui servira de point de départ à de futurs projets dans ce domaine ; 2) L'utilisation de la cryo-EM pour élucider à haute résolution les détails des interfaces antigène-anticorps multispécifiques dans le contexte de l'anticorps complet. Ces travaux ont ciblé trois anticorps : CODV (bispécifique), TBTI (bispécifique) et TDT (trispécifique), avec un fort accent sur le CODV et ses complexes avec les petits antigénes IL4 et IL13. Les premiers travaux (chapitre 1) se sont concentrés sur la préparation, la purification et la caractérisation biophysique d'anticorps individuels et de complexes CODV-antigène. Ici, les études SPR ont montré que CODV se lie à ses deux antigènes IL4 et IL13 avec une affinité picomolaire et que cette affinité est indépendante de l'ordre de liaison ou des effets de position. Des expériences préliminaires de microscopie électronique à coloration négative (NS-EM) (chapitre 2) ont fourni des informations sur la qualité et la dispersion des échantillons et ont permis la détermination de reconstructions à basse résolution. Les expériences NS-EM ont suggéré un niveau élevé de flexibilité et d'hétérogénéité conformationnelle des anticorps, en particulier au niveau du Fc. De plus, les reconstructions obtenues pour les complexes CODV-antigène n'ont montré aucune densité correspondant aux antigènes. En raison des avantages thérapeutiques du format et de sa priorité pour Sanofi, le système CODV a ensuite été utilisé pour la mise en place d'un protocole de cryo-EM (chapitre 3). Des stratégies de préparation de grille ont d'abord été explorées afin de limiter l'agrégation des anticorps CODV et leur aversion pour les supports conventionnels. Des jeux de données Cryo-EM pour apo-CODV, CODV-IL4 et CODV-IL4 / IL13 ont ensuite été collectés au microscope Titan Krios 300 keV de la ligne de lumière ESRF CM01. Le traitement de ces données a confirmé à la fois l'absence apparente d'antigènes liés à CODV et la forte hétérogénéité conformationnelle de l'anticorps déjà observée dans les expériences NS-EM. Ceci signifie que seules des reconstructions à très faible résolution, parfois incomplètes, pouvaient être obtenues. Une stratégie de réduction de la flexibilité conformationnelle a donc été proposée. Cela comprenait le marquage de l'antigène IL13 avec du tralokinumab, un anticorps anti-IL13 (chapitre 3). Un complexe ternaire CODV-IL13-Tralokinumab a donc été préparé et purifié. Les expériences NS-EM ont révélé la présence de densité pour IL13 et des expériences de cryo-EM basées sur le protocole développé ont été réalisées. Celles-ci ont abouti à une reconstruction à résolution moyenne (3.93 Å) de l'interface CODV-IL13-Tralokinumab, suggérant que cette stratégie de marquage peut être utilisée dans d'autres études. Ce travail ouvre donc la voie à de futures études cryo-EM des complexes anticorps-antigène, en particulier pour celles où la présence de Fc est essentielle pour le bon contexte biologique, comme l'opsonisation ou la dégranulation cellulaire.